Exploring the utility of high frequency satellite information on wildfire characterization and impact estimation

A thesis submitted in fulfilment of the requirements for the degree of Doctor of Philosophy

Konstantinos Chatzopoulos Vouzoglanis

Integrated Masters Spatial Planning and Development – Aristotle University of Thessaloniki

M.Sc. Civil Engineering (track Geoscience and Remote Sensing) – Delft University of Technology

ORCID: 0000-0001-7502-4216

School of Science

College of Science, Technology, Engineering and Maths

RMIT University

Australia

November 2024

Declaration of Authorship

I certify that except where due acknowledgement has been made, this research is that of the author alone; the content of this research submission is the result of work which has been carried out since the official commencement date of the approved research program; any editorial work, paid or unpaid, carried out by a third party is acknowledged; and, ethics procedures and guidelines have been followed.

In addition, I certify that this submission contains no material previously submitted for award of any qualification at any other university or institution, unless approved for a joint-award with another institution, and acknowledge that no part of this work will, in the future, be used in a submission in my name, for any other qualification in any university or other tertiary institution without the prior approval of the University, and where applicable, any partner institution responsible for the joint-award of this degree.

I acknowledge that copyright of any published works contained within this thesis resides with the copyright holder(s) of those works.

I give permission for the digital version of my research submission to be made available on the web, via the University's digital research repository, unless permission has been granted by the University to restrict access for a period of time.

Konstantinos Chatzopoulos Vouzoglanis, 28/11/2024

Acknowledgements

I acknowledge the Traditional Owners of the land on which I completed my studies and this dissertation and their continuing connection to it, the Wurundjeri Woi-wurrung people of the Kulin Nation. I pay my respects to their Elders, past and present. I further recognise the profound and ongoing effects of imperialism and colonialism on the Aboriginal and Torres Strait Islander peoples of Australia. I am committed to honouring the resilience and knowledge of the First Peoples of Australia and advocating for a future rooted in respect, equity, and justice.

I acknowledge the support I have received for my research through the RMIT Research Stipend Scholarship and the SmartSat Cooperative Research Centre top-up scholarship (Project 3.04s). I am also incredibly grateful to all the people that have supported me throughout this journey, within RMIT University, as well as my family and community.

I am deeply grateful for my supervisors, Prof. Simon Jones, Dr Mariela Soto-Berelov and Assoc. Prof. Karin Reinke. Thank you for offering me the opportunity to study with you and for going above and beyond to support me throughout my candidature. I appreciate the time you invested in me, offering advice, attending meetings, debating ideas and reviewing my work. I enjoyed exploring all the rabbit holes we collectively brought to the table, helping me grow as a curious mind and understand what kind of researcher I would like to be.

To my friends and fellow PhD students at RMIT, thank you for being there to bounce ideas, provide motivation and share struggles. Sven, thank you for that first coffee when I was new in Australia and for checking in with me and urging me to apply for a PhD position when I was about to give up. Jenna, Bryan, and James, thank you for welcoming me to the remote sensing group during the lockdowns, and organising all the activities, whether a shut-up and write session or a squash game. Johann, Mohammad, Shaye, Nur, Michael, Ashley, Nick, Tuv, Alvaro, Percy, Glen, and Athenee, thank you for the company, lunches, coffees, dinners, trips, picnics, birthday cards and cakes. I am grateful for this community and all our time together, which made my candidature very enjoyable.

To my parents Elli and Stavros, I am deeply grateful for all your sacrifices. Mum, thank you for pushing me to achieve my goals in life and teaching me to be methodical, patient, and equitable. Dad, thank you for showing me how to be calm and practical in any situation and face problems logically. To my wife, Lucille, thank you for all your support and for not shying away from discussing all my research ideas with you. You can give a good presentation about my PhD in my place if needed. To my parents-in-law, Simon and Margaret, and my siblings-in-law, Peggy, Patrick and Deborah, thank you for being my community and support network outside academia. Finally, thank you to my family and friends in Greece, the Netherlands, and the UK, who stayed connected with me while I was so far away from them and provided me with good memories during vacations and weddings in the last four years.

Contents

List of Figures

List of Tables

Abbreviations

ABI	Advanced Baseline Imager
ACT	Australian Capital Territory – ACT
AHI	Advanced Himawari Imager
AMI	Advanced Meteorological Imager
BRIGHT	Biogeographical Region and Individual Geostationary HHMMSS Threshold
CBI	Composite Burn Index
CT	Climate Teleconnection
DCCEEW	Department of Climate Change, Energy, the Environment and Water
DEECA	Department of Energy, Environment and Climate Action
dNBR	Differenced Normalised Burn Ratio
DR	dimensionality reduction
EMR	electromagnetic radiation
ENSO	El Niño Southern Oscillation
ESA	European Space Agency
FFC	Fire Fractional Cover
FGR	fire growth rate
FRE	Fire Radiative Energy
FRP	Fire Radiative Power
FTA	Fire Thermal Anomaly
GEO	GEOstationary
GeoCBI	Geometrically corrected Composite Burn Index
GeoXO	Geostationary Extended Observations
GHG	Greenhouse Gases
HDF	Hierarchical Data Format
IBRA	Interim Biogeographic Regionalisation for Australia
IFOV	Instantaneous Field of View
IOD	Indian Ocean Dipole
JMA	Japanese Meteorological Agency
LAADS	NASA's Level 1 and Atmosphere Archive and Distribution System
LAI	Leaf Area Index
LC	Land Cover
LEO	Low Earth Orbiting
LULC	Land Use Land Cover
LWIR	longwave
MIR	middle infrared
MJ	Mega Joules
MODIS	Moderate Resolution Imaging Spectroradiometer
MSG	Meteosat's Second Generation
MSI	Multispectral Imager

MW	Mega Watts
NASA	National Aeronautics and Space Administration
NBR	Normalised Burn Ratio
NICT	National Institute of Information and Communications Technology
NIR	Near-Infrared
NSW	New South Wales – NSW
OLS	Ordinary Least Squares
PaCMAP	Pairwise Controlled Manifold Approximation
PC	Principal Component
PCA	Principal Component Analysis
QLD	Queensland
R	Correlation coefficient
RBR	Relativised Burn Ratio
RdNBR	Relative dNBR
SEVIRI	Spinning Enhanced Visible and Infrared Imager
SLSTR	Sea and Land Surface Temperature Radiometer
SNPP	Suomi National Polar-orbiting Partnership
SWIR	Shortwave Infrared
t-SNE	t-distributed Stochastic Neighbour Embedding
UMAP	Uniform Manifold Approximation and Projection for Dimension Reduction
VIC	Victoria
VIIRS	Visible Infrared Imaging Radiometer Suite

Abstract

Wildfires are environmental phenomena that contribute to global carbon emissions and can cause abrupt ecological changes in local environments. Within the context of a changing climate, wildfire frequency and impact are projected to worsen. The effective monitoring, characterisation and impact assessment of wildfires can be quite challenging due to their potentially large extent, which can include a variety of land cover types, fuel loads, moisture conditions and topography. Additional challenges arise also from rapid changes in intensity and direction caused by factors such as the wind velocity and humidity. To this end, collecting data that describes the different stages and aspects of wildfires is crucial for understanding and mitigating their effects.

Satellite remote sensing systems provide opportunities to monitor wildfires at a variety of spatiotemporal resolutions. Traditionally, Low Earth Orbiting (LEO) satellite sensors have been the main source of wildfire data, from hotspot detections to severity estimations. Due to their orbital limitations, however, LEO sensors have a temporal resolution (typically 12-24 hours) that is not adequate for capturing the rapidly changing course of an active fire. Meanwhile, GEOstationary (GEO) sensors are capable of capturing data multiple times in an hour but have coarser spatial resolution that reduces the ability to detect small and cool actively burning fires. Contemporary GEO sensors, such as the Advanced Baseline Imager (ABI) and the Advanced Himawari Imager (AHI), capture full-disk images of the earth every 10-minutes in a range of visible, near-infrared and thermal spectral channels, opening new pathways for high-frequency wildfire monitoring. This dissertation explores the utility of these satellite sensors for wildfire characterisation and investigates opportunities for new ways of fire impact classification, using AHI which unlike ABI has acquisition coverage over Australia. To address this aim, four research questions are posed.

The first research question examined the equivalency of Fire Radiative Power (FRP) estimates – expressed in SI units of megawatts (MW) – from LEO and GEO sensors, during the Black Summer Fires in Southeastern Australia (2019-2020). Specifically, the commonly used data products from the MODIS LEO sensor (MOD14/MYD14) and the AHI sensor (BRIGHT/AHI) were compared. The intercomparison was implemented across different geographical areas and scales, including regional segmentations, spatially and temporally continuous wildfire events and individual concurrent hotspots/pixels. Results show a high agreement between the products at the pixel level ($r = 0.74$), but with BRIGHT/AHI consistently underestimating FRP (by ~15%) due to its lower spatial resolution. However, BRIGHT/AHI's temporal profile of fire activity was significantly more detailed at a regional level with up to 144 cloud free observation opportunities every 24 hours compared to MODIS, which has four observation opportunities

per day. Therefore, the confidence in BRIGHT/AHI's ability to capture equivalent wildfire detail to MODIS and reveal new insights, for an extreme event such as the Black Summer fires (2019-2020), was established.

The second research question progressed the intercomparison of the BRIGHT/AHI FRP estimations to the whole continent of Australia for an entire year, day and night, inclusive of a diverse range of land covers, burning conditions and durations. In addition to MODIS, LEO active fire detections from VIIRS (VNP14IMG) were included to further explore the effect of higher spatial resolution data in the intercomparison. The results suggest that LEO and GEO products captured similar wildfire dynamics, with a high agreement on a pixel level for concurrent detections ($r = 0.74$-0.77). The FRP estimations from BRIGHT/AHI, MODIS and VIIRS showed similar distributions across different land covers and regions, although with a clear positive bias for higher spatial resolution data upwards of 10 times the BRIGHT/AHI FRP estimations on average. Unsurprisingly, the regional diurnal fire intensity profiles captured by the LEO sensors demonstrated major temporal gaps between acquisitions compared to BRIGHT/AHI, especially around the times of peak and low fire activity. Examining individual localised events revealed that AHI captured a continuous stream of data that closely followed, although underestimated, all the temporal FRP peaks captured by either MODIS or VIIRS, with MODIS missing fire activity on some occasions. These findings indicate the ability of GEO data to capture active fire information accurately over large spatial scales, with an improved temporal detail over the LEO sensors.

With the capability of the BRIGHT/AHI product established, the third research question explored the association of this new stream of wildfire activity data to commonly used burn severity metrics. While burn severity has been extensively studied using bi-temporal spectral differencing indices, such as the Differenced Normalised Burn Ratio (dNBR), few studies have examined whether active fire observations capture the same aspects of fire activity as dNBR. Here, the BRIGHT/AHI FRP metrics were compared to Sentinel-2 dNBR metrics across Australia. Results reveal that the two groups of metrics were only weakly correlated for high maximum FPR fires ($r = 0.33$-0.39), while regional, land cover, and duration variations did not have a significant impact on the correlations. Higher correlations were only achieved after introducing different burned area classification thresholds to derive the fire fractional cover, or FFC, (percentage of an AHI pixel classified as burned by Sentinel-2 data) for each category of fire hotspots based on their fire intensity (FRP) and duration.

As the spectral differencing (Sentinel-2 dNBR) and FRP (BRIGHT/AHI) metrics capture independent aspects of wildfire activity, the fourth research question explored the combination of the two in a new wildfire impact classification method. Active fire metrics, such as the maximum FRP, the total energy emitted (Fire Radiative Energy – FRE) and the duration of the fire in a specific pixel location, were combined with the dNBR, the FFC and the pre-fire NBR (as a proxy of pre-fire vegetation health) in a

dataset. Commonly used and state of the art dimensionality reduction techniques (e.g., PCA, t-SNE, UMAP, PaCMAP) were used to transform the dataset into two-dimensional projections that distributed wildfire pixels in terms of linear or non-linear associations across the six wildfire variables (Maximum FRP, FRE, Duration, dNBR, FFC, pre-fire NBR). Then, agglomerative hierarchical clustering was implemented to group the transformed data into clusters that were aggregated using ensemble clustering. The resulting ensemble clusters represented similar fires across a variety of land covers and were attributed different Composite Wildfire Impact (CWI) ratings based on their individual variable medians. The results reveal that expected fire regime patterns are effectively captured on a continental scale and over a variety of biogeographical settings. Furthermore, despite the spatial resolution differences, local burn severity assessments based on dNBR and *in-situ* data demonstrated a broad agreement with the proposed CWI rating. The proposed data-driven methodology can be adapted and applied to different environments globally, without the need for training data, and assist in the monitoring of fire regime patterns and trends over extensive spatiotemporal scales.

This thesis highlights the potential of contemporary geostationary satellite sensors in advancing wildfire monitoring and impact assessment. By providing continuous, high-frequency observations, GEO sensors can complement and, in some regards, surpass traditional LEO sensors in capturing the dynamic nature of wildfires. The combination of GEO fire intensity metrics with established LEO burn severity indices offers a new pathway to understanding and categorising wildfire impacts across landscapes. The methodology developed here enhances our ability to monitor wildfires on a continental scale, while it also provides a scalable and globally applicable framework for future research and operational monitoring. As climate change continues to increase the frequency and intensity of wildfires, the insights and tools provided here can inform mitigation strategies and improve our resilience to the environmental challenges of the future.

Chapter 1. Introduction

This thesis explores the utility of next-generation geostationary sensors in combination with polar-orbiting satellite data for wildfire characterisation. It proposes a set of remotely sensed variables and auxiliary data that can provide important information regarding wildfire effects that goes beyond the traditional and commonly used burn severity spectral indices. These effects are described as the impact of the wildfire and are estimated by combining active fire and spectral differencing metrics. This chapter introduces the key concepts associated with the remote sensing of wildfire, identifies knowledge gaps in the literature and formulates the research aim and questions that are the focus of this dissertation.

1.1. Motivation

Every year, the world witnesses extreme weather events, such as forest fires, floods and hurricanes (Messerli et al., 2019). The United Nations' 2030 agenda, with Sustainable Development Goals 13 and 15, urges for national policy adaptation to hazards related to climate change, as well as the protection and restoration of terrestrial ecosystems (UN General Assembly, 2015). Forests are important ecosystems and carbon storage sinks, which release considerable amounts of greenhouse gases (GHG) when burned. As fire seasons become longer and more extreme, with higher temperatures and less precipitation, wildfire regimes are changing often with negative impacts (Jia et al., 2019). If not disturbed again, burnt forest and vegetated areas are expected to recover within years to decades, recapturing most of the released carbon (Landry and Matthews, 2016). Therefore, wildfire monitoring and an enhanced understanding of their ignition conditions, behaviour and impact are crucial (Lang and Moeini-Meybodi, 2021).

Remote sensing offers a plethora of diverse observations that can be used to quantify fire danger based on pre-fire conditions (Pettinari and Chuvieco, 2020), detect wildfires actively burning at the time of satellite observation (Engel et al., 2021a), assess their GHG emissions based on their intensity and available carbon (biomass) (Nguyen et al., 2023), map burned areas (Roy et al., 2024), quantify the immediate impact on the landscape (Lizundia-Loiola et al., 2022), as well as monitor fuel load (Fernández-Guisuraga et al., 2022), fuel moisture (Rao et al., 2020), and the long-term recovery of the vegetation (Sparks et al., 2023a; Wooster et al., 2021). This information is often available over large spatial areas and for long periods of time, in some cases decades, with varying observation revisits ranging from days to minutes.

However, current satellite products are limited in their spatial and temporal resolution. Low Earth polar-orbiting sensors (LEO) used in wildfire detection and characterisation revisit the same location typically every 12-24 hours, which is not ideal for capturing dynamic and rapidly changing wildfires. Meanwhile, geostationary sensors (GEO) observe the full disk from a "fixed" position, capturing multiple images per hour, although their spatial resolution cannot compete with LEO sensors yet. To allow for more detailed and accurate description of fire regimes and effects, new frameworks are needed to combine the available data and maximise their strengths. Hence, an opportunity emerges to investigate and define better ways of using satellite-derived information for understanding wildfire impact in the landscape.

1.2. Wildfire monitoring from space

1.2.1. Active fire detection and intensity

Earth observations can be used to identify wildfire hotspots across large spatial areas in a timely manner. Active fires emit electromagnetic radiation (EMR) that can be detected by multispectral sensors in the middle (MIR) and longwave (LWIR) infrared part of the spectrum, between 3-5μm and 8-14μm respectively (Dozier, 1980; Wooster et al., 2021). Often, additional spectral bands may also be used to filter out the contamination from signals other than fire (e.g., clouds, sun glint) (Giglio et al., 2021; Szpakowski and Jensen, 2019; Wooster et al., 2021).

Wildfires are rapidly changing phenomena, hence their prompt detection and spread monitoring is time sensitive. An important aspect of a satellite sensor used in fire detection is its revisit time to a specific location, also known as its temporal resolution. Polar-orbiting or LEO sensors are the most commonly used for fire detection, and their temporal resolution is typically 12 hours with one daytime and one nighttime observation (e.g., MODIS, VIIRS). Recently, fire detection algorithms have been adapted to GEO sensor observations to take advantage of their higher temporal resolution (10-30 minutes) (Engel et al., 2021b; Roberts and Wooster, 2008; Xu et al., 2021, 2010) enabling near continuous or persistent surveillance during cloud-free conditions. Therefore, GEO satellites offer the potential for more appropriate observation frequency that is better suited to dynamic phenomena such as active wildfires.

The sensor's ability to distinguish a fire from its background depends on several factors. For example, the size and temperature of the fire, the surrounding land cover, and the spatial resolution of the sensor. If a fire occupies only a fraction of an image's pixel, which corresponds to the sensor's minimum sampling distance on the ground, then a true detection can be missed (or omitted). LEO sensors usually have a higher spatial resolution than GEO sensors and are more successful at detecting small and low intensity fires (Engel et al., 2021b; Hall et al., 2019). Logically, the agreement between LEO and GEO increases with increasing fire temperature and size (Engel et al., 2021b; Xu et al., 2017).

The upwelling radiation in the MIR part of the EMR spectrum of an active fire is an indicator of fire intensity (Keeley, 2009; Wooster, 2002). The Fire Radiative Power (FRP) of an active fire detection, an instantaneous fire intensity proxy, can be estimated from satellite sensor MIR data (Wooster et al., 2005).

The time integration of FRP through the course of a wildfire's life is called Fire Radiative Energy (FRE), typically expressed in megajoules (MJ). FRE represents the total radiative energy released during combustion and is computed by integrating FRP over time. In practice, this is done by summing the product of FRP and the temporal interval between consecutive satellite observations. The temporal extent is determined by identifying the start and end of detectable fire activity from active fire detections. FRE has been shown to correlate with biomass consumption and it has been used to estimate GHG emissions (Ichoku and Kaufman, 2005; Mota and Wooster, 2018). This information is important for atmospheric carbon emission and climate change studies (Li et al., 2019a; Nguyen et al., 2023).

1.2.2. Burned area detection and wildfire severity

The change in the earth's surface reflectance caused by a wildfire, and especially in the Shortwave Infrared (SWIR) and Near-Infrared (NIR) part of the electromagnetic spectrum, is used to detect burned area and proxy measures of severity (Chuvieco et al., 2019; Key and Benson, 2006), and has been of interest in the remote sensing community for decades Such changes are used to quantify burned area assessments through a binary classification of land to burned or unburned. Meanwhile, the magnitude of spectral change is used to quantify the burn severity of a fire, a term that have been used in the literature to describe various aspects of wildfire effects on the landscape (Keeley, 2009; Key and Benson, 2006). The Normalised Burn Ratio (NBR) and its pre-post fire difference (dNBR) is a spectral index often used for burned area mapping and severity assessments that incorporates NIR and SWIR remotely sensed information (Key and Benson, 2006; López-García and Caselles, 1991). NBR-based indices are usually calibrated with *in-situ* assessments of severity in small plots of burned land and generalized locally (De Santis and Chuvieco, 2009; Gerrevink and Veraverbeke, 2021; Key and Benson, 2006). However, their generalization capabilities are limited over larger areas (Fernández-Guisuraga et al., 2023a; French et al., 2008), with their design often being deemed adequate for burned area mapping, but not for severity assessment (Roy et al., 2006). Meanwhile, canopy density (Yin et al., 2020) and poor pre-fire vegetation health (e.g., after a drought) (Gale and Cary, 2022) can also result in negligible spectral change estimates due to a fire.

Severity is usually defined as the spectral change of vegetation that has been burned, however, wildfire impact can be broader. Several small area studies have shown that the radiated heat of a fire can affect tree growth and mortality in the short and long term (Smith et al., 2016; Sparks et al., 2023a, 2017; Subasinghe Achchige et al., 2022). Furthermore, tall and dense canopies can obstruct the ground and fires that burn with low intensity may not reach the crown of the trees, making changes from a nadir perspective difficult to observe (Fernández-Guisuraga et al., 2023a). While next generation GEO sensors are limited in their ability to detect significant post-fire changes in reflectance due to coarse spatial resolution and strong diurnal reflectance variation (Roy et al., 2021), they provide near-continuous observations of active fire activity and radiative power. This capability offers a complementary data stream that, when integrated with high-resolution spectral differencing methods, can offer additional insights into wildfire impact, beyond what traditional post-fire assessments capture.

1.3. Satellite sensor data and algorithms for wildfire applications

1.3.1. Himawari-8/9 AHI

Himawari-8/9 are meteorological satellites launched by the Japanese Meteorological Agency (JMA) that follow a geostationary orbit. They carry the Advanced Himawari Imager (AHI) sensor, an instrument that is significantly improved from older generations and identical to the Advanced Baseline Imager (ABI) of the GOES satellites of NASA (Bessho et al., 2016). AHI provides full-disk scenes of the earth every 10-minutes in 16 multispectral bands that range between 500m and 2km spatial resolution. While AHI's observations are mainly used for meteorological purposes, its improved spatial resolution, and its ability to capture data in the MIR and Thermal Infra-red (TIR) make it a good candidate for wildfire monitoring. Specifically, bands 7 and 13 centred at 3.9μm and 10.4μm respectively, and at 2km spatial resolution (Table 1.1), have been used in various studies for active fire detection (Engel et al., 2021b, 2021a; Wickramasinghe et al., 2020) and FRP estimation (Engel et al., 2022; Xu et al., 2017).

Table 1.1 Himawari-8/9 AHI sensor specifications, showing central wavelengths and spatial resolution per band (Bessho et al., 2016).

Part of the EM spectrum	Band	Wavelength (μm)	Spatial resolution (km)
Visible	1	0.47	1
	2	0.51	1
	3	0.64	0.5
Near-Infrared	4	0.86	1
	5	1.6	2
	6	2.3	2
Infra-red	7	3.9	2
	8	6.2	2
	9	6.9	2
	10	7.3	2
	11	8.6	2
	12	9.6	2
	13	10.4	2
	14	11.2	2
	15	12.4	2
	16	13.3	2

1.3.2. Geostationary active fire detection algorithms

Fire detection algorithms are used with satellite data to identify fires by identifying spatial or temporal anomalies between fire pixels and their surroundings. These algorithms typically utilise Brightness Temperature (BT) bands in the MIR and TIR parts of the spectrum, around 3.9μm and 10.4μm respectively, as well as reflectance in the red band (0.64μm) for cloud masking and albedo thresholds (Dozier, 1980; Engel et al., 2021b; Wooster et al., 2021). The most prominent spatial anomaly algorithm is the Fire Thermal Anomaly (FTA) (Roberts and Wooster, 2008). FTA is a contextual algorithm, which means that it identifies potential fire pixels in single images using fixed thresholds and then refines its detection by comparing them to nearby non-fire pixels (Wooster et al., 2021). FTA has been implemented across different geostationary sensors, such as the Meteosat SEVIRI over Europe and Africa (Freeborn et al., 2014a; Wooster et al., 2015), the two GOES sensors over the Americas (Xu et al., 2010), and AHI over East Asia and Australia (Xu et al., 2017).

Meanwhile, algorithms that detect fire hotspots based on spatial and temporal information utilising GEO sensors (AHI) have also been developed (Engel et al., 2021b, 2021a; Hally et al., 2023, 2019). One such algorithm is the Biogeographical Region and Individual Geostationary HHMMSS Threshold (BRIGHT) that has been developed for AHI with a focus on Australia (Engel et al., 2021b, 2021a). BRIGHT/AHI considers the temporal information of each pixel as well as the neighbouring pixels that are situated in the same biogeographical region. The temporal information includes all the available cloud-free observations in the 28 days leading up to a new observation, and it is used to derive the expected fire-free background BT for each of the 419 unique biogeographical regions of Australia (DAWE, 2000; Engel et al., 2021a). Each new observation is then compared to the expected background BT and it is classified as an active fire detection or not, based on a series of statistical thresholds (Engel et al., 2021b, 2021a). For each hotspot, BRIGHT/AHI also provides fire intensity information (FRP) using the model proposed by Wooster et al. (2005, 2003) (Engel et al., 2022).

1.3.3. AQUA/TERRA MODIS

NASA's Aqua and Terra LEO satellites and the Moderate Resolution Imaging Spectroradiometer (MODIS) sensors have been providing daily global earth observations for over than two decades. The MODIS observation capabilities include 36 spectral bands from 0.41μm to 14.23μm, at spatial resolutions ranging from 250m to 1km. The active fire detections are derived using a contextual algorithm that utilizes the MODIS brightness temperature bands 21, 22, and 31 (Table 1.2) (Giglio et al., 2021, 2016). The hotspots are available at 1km of spatial resolution, two times a day from each of two satellites and they include FRP estimations using the method proposed by Wooster et al. (2003). The resulting datasets are distributed as MOD14 (Terra) and MYD14 (Aqua) products (Giglio et al., 2021).

Table 1.2 MODIS specifications, showing central wavelengths and spatial resolution per spectral band that is relevant for the fire detection algorithm (Giglio et al., 2016).

Band	Wavelength (μm)	Spatial resolution (km)
21	4	1
22	4	1
31	11	1

1.3.4. SNPP VIIRS

The Suomi National Polar-orbiting Partnership Visible Infrared Imaging Radiometer Suite (SNPP/VIIRS) is a sensor used for various earth observation applications, including active fire monitoring, since 2012 (Schroeder and Giglio, 2018). The VIIRS sensor offers data in 21 spectral bands, ranging from 0.412 μm to 12μm. VIIRS bands I4 and I5 (Table 1.3) are used for active fire hotspot detection and FRP estimation, and their derivation follows the same methodology as MODIS (Giglio et al., 2016). The active fire VIIRS data are available at a higher spatial resolution compared to MODIS (375m) and are distributed as VNP14IMG (Schroeder and Giglio, 2018). VIIRS data have a global coverage, with two observation per day (day and night) (Schroeder et al., 2014).

Table 1.3 VIIRS specifications, showing central wavelengths and spatial resolution per spectral band that is relevant for the fire detection algorithm (Schroeder et al., 2014).

Band	Wavelength (μm)	Spatial resolution (m)
I4	3.74	375
I5	11.45	375

1.3.5. Sentinel-2 MSI

The Sentinel-2 mission is a two-satellite constellation on a polar-orbit that carry the Multispectral Imager (MSI). The satellites' temporal resolution is 10 days, that when combined can offer data for specific locations every 5 days. MSI data are available in three different spatial resolutions depending on the spectral band, at 10m, 20m and 60m (ESA, 2015). While these data are not ideal for active fire monitoring due to the long revisit times and the absence of MIR and TIR spectral bands Table 1.4), they are suitable for monitoring temporal changes in reflectance of the burned areas at a much higher spatial resolution than the active fire hotspot sensors. The Near Infrared (band 8A) and Short-wave Infrared (band 12) bands are often used to derive NBR and dNBR indices using MSI data (Roy et al., 2021).

Table 1.4 Sentinel-2 MSI specifications, showing central wavelengths and spatial resolution per band (ESA, 2015).

Band	Wavelength (nm)	Spatial resolution (m)
1	443	60
2	490	10
3	560	10
4	665	10
5	705	20
6	740	20
7	783	20
8	842	10
8A	865	20
9	945	60
10	1375	60
11	1610	20
12	2190	20

1.4. Problem statement

Next generation geostationary sensors make active fire behaviour data available at a higher spatial and temporal resolution that has been unavailable from sensors in such orbits until recently. Previously, the lack of high frequency information on the active fire progression (Keeley, 2009) meant that wildfire impact from space has mostly been studied using surface reflectance change due to fire (e.g., dNBR). New active fire information from GEO sensors is becoming increasingly available in higher temporal and spatial resolutions, but so far it has not been explored whether it can also be used to characterise wildfire impact. Here, we define wildfire impact as the composite effects on vegetation, ecosystems and the landscape that are observed through remotely sensed spectral changes and the release of energy from burning biomass.

Few studies have explored the association between active fire intensity and burn severity metrics by directly comparing FRP from polar-orbiting sensors (MODIS) to the change in spectral indices for small area fires, but no significant correlation was found (Henry et al., 2019; Heward et al., 2013). GEO datasets, such as BRIGHT/AHI, can provide detailed diurnal information about the active fire and reduce the temporal uncertainty introduced by polar-orbiting observations. However, despite its ability to rapidly detect fires (Engel et al., 2021a, 2021b), BRIGHT/AHI is a nascent product and its fire intensity monitoring capabilities have not been fully explored.

1.5. Research aim

This thesis argues that the existing spectral differencing methods commonly utilised to characterise fires can be augmented by including high frequency active fire behaviour information. The aim is to explore the utility of these new earth observations and derived products, expand on their evaluation methods, and investigate new approaches for understanding and characterising wildfire activity and impact. This is achieved over a comprehensive variety of climates, landscapes, and fire regimes, by including the whole continent of Australia for a year of fire activity (April 2019-Mach 2020).

1.5.1. Research questions

The research aim is achieved by investigating four research questions outlined below:

Research Question 1: How do measures of fire radiative power from geostationary satellites compare with those from polar-orbiting satellites for an extreme wildfire event?

In this research question, next generation geostationary wildfire detections and their associated intensity estimations (BRIGHT/AHI) are compared to equivalent and commonly used polar-orbiting sensor data from MODIS (MOD14/MYD14). The goal is to assess the ability of BRIGHT/AHI to capture the intensity of fire and to explore opportunities stemming from its higher temporal resolution to characterise wildfires. The data used correspond to the southeastern Australia during the devastating Black Summer Fires (2019/2020), which was an unprecedented fire season that exceeded typical scale and intensity expectations. The Black Summer fires started in northern Australia and progressed south, affecting large parts of Northern Territory, Queensland, New South Wales, and Victoria. The association between the datasets is assessed for simultaneous observations on a pixel, single fire event, and biogeographical region level. The diurnal fire intensity profiles and spread patterns over the study area and period are also compared.

Research Question 2: How do measures of fire radiative power from geostationary satellites compare with those from polar-orbiting satellites when examining an entire year of wildfire activity, for the whole of Australia to capture seasonal and geographical variations?

This research question expands RQ1's study area (southeastern Australia) and period (over an extreme wildfire event), to all of Australia between April 2019 and March 2020, to further explore the equivalency of BRIGHT/AHI to other established polar-orbiting datasets over varying land covers, fire regimes and seasons. An additional polar-orbiting dataset from VIIRS (VNP14IMG) with a higher spatial resolution than MODIS is included in the analysis. Simultaneous observations between the sensors are compared to evaluate the effect of their different spatial resolutions on fire intensity estimation. The temporal resolution differences between the datasets are also assessed by comparing their total observation records for high and low fire activity months, exploring the benefits of high frequency observations. Finally, the time-series of FRP for four fire events are compared to examine additional temporal resolution discrepancies in more detail.

<u>Research Question 3</u>: What is the relationship between different earth observation measures of fire intensity (i.e., active fire) and burn severity (i.e., impact of fire)?

The third research question explores the association between fire intensity data (Maximum FRP and FRE) from BRIGHT/AHI and burn severity data from Sentinel-2. These metrics were selected based on their relevance to different phases of a wildfire event. Maximum FRP provides a measure of peak fire intensity, offering insight into the most extreme radiative output of the event. FRE reflects the total energy released from the burning process and serves as a proxy for total fuel consumption. Finally, dNBR is used as a proxy of burn severity, as it is traditionally used in burn severity assessments in remote sensing. The aim is to examine whether these distinct metrics correlate and capture similar effects for the same fires. Their equivalency is studied over different land covers, burning conditions and durations all over Australia between April 2019 and March 2020 to reveal opportunities for complementary use.

<u>Research Question 4</u>: How can cross-platform fire intensity and severity measures be used to derive new metrics of wildfire characterization and impact in the landscape?

The final research question builds on the outcomes of the previous research and proposes a framework to characterise wildfire impact on vegetation. The framework also introduces additional dimensions to fire impact assessment, by incorporating pre-fire spectral observations, land cover, burned area percentage of the AHI pixel and fire duration variables. The study area is Australia, and the study period spans from April 2019 to March 2020. Current practices rely on spectral differencing and have certain drawbacks, such as an inability to generalise the severity assessments, and inconsistencies due to pre-fire vegetation condition and fire history. The aim of this research question is to augment the existing methodologies with newly available active fire information from geostationary sensors.

1.6.Thesis structure

This thesis is organized into six chapters, including this introductory chapter (Chapter 1). The following four chapters (Chapter 2 to Chapter 5) correspond to each of the four research questions (1.5.1). Chapters 2 determine the capability of BRIGHT/AHI to estimate fire intensity during and extreme event. Chapter 3 expands on the methodology and study area of Chapter 2 including a complete fire season and all of Australia. Chapter 4 assesses the association between BRIGHT/AHI, whose confidence and limitations have been established in the previous chapters, with traditionally used burn severity metrics based on spectral differencing. Chapter 5 explores the combination of the two cohorts of metrics from Chapter 4 into a new wildfire impact rating system. By the time of this thesis's submission, Chapters 2 to 4 (Research Questions 1, 2 and 3) have been published in peer-reviewed journals (Chatzopoulos-Vouzoglanis et al., 2024, 2023, 2022), while Chapter 5 is submitted for publication. The outcome of this study, its contributions to the field and suggestions for future research are presented in Chapter 6.

Chapter 2. Comparing Geostationary and Polar-orbiting satellite sensor estimates of Fire Radiative Power (FRP) during the Black Summer Fires (2019-2020) in South-Eastern Australia

This chapter is based on: Chatzopoulos-Vouzoglanis, K., Reinke, K.J., Soto-Berelov, M., Engel, C., Jones, S.D., 2022. Comparing geostationary and polar-orbiting satellite sensor estimates of Fire Radiative Power (FRP) during the Black Summer Fires (2019–2020) in south-eastern Australia. International Journal of Wildland Fire 31, 572–585. https://doi.org/10.1071/WF21144

Abstract

We compared estimates of Fire Radiative Power (FRP) from sensors onboard geostationary Himawari-8 (BRIGHT_AHI) and polar-orbiting TERRA/AQUA (MOD14/MYD14) satellites during the 2019/2020 Black Summer Fires in South-Eastern Australia. Analysis was performed on a pixel, bioregion, and wildfire event basis to assess the utility of the new BRIGHT_AHI FRP product. Results show a high agreement between the products ($r = 0.74$, $p < 0.01$) on a pixel level, with BRIGHT_AHI generally underestimating FRP compared to MOD14/MYD14. Regional spatio-temporal trends were captured in more detail by BRIGHT_AHI due to its higher temporal resolution, with MOD14/MYD14 systematically underestimating the total and sub-diurnal FRP values. Nevertheless, both datasets captured similar fire ignition and spread patterns for the study region. On the event level, the correlation between the datasets was moderate ($r = 0.49$, $r = 0.67$), when considering different temporal constraints for hotspot matching. The results of this study indicate that BRIGHT_AHI approximates the well-established MOD14/MYD14 product during concurrent observations, while revealing additional temporal information for FRP trends. This gives confidence of the reliability of BRIGHT_AHI FRP estimates, opening the way for a denser observation record (10-minute intervals) that will provide new opportunities for fire activity reporting, some of which are presented here.

2.1. Introduction

During the 2019-2020 southern hemisphere summer, south eastern Australia experienced prolonged drought, dry fuel accumulation, and extremely high temperatures creating fire-favouring conditions (Fryirs et al., 2021). Multiple fires ignited across south-eastern Australia, eventually leading to major fires that were collectively termed the Black Summer Fires, burning almost 12.6 million ha of land, including 8 million ha of natural vegetation (Godfree et al., 2021; Wintle et al., 2020). Despite the long history of extreme wildfires in Australia, the Black Summer Fires were devastating for the already stressed ecosystems and unparalleled in terms of intensity, spatial and temporal scales (Wintle et al., 2020). It is estimated that 76 plant families were affected by the fires, while 498 out of the 816 vascular plant species lost more than 75% of the area they occupy (Godfree et al., 2021). In addition, 33 human lives were lost, thousands of houses burned down, while over one billion animals estimated to have been killed (Filkov et al., 2020).

Satellite earth observations allow wildfires to be observed and studied through their various stages; from ignition to impact in the landscape. The orbital characteristics of satellite sensors influence how often, and with what level of detail, fire activity can be observed and recorded. Most commonly used datasets are captured by polar-orbiting satellites in a Low Earth Orbit (LEO), which allows them to revisit almost any spot on the earth's surface from two times a day (e.g., TERRA/MODIS) to a few times a month (e.g., Sentinel-2 MSI). Recently, data from satellites on a Geostationary Orbit (GEO) are also being used as they offer multiple observations per hour but for a constant area, that often corresponds to a full-disk view of the earth (e.g., Himawari-8/AHI). Fire hotspot detection and identification (Engel et al., 2021a; Giglio et al., 2021; Wickramasinghe et al., 2020), fire intensity estimation (Engel et al., 2022; Xu et al., 2021, 2017), burned area estimation (Giglio et al., 2018; Roy et al., 2019), and fire severity assessment metrics (Gibson et al., 2020) are among the applications that highlight the importance and opportunities that these observations offer.

Fire activity and hotspot detection capabilities using GEO and LEO satellites have been studied through LEO-vs-LEO (Fu et al., 2020) and LEO-vs-GEO product intercomparisons (Engel et al., 2021b), comparing errors of omission and commission and FRP retrieval capabilities. Generally, MOD14/MYD14 have been shown to detect more fire hotspots than GEO satellite products when given the same observation opportunities (e.g., clear line-of-sight, appropriate satellite and sensor location over the fire), and especially when these fires are burning with low intensity (Engel et al., 2021b; Xu et al., 2021, 2017). When products that implement the Fire Thermal Anomaly (FTA) algorithm (Wooster et al., 2015) derived from the GOES-16 geostationary satellite over the Americas are compared to MOD14/MYD14 (Xu et al., 2021), they report

68% omission and 12% commissions errors. The omission error is mainly attributed to undetected low intensity fires which, when excluded from the assessment, reduce the omission error to 37% (Xu et al., 2021). Similarly, the adapted FTA algorithm product for Himawari-8's Advanced Himawari Imager (AHI) reported a 66% omission error and an 8% commission error in comparison to MOD14/MYD14, across East Asia and Australia and different land covers for June 2015 (Xu et al., 2017).

A recently developed algorithm for the AHI data, the Biogeographical Region and Individual Geostationary HHMMSS Threshold (BRIGHT) (Engel et al., 2021b), uses a different approach to fire detection compared to FTA. Its latest version has slightly reduced omission and commission errors for Australia reporting 54% and 5% respectively when compared to MOD14/MYD14 from April of 2019 to March 2020 (Engel et al., 2021a). This error is again attributed to lower intensity fires being missed due to the lower spatial resolution of the GEO products, but differs from previous studies as the study period was considerably longer, capturing an entire year of observations across the whole of Australia. (Engel et al., 2021a) also showed that the agreement between the two datasets in terms of probability of fire detection increases with increasing minimum fire intensity throughout a fire event.

One particularly important element of attributing and measuring fire intensity and activity is Fire Radiative Power (FRP). This corresponds to the upwelling energy emitted by a fire and is used to inform combustion completeness, burning biomass emissions, severity, and impact of wildfire (Freeborn et al., 2014b; Li et al., 2019b; Shen et al., 2021; Wooster et al., 2005, 2003). A detailed diurnal estimation of FRP can be integrated to compute the Fire Radiative Energy (FRE) of a fire and alongside other satellite sensor derived variables (e.g., Aerosol Optical Depth) used to make an alternative biome specific emission estimation without the need of certain assumptions and hard to acquire variables, such as fuel density and consumption rates (Ichoku and Ellison, 2014; Ichoku and Kaufman, 2005; Nguyen and Wooster, 2020). (Xu et al., 2017) compared GEO FRP estimates with established products, such as MOD14/MYD14, for different parts of the world and land covers. They found that more recent GEO sensors such as H8-AHI can provide FRP estimations more reliably than older platforms such as FY-2 and MTSAT. AHI showcased an almost perfect correlation with MOD14/MYD14 (R^2 = 0.98) on a per-fire level across East Asia and Australia for June 2015, where per-fire refers to a cluster of spatially-adjacent and near-simultaneous fire pixels.

Currently, only the two studies mentioned above (Xu et al., 2021, 2017) have moved past the detection error comparison and intercompared FRP derived from GEO and LEO sensors. These studies compare aggregations of FRP estimations from each sensor that correspond to specific fire event/clusters or 0.5^o grid aggregations. Nevertheless, conclusions from these studies are limited as they cover one and two months respectively, while focusing on large area spatial patterns.

This study intercompares the BRIGHT_AHI FRP product (Engel et al., 2022) to MOD14/MYD14 during the extreme Black Summer Fires event in south-eastern Australia (November 2019- March 2020). The two FRP products are compared through different temporal and spatial constraints to explore the agreement in concurrent hotspot FRP estimations (per-pixel) and diurnal FRP variations in bio-regional and seasonal settings.

2.2.Methods

2.2.1. Data

The FRP Level 2 MODIS products (1km spatial resolution) MOD14 from the TERRA and MYD14 from AQUA satellites (Thermal Anomalies/Fire) were accessed. MOD14/MYD14 is included in the latest MODIS data releases and remain unchanged between Collection 6 and 6.1. Nevertheless, a small percentage of pixels (~0.1%) have changed cloud cover status due to improvements in the processing of the relevant spectral channels (Giglio et al., 2021). The FRP calculation is based on the methodology proposed by (Wooster et al., 2003), which utilises the MIR channel centred at $4\mu m$ and is heavily dependent on the accurate characterisation of the identified hotspot's background MIR radiance (Giglio et al., 2016). In addition to the typical image granule format (HDF), NASA's Fire Energetics and Emissions Research (FEER) website offers Collection 6 data in tables (ASCII) including the coordinates, timestamp and variables for each hotspot (FEER, 2021). The FEER data was used in this study.

To reduce known errors in hotspot detection and FRP intercomparison, MOD14/MYD14 data were limited to narrower than the full scan angle, as this is known to affect the detection and retrieval capabilities with the increasing pixel size towards the scan edge (Engel et al., 2021b, 2021a; Freeborn et al., 2014a; Roberts et al., 2015; Xu et al., 2021, 2017). For comparison and consistency with the existing literature purposes, MOD14/MYD14 hotspots were filtered to those retrieved from pixels with a scan angle between 0^o and 30^o, which results in a maximum increment of the MOD14/MYD14 pixels by 1.7-times compared to their size at nadir.

BRIGHT_AHI FRP estimations derived from Himawari-8 imagery were also collected. Himawari-8 sits in a geostationary orbit (140.7º E) and through the Advanced Himawari Imager (AHI) sensor, provides data for the whole disk in 10-minute intervals in 16 spectral bands of varying spatial resolutions from 500m to 2km IFOV. The BRIGHT_AHI hotspot detection algorithm (Engel et al., 2021b, 2021a) provides FRP estimations at hotspot locations at ~2km spatial resolution. The same algorithm as MOD14/MYD14 (Wooster et al., 2003) is used for this step (Engel et al., 2022), utilising the Middle Infrared spectral band from AHI (MIR at 3.9 μm) to derive the FRP values at hotspot locations.

2.2.2. Study area and duration

The study was conducted across south-eastern Australia, specifically along forested areas impacted by the Black Summer Fires during Southern Hemisphere summer (2019-2020). Nine biogeographical regions (or bioregions) as defined by the Interim Biogeographic Regionalisation for Australia (IBRA) framework that were affected by the Black Summer Fires were selected as the study area for the period between 1/11/2019 and 31/3/2020 (Figure 2.1). IBRA is a commonly used segmentation of the continent into regions of similar biophysical characteristics (DAWE, 2000). The analysis was conducted across multiple spatial scales: the entire study area, for each bioregion, for individual wildfire events/clusters and on a pixel level. At the bioregion scale the analysis includes only the NSW North Coast, Sydney Basin and South East Corner bioregions as they have the highest forest cover and highest fire activity according to the two datasets (Table 2.1).

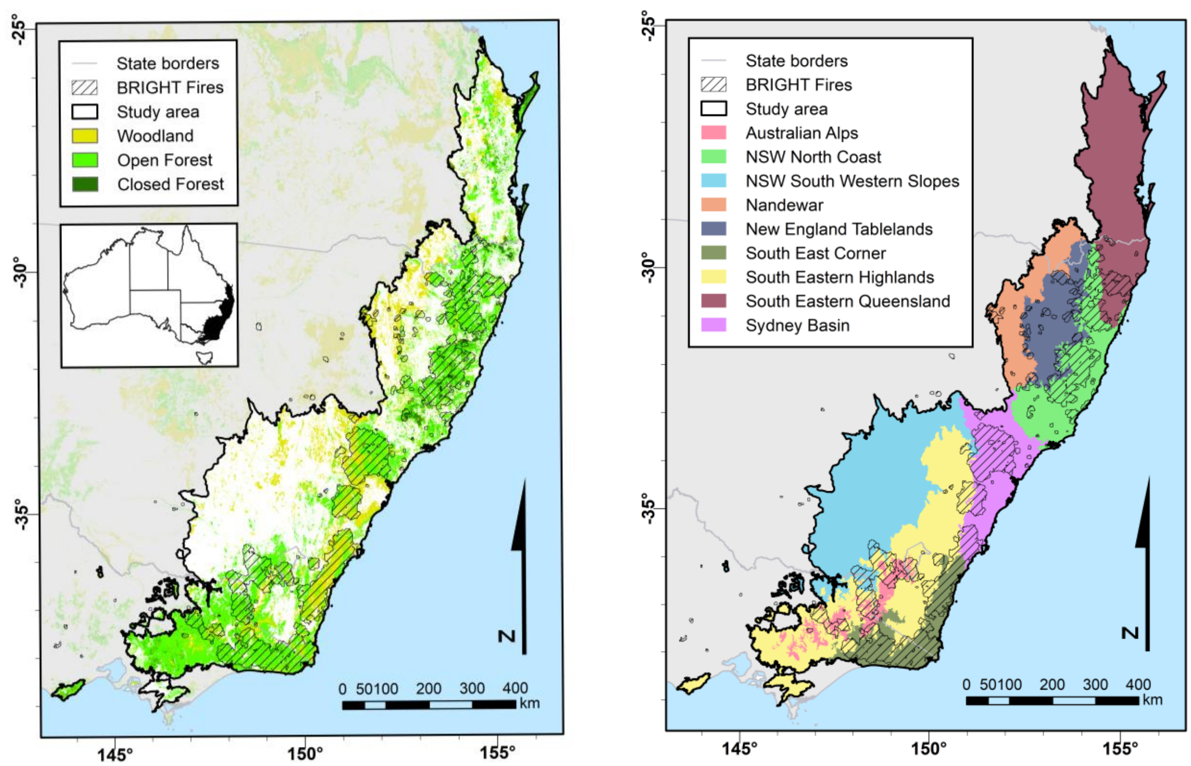

Figure 2.1 Map of study area with the different forest cover types (SOFR, 2018) (left) and different biogeographic regions (DAWE, 2000) (right).The areas that correspond to single fire events in VIC and NSW are highlighted in both maps as derived the methodology described in (Lizundia-Loiola et al., 2020) .

Table 2.1. Size of IBRA Bioregions used in the study area, proportion of forest within, and their administrative setting (Australian Capital Territory – ACT, New South Wales – NSW, Victoria – VIC).

Bioregion	Area (sq km)	Forest Cover (%)	State
Australian Alps	12330	8.5	NSW, VIC
Nandewar	27020	0.9	NSW, QLD
New England Tablelands	30022	4.6	NSW, QLD
NSW North Coast	39966	9.9	NSW
NSW South Western Slopes	86811	0.3	NSW, VIC
South East Corner	25320	13.4	NSW, VIC
South Eastern Highlands	83760	3.3	NSW, VIC
South Eastern Queensland	68421	1.9	QLD
Sydney Basin	36296	11.7	NSW

2.2.3. Intercomparison of BRIGHT_AHI and MOD14/MYD14 FRP values

The first level of comparison between BRIGHT_AHI and MOD14/MYD14 was performed on the entire study area by grouping the hotspots (pixel centroids) using spatial and temporal proximity constraints. The bioregion level stratification was used to spatially group the hotspots, while a temporal separation was implemented using discrete calendar months. For each bioregion and calendar month, diurnal cycle plots were created using the total number of hotspots, along with the averaged and summed (integrated) FRP estimations per hour (local time) as an appropriate visualization tool that would uncover the general trends.

An additional level of fire-hotspot spatial grouping was achieved through the spatiotemporal clustering of the BRIGHT_AHI fire pixels into superclusters as reported in (Ramsey et al., 2021) based on the work by (Lizundia-Loiola et al., 2020). A supercluster refers to a group of spatially (within a 3.6km radius) and temporally (2-hour window) connected fire pixel centroids that are assumed to represent a single fire event from ignition to extinguishment. The superclusters were used to further intercompare BRIGHT_AHI and MOD14/MYD14 using their FRP estimates for the spatial extent and duration of specific events. Two different approaches were examined, one integrating and comparing all hotspots from both datasets in a supercluster's footprint and duration, and a second including only concurrent hotspots from both datasets that were observed within 10 minutes of each other.

2.2.4. Grid alignment between BRIGHT_AHI and MOD14/MYD14

The comparison of two products with different spatial resolutions usually requires some grid reprojection for the measurements to correspond to the same area and location on the earth's surface. The differences are more prominent when the products are derived from sensors with different orbits, scan angles and point spread functions. As such, MOD14/MYD14 pixels were aggregated to match the lower spatial resolution grid of BRIGHT_AHI (~2km^2) and from hereon will be referred to as MD14_agg. A modification of the superellipse model (also known as Lamé Curve or Oval - (Gridgeman, 1970)) was used to define the neighbourhood of each BRIGHT_AHI pixel centroid, to approximate the elongated rectangular pixels of the sensor (Equation 1). Any concurrent MOD14/MYD14 pixel centroids that were located inside the superellipse were summed to provide a single aggregated FRP value for the area. The temporal threshold used to define concurrent spatiotemporal matches between the two datasets was ±10 minutes.

The superellipse neighbourhood was given by the inequality:

$$\left|\frac{x_{AHI}-x_{MOD}}{a+h}\right|^p + \left|\frac{y_{AHI}-y_{MOD}}{b+h}\right|^p \leq 1 \qquad \textit{Eq 2.1}$$

Where x and y are the coordinates of the BRIGHT_AHI and MOD14/MYD14 pixel centroids, a and b are the values of the major and minor axis of the superellipse that approximates the BRIGHT_AHI pixel axes lengths within the study region, and p is the curvature coefficient of the model. The p=1 represents a rhombus, p=2 represents a normal ellipse and p→∞ approximates a rectangle. The h was used as a buffer constant that increased the size of the superellipse by half a MOD14/MYD14 pixel to account for pixel area (but not centroid) overlap and was set to 0.005 decimal degrees.

2.2.5. Intercomparison of BRIGHT_AHI and MD14_agg spread patterns and FRP values

The association of the matched hotspots was examined through their correlation using Pearson's correlation coefficient *(r)*, as the two products are estimations of the same variable and therefore their relationship is expected to be linear. Following the work by (Xu et al., 2021, 2017), the best-fit linear model that passes through the origin was also calculated for the log-transformed data to satisfy the normality assumption of the Ordinary-Least-Squares regression (OLS) and be consistent with the literature. In addition, the matched hotspots were compared in terms of their location and ignition date, which was calculated based on the first logged FRP measurement in the time series of the stable BRIGHT_AHI pixel centroid location.

2.3.Results

2.3.1. BRIGHT_AHI vs MOD14/MYD14

The frequency distribution for the different sensor hotspot retrievals (Figure 2.2) depicts the temporal coverage difference between the two platforms over the diurnal cycle. BRIGHT_AHI reports considerably more hotspots per hour than MOD14/MYD14 on their concurrent hours, but this should be interpreted after considering the temporal resolution (BRIGHT_AHI makes six retrievals per hour versus a four retrievals per day by MOD14/MYD14) and spatial resolution (BRIGHT_AHI's pixels are two to four times larger than MOD14/MYD14) differences. However, BRIGHT_AHI detects significantly fewer hotspots per hour between 06:00 and 19:00 compared to 20:00-05:00 (Figure 2.2), which roughly corresponds to a day/night difference.

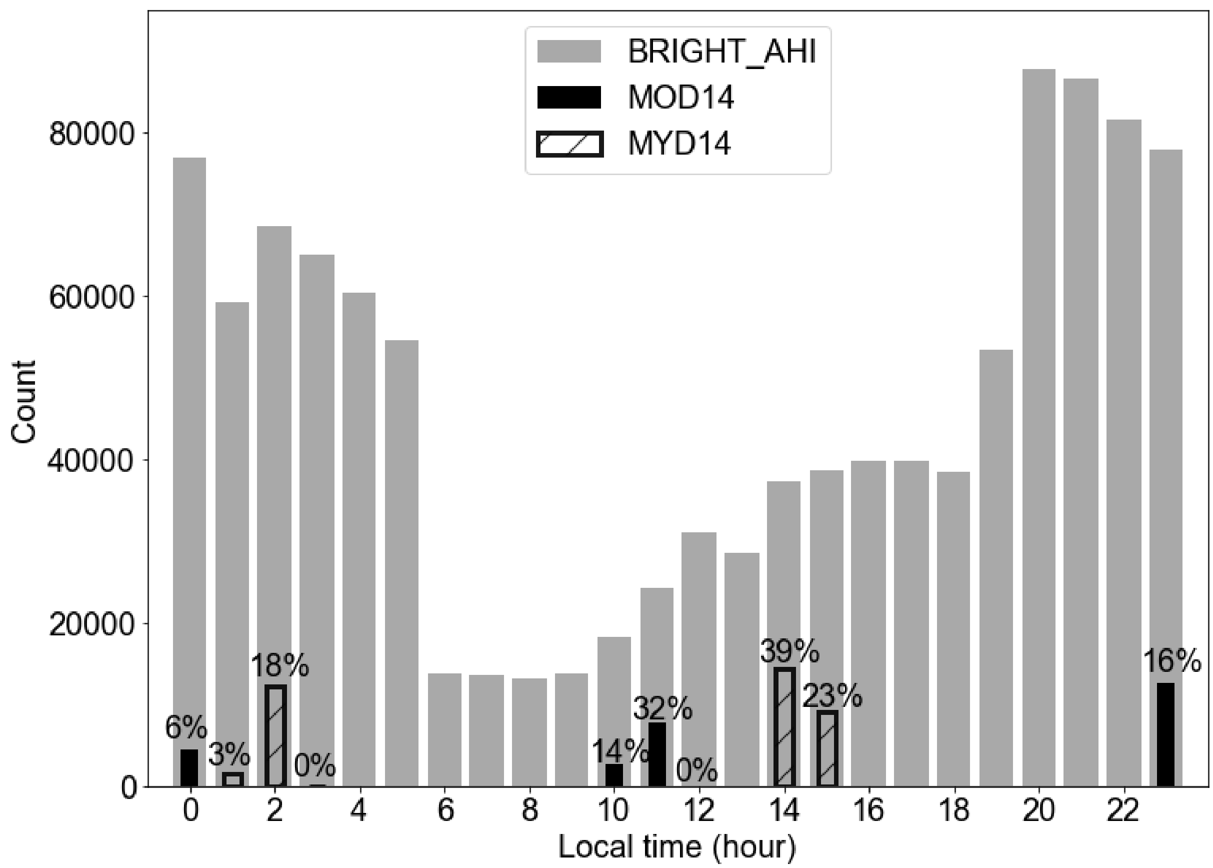

Figure 2.2 Frequency distribution of hotspot numbers per retrieval time during the Black Summer fires (November 2019 - March2020). The percentage captions over the MOD14 and MYD14 hotspot bars indicate their proportion against the reported BRIGHT_AHI hotspot numbers in the one-hour window.

A clear difference in the number of hotspots between BRIGHT_AHI and MOD14/MYD14 products is detected (Figure 2.3 a, b). Integrated FRP values demonstrate a similar trend (Figure 3 c, d), where observations from both sensors are available, with a dip in the morning hours and an increase from 10:00 to 15:00. Meanwhile, the mean FRP values fluctuate with a similar magnitude and trend, peaking around 15:00. Finally, an inverse relationship between the number of hotspots and their average and integrated FRP is evident in the BRIGHT_AHI data, alternating between day and night (Figure 2.3 a, c).

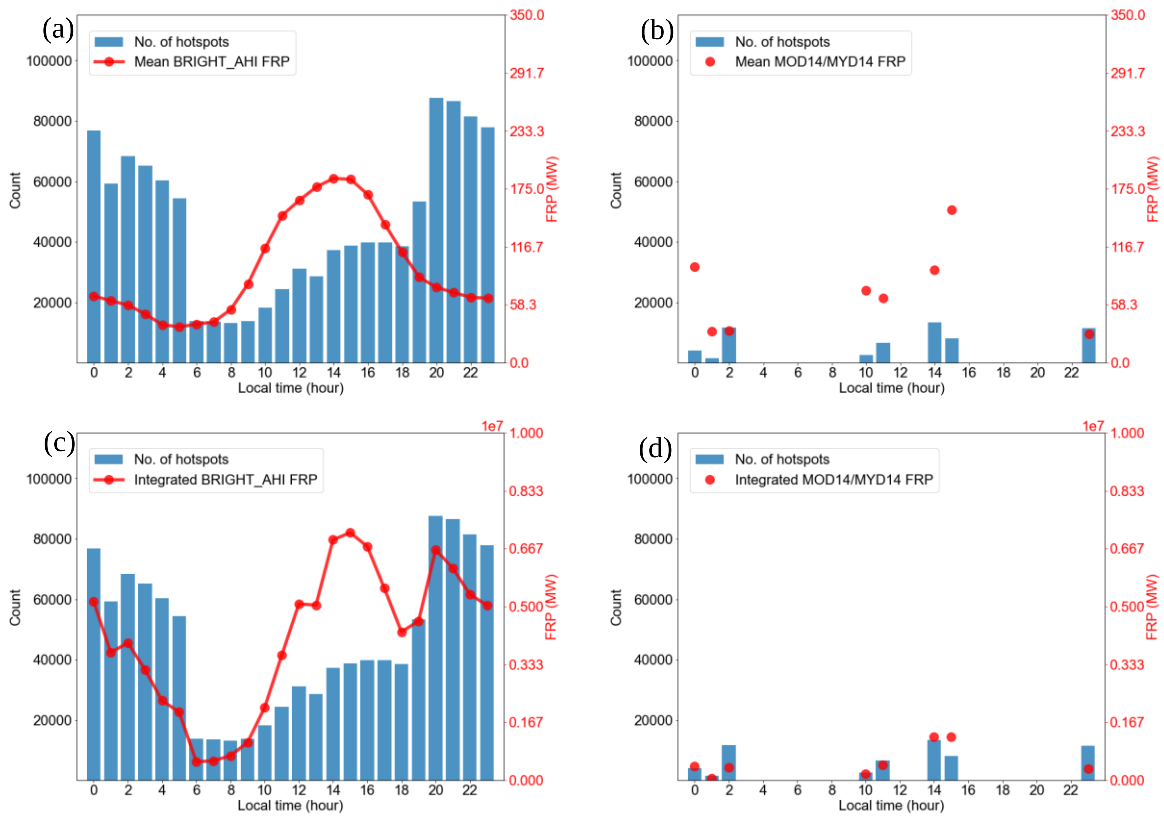

Figure 2.3 Aggregated diurnal cycles of hotspot numbers overlayed by Mean and Integrated FRP values for the BRIGHT_AHI (a), (c) and MOD14/MYD14 (b), (d) sensors. The data are grouped on hourly intervals and represent the entirety of the Black Summer fires (November 2019 – March 2020).

A further break down of the dataset per month and bioregion reveals specific temporal patterns. As seen in Figure 2.4, there is a clear gradient indicating that at the beginning of the fire season (November) the majority of hotspots were in the northern regions (NSW North Coast). A month later most hotspots were in the central region (Sydney Basin) and another month later the southern region South East Corner had more hotspots than the other areas.

Figure 2.4 Aggregated diurnal cycles of Mean FRP from BRIGHT_AHI over number of hotspots between November 2019 and January 2020 for the three analysed bioregions which follow a north to south latitudinal gradient (NSW North Coast – top row; Sydney Basin – middle row; South East Corner – bottom row). From left to right the progression depicts the temporal change (November to January), while from top to bottom spatial change (Bioregions from North to South).

When compared to BRIGHT_AHI, the number of hotspots from MOD14/MYD14 is lower with the resultant loss of fire activity information. However, a similar trend in hotspot spatial-temporal incidence can be seen in the data (Figure 2.5). Mean MOD14/MYD14 FRP values are underestimated compared to BRIGHT_AHI (Figure 2.4).

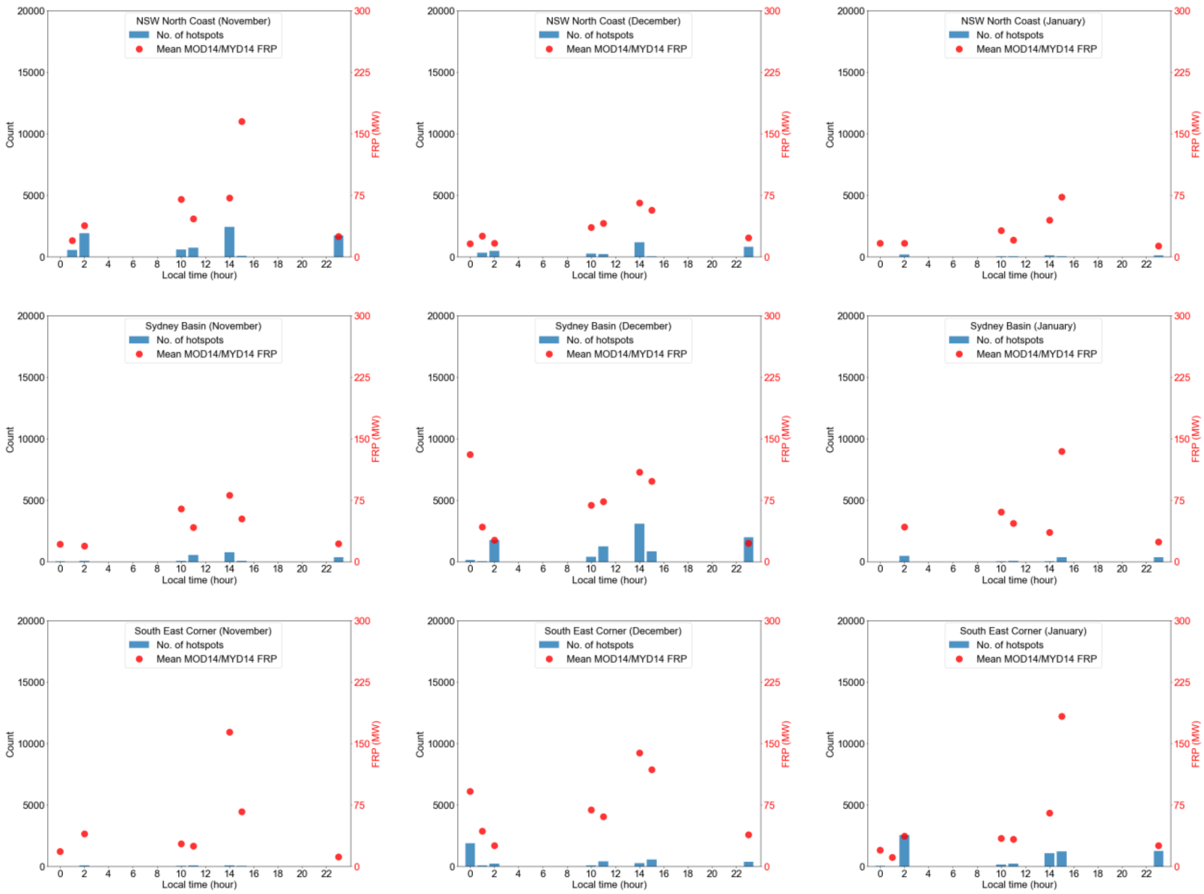

Figure 2.5 Aggregated diurnal cycles of Mean FRP from MOD14/MYD14 over number of hotspots between November 2019 and January 2020 for the three analysed bioregions which follow a north to south latitudinal gradient (NSW North Coast – top row; Sydney Basin – middle row; South East Corner – bottom row). From left to right the progression depicts the temporal change (November to January), while from top to bottom spatial change (Bioregions from North to South).

Figure 2.6 replicates the fire season progression (November, December 2019, January 2020) and study bioregions presented in figures 4 and 5. As per the trends in hotspot numbers, fires became more intense over time and progress towards the south, while their intensity reduced over time in the north. An irregular jump of the FRP is observed in South East Corner for night-time observations in December 2019.

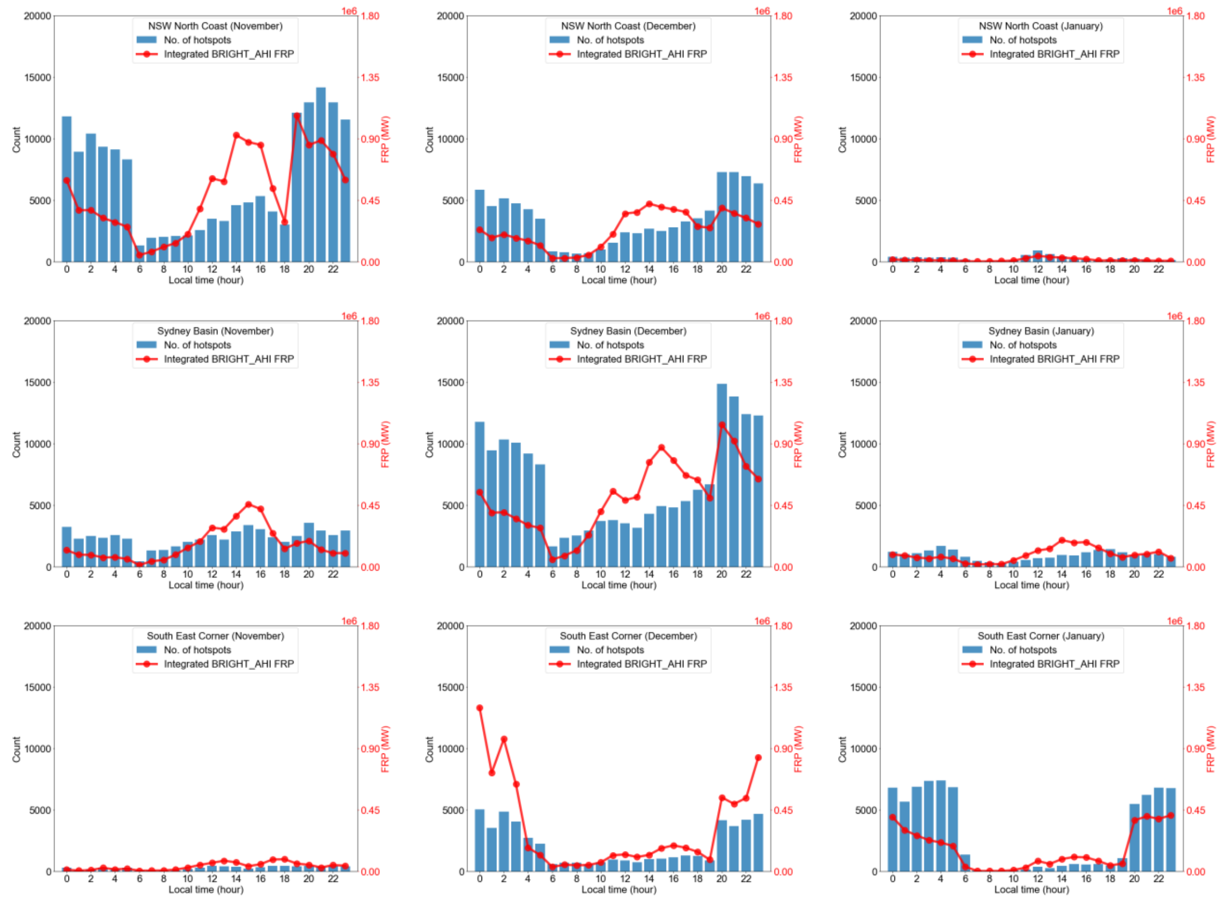

Figure 2.6 Aggregated diurnal cycles of Integrated FRP from Himawari-8 over number of hotspots between November 2019 and January 2020 for the three analysed bioregions which follow a north to south latitudinal gradient (NSW North Coast – top row; Sydney Basin – middle row; South East Corner – bottom row). From left to right the progression depicts the temporal change (November to January), while from top to bottom spatial change (Bioregions from North to South).

MOD14/MYD14 depicts similar spatial and temporal trends as BRIGHT_AHI (Figure 2.7), but these are smaller in magnitude. The night-time peaks measured by BRIGHT_AHI during November in NSW North Coast and December in Sydney Basin and South East Corner are not captured by MOD14/MYD14.

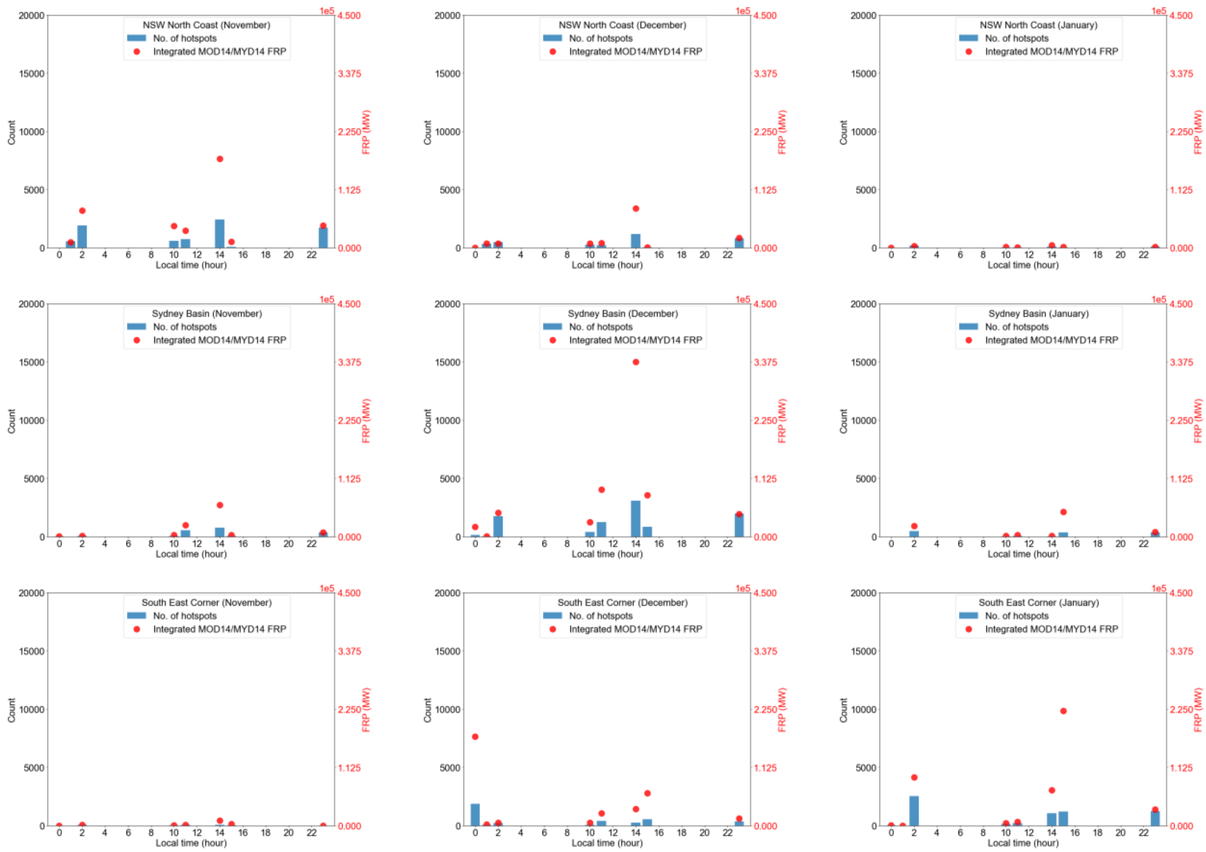

Figure 2.7 Aggregated diurnal cycles of Integrated FRP from MOD14/MYD14 over number of hotspots between November 2019 and January 2020 for the three analysed bioregions which follow a north to south latitudinal gradient (NSW North Coast – top row; Sydney Basin – middle row; South East Corner – bottom row). From left to right the progression depicts the temporal change (November to January), while from top to bottom spatial change (Bioregions from North to South).

2.3.2. BRIGHT_AHI vs MOD14/MYD14: Fire superclusters

Using the fire superclusters (for derivation see Methods), BRIGHT_AHI continues to offer a more complete picture of fire intensity and hotspot numbers (Table 2.2). As seen in Figure 2.8 and Table 2.2, the NSW North Coast supercluster as captured by BRIGHT_AHI is consistent with the results from the bioregional level analysis (Figure 2.4), with a peak of intensity between 10:00-14:00, unlike MOD14/MYD14 that misses the FRP variation. Meanwhile, MOD14/MYD14 successfully indicates the increase in intensity between 11:00 and 14:00 for the Sydney Basin supercluster, but with less detail than BRIGHT_AHI. The intensity during the South East Corner fire supercluster is the highest measured out of the three events as observed by BRIGHT_AHI, while MOD14/MYD14 failed to capture any data at this location/time.

Table 2.2 Superclusters of three chosen fire events, with the highest Mean FRP, Integrated FRP, number of hotspots and longest duration of fire in hours.

Start	End	Duration (h)	Area (sq km)	Integrated FRP (MW)	Mean FRP (MW)	No. of hotspots	Bioregion
05/11/2019 5PM	09/11/2019 11PM	102	2871	3314865	138.0	30576	NSW North Coast
11/11/2019 6AM	15/11/2019 11PM	113.5	1607	1925086	61.8	31807	Sydney Basin
29/12/2019 10PM	30/12/2019 11PM	25.3	5051	3122205	382.7	11612	South East Corner

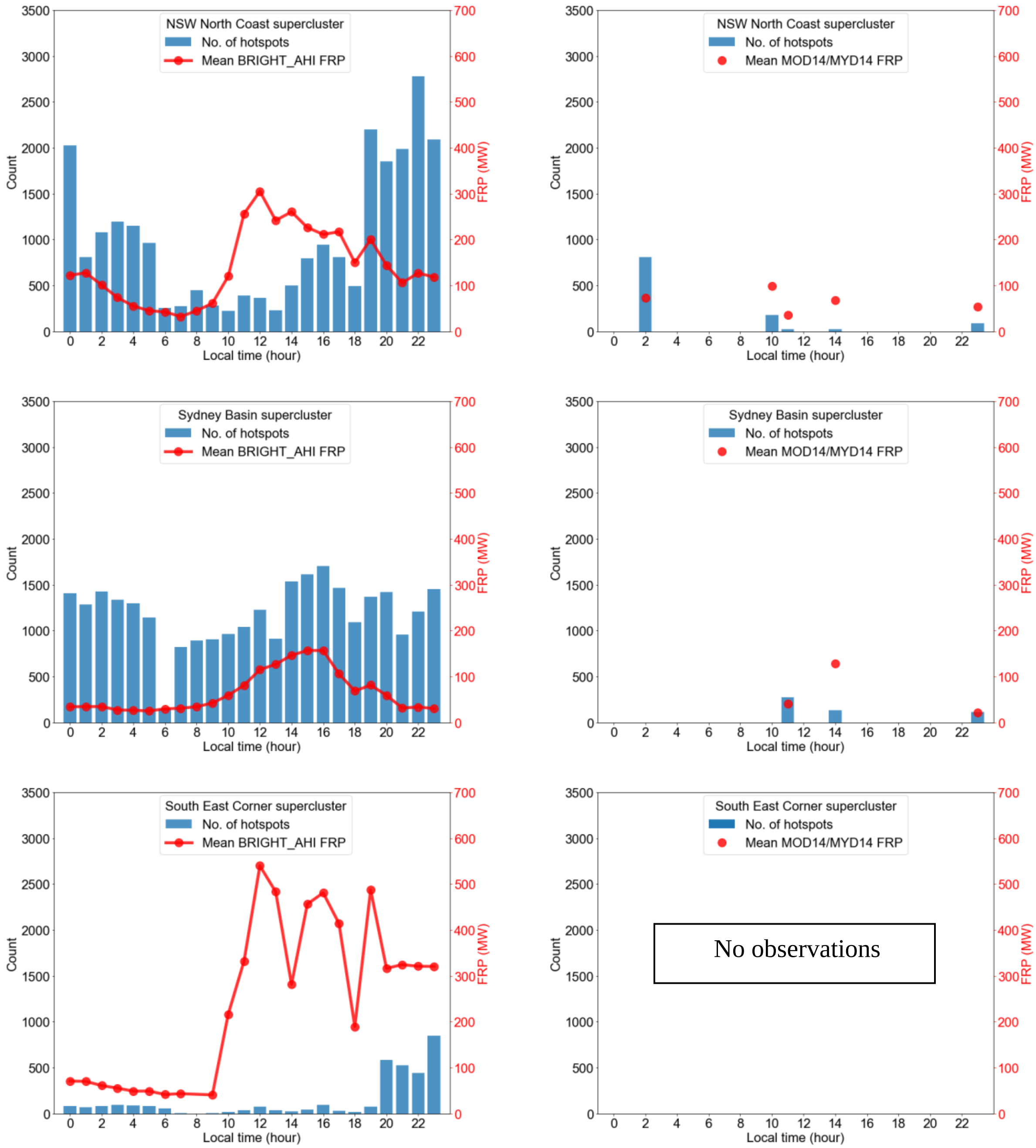

Figure 2.8 Comparison of aggregated diurnal cycles of Mean FRP from BRIGHT_AHI (left column) and MOD14/MYD14 (right column) during the three fire superclusters analysed at the bioregion level (NSW North Coast – top row; Sydney Basin – middle row; South East Corner – bottom row).

Next, the association of the total FRP per supercluster was examined for BRIGHT_AHI and MOD14/MYD14 (Figure 2.9). The correlation between the two datasets is moderate positive when all hotspots in a supercluster are integrated and compared ($r = 0.67$, $p < 0.01$, slope = 1.38), with BIRGHT_AHI logging higher total values due to its more frequent observations. Meanwhile, the observed correlation is lower (r = 0.49, p < 0.01, slope = 1.29) when only hotspots that are concurrently observed by both datasets within 10 minutes of each other are integrated, and the bias towards BRIGHT_AHI FRP is reduced.

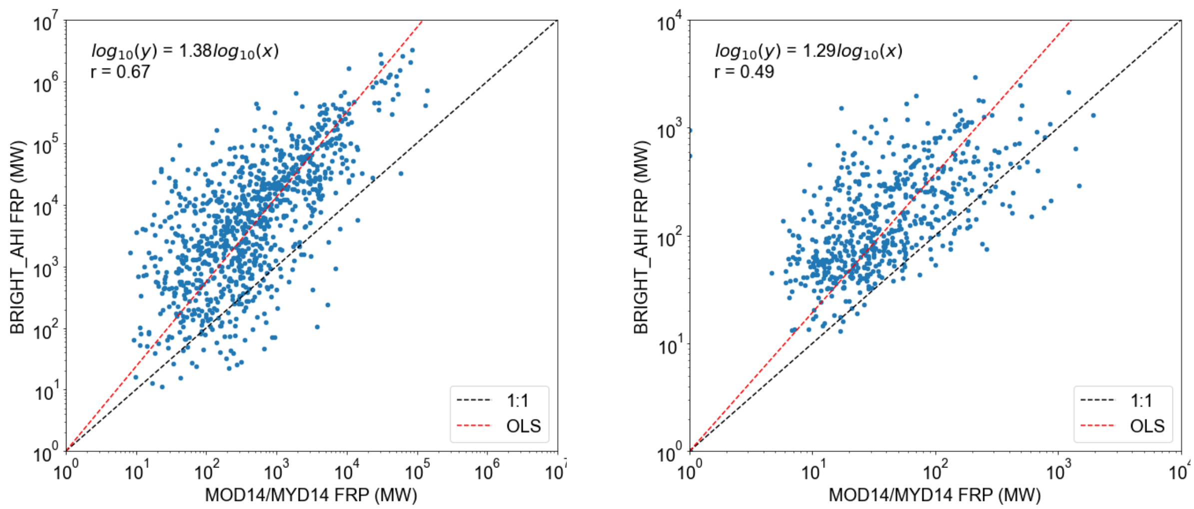

Figure 2.9 BRIGHT_AHI and MOD14/MYD14 FRP aggregations at supercluster/fire event locations and association statistics, namely the slope of the fitted linear model passing through the origin and Pearson's r. The scatterplots correspond to the integrated FRP values for the duration of the event (left) and the integrated FRP values only for concurrent hotspots (right) per-fire supercluster as measured by each product.

2.3.3. BRIGHT_AHI vs MD14_agg

Over 9,0000 concurrent hotspots, between BRIGHT_AHI and MD14_agg, were identified for the nine bioregions used in this study. A strong positive correlation between the FRP products (r = 0.74, Figure 2.10) was observed, while the linear model passing through the origin and applied on the log-transformed data was fitted with a slope of 0.87. Despite the strong correlation, BRIGHT_AHI still underestimates the FRP values and saturates at around 950MW.

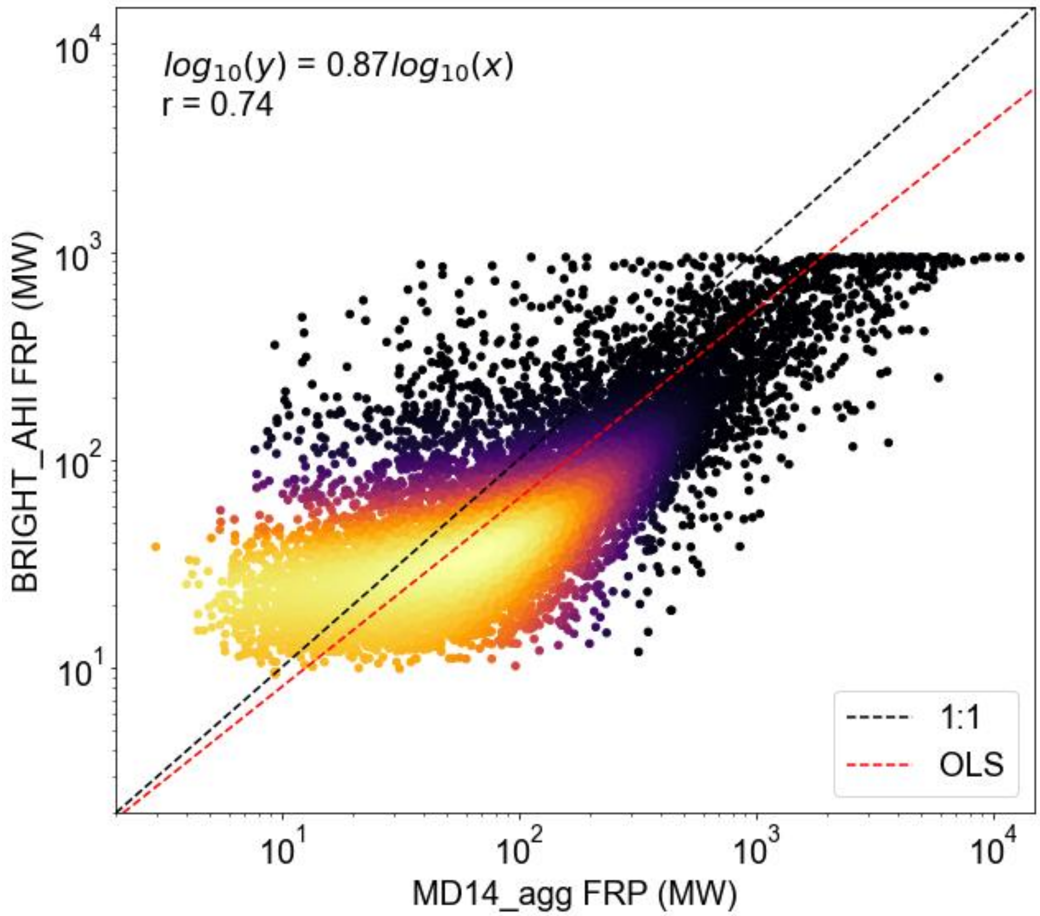

Figure 2.10 Scatter plot of BRIGHT_AHI and MD14_agg FRP at spatially (superellipse neighbourhood) and temporally (±10 minutes) concurrent hotspots in logarithmic scale. The colour gradient depicts the kernel density of the points in the plot, where lighter colours denote higher density and darker colours a lower density. This is meant as a qualitative visualisation aid rather than a quantifiable parameter.

Figure 2.11 illustrates the spatiotemporal progression of the fire for BRIGHT_AHI and MD14_agg in the form of a 2D histogram. The plots show that fires spread from North to South and from East to West (length of artifacts along the y-axis). Most distance was covered during the last week of December and the first week of January, where fire ignitions peaked through 2^{o} of latitude and 2.5^{o} of longitude. From beginning to end, December had the largest number of ignitions (length of artifacts along the x-axis) especially along the 150^{o} meridian, which corresponds to the Sydney Basin IBRA region of the study area.

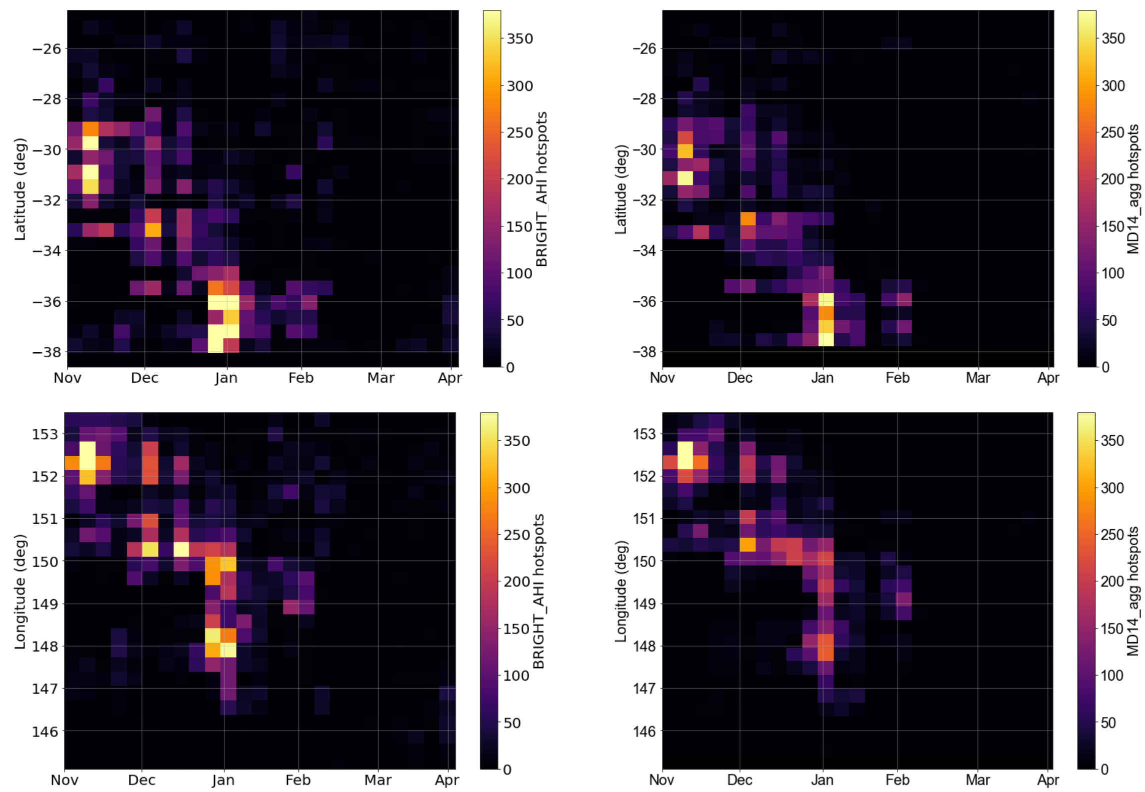

Figure 2.11 Heatmap of first detection dynamics by latitude (top row) and longitude (bottom row), BRIGHT_AHI hotspots (left column) and MD14_agg (right column). Plot axes correspond to coordinate (y-axis) and time (x-axis). The colour gradient shows the density of hotspot pixels for each point in time and space.

On a bioregion level, the two datasets remain positively correlated with values ranging from 0.69 to 0.86 as reported in Table 2.3. Pearson's r is higher in NSW North Coast and Sydney Basin, and slightly lower in the South East Corner bioregion, compared to the overall correlation ($r = 0.74$, $p < 0.01$).

Table 2.3 Correlation and number of pairs per IBRA Bioregion for the BRIGHT_AHI and MD14_A FRP comparison.

Bioregion Name	Number of Pairs	*r*
Australian Alps	409	0.73
Nandewar	137	0.83
New England Tablelands	1122	0.7
NSW North Coast	1919	0.84
NSW South Western Slopes	282	0.7
South East Corner	1304	0.69
South Eastern Highlands	1152	0.74
South Eastern Queensland	643	0.86
Sydney Basin	2082	0.79

2.4. Discussion

Fire Radiative Power estimations from LEO (MOD14/MYD14) and GEO (BRIGHT_AHI) sensors were compared using different spatial and temporal constraints at three spatial aggregations. General agreement between FRP estimates was observed for bioregion (first level) and fire event (second level) stratifications of the data, with BRIGHT_AHI providing more detailed diurnal information due to its higher temporal resolution. Meanwhile, high agreement was shown in the fire spread patterns captured by each sensor and detection algorithm. A strong positive correlation was also shown in concurrently observed fire hotspots by both datasets that is significant given the sensor and orbit differences (third level). This overall agreement is supportive of the legitimacy of BRIGHT_AHI detections and the utility of AHI to derive measures of FRP when compared to a higher spatial resolution product.

BRIGHT_AHI and MOD14/MYD14 were first compared according to month and bioregion. BRIGHT_AHI showed clear advantages over MOD14/MYD14 in the diurnal cycle analysis, where the former's high temporal resolution allowed for temporal patterns to be captured in detail while fewer insights were able to be extracted from the latter (e.g., Figure 2.3). This is to be expected as Himawari-8's AHI has 144 opportunities per day to capture the earth's surface compared to the four of the MODIS satellite pair. Nevertheless, a significant difference in the number of hotspots between day and night-time was documented for BRIGHT_AHI, which is a finding consistent with (Engel et al., 2021a) and (Engel et al., 2021b). Furthermore, in the case of cloud presence during the overpass of the satellite, entire fire event can be missed (e.g., fire supercluster in South East Corner –Figure 2.8) or sporadic high intensity fire activity during the night-time compared to daytime can also be omitted (e.g., South East Corner during December – Figure 2.6). The absence of an albedo check in the night-time BRIGHT algorithm relaxes detection rules thereby increasing hotspot detections and potentially the rate of commission errors.

For the second level of intercomparison between the datasets, an alternative spatiotemporal constraint based on the work by (Lizundia-Loiola et al., 2020; Ramsey et al., 2021) was applied using superclusters that corresponded to specific fire events. Here, it was observed that MOD14/MYD14 data underrepresented or completely omitted the fire activity (Figure 2.8), unlike BRIGHT_AHI that provided consistent information for all the events. In the case of the South East Corner supercluster, a small number of BRIGHT_AHI hotspots along with high FRP values were measured, while MOD14/MYD14 missed the entire event. To further explore this, the cloud cover during the event was visually inspected using Japan's National Institute of Information and Communications Technology (NICT) website (https://himawari8.nict.go.jp/). There it was observed that in the early morning and afternoon, both clouds and smoke were present covering parts of the coast, while the sky was clear only during the late morning of 30/12/2019. This could mean that MOD14/MYD14 did not observe this extreme event due to cloud and smoke contamination during the AQUA/TERRA overpasses, unlike BRIGHT_AHI that managed to provide information throughout the day utilising clear-sky moments.

The third level of comparison was implemented on a pixel level, using a superellipse neighbourhood to better match the MOD14/MYD14 smaller IFOV to the coarser and differently shaped BRIGHT_AHI pixels. As a result, the "double counting" of MOD14/MYD14 hotspots with multiple adjacent BRIGHT_AHI was reduced for the pixel matching process, better aligning the different grid systems of the two products compared to a simpler model, e.g., Euclidean distance (circle). Further quality considerations for the neighbourhood definition include the varying pixel shape of BRIGHT_AHI across the observed disk, an artifact of the Earth's curvature and AHI's orbit. Adjustments to the dimensions of the superellipse in terms of rotation, minor and major axis length could be made when applied in continental scales to keep the pixel matching consistent. Nevertheless, the distortion introduced by the sub-state size of the study area presented here was assumed insignificant and therefore the superellipse method had high utility.

To better appreciate the strong positive correlation (r = 0.74) between the two hotspot products for concurrent detections (Figure 2.10), variations in addition to the gridding systems should be considered. For example, while both products implement the same FRP calculation algorithm (Wooster et al., 2003), they each derive the background radiation differently during the hotspot detection stage. Background radiation is an important input in the model developed by (Wooster et al., 2003), and therefore it greatly affects the final FRP estimation. BRIGHT_AHI utilizes a series of dynamic seasonal, bioregional, and time-of-day thresholds to derive the background radiation for a given hotspot, whereas MOD14/MYD14 uses only spatially neighbouring "ambient" pixels from a single scene to separate the radiation from a fire hotspot from the radiation of the background. Furthermore, the fact that multiple MOD14/MYD14 observations are aggregated and compared to a single BRIGHT_AHI observation can exacerbate the differences in FRP magnitude that are caused by the difference in spatial resolution between AHI and MODIS. An example of this is the saturation at around 950MW for BRIGHT_AHI FRP that is attributed to the MIR AHI channel saturation at 400K (Hall et al., 2019), but also worsens through the MOD14/MYD14 aggregation, amplifying the positive bias towards the latter (Figure 2.10).

Finally, the fire spread patterns derived by the two products using the first ignition per pixel analysis revealed similar insights about the black summer fire season. Both datasets suggest that the fire started in the north and spread towards the south and south-east of the study area over time, following the findings of (Zheng et al., 2021). Our findings also indicate that most ignitions occurred in the south of the study area towards the end of December. This peak of ignitions corresponds to the South East Corner bioregion, which shows a low number of hotspots during daytime in December, but a large increase of hotspot number, mean and integrated FRP during the night-time (Figure 2.6) that is in agreement with the high night-time activity in East Victoria as documented by (Zheng et al., 2021).

Several studies have compared and combined GEO and LEO FRP products that focus on biomass burning emissions (Freeborn et al., 2009; Li et al., 2019b, 2018b; Mota and Wooster, 2018; Zhang et al., 2020). However, fewer studies focused in the intercomparison of FRP estimations from GEO and LEO sensors (Hyer et al., 2013; Xu et al., 2021, 2017). AHI and MOD14/MYD14 were compared in the work by (Xu et al., 2017), which was conducted for the whole disk for a single month (June 2015) and a hotspot aggregation to 0.5^{o} grid cells or specific fire event clusters spatial scales. In addition, (Xu et al., 2017) used the FTA algorithm (Wooster et al. 2015) to calculate the FRP from AHI data (FTA_AHI). These aggregations may be sufficient for extracting general differences and trends, however, in this study we also used AHI's native resolution to perform pixel-to-pixel overlap comparison. A higher resolution comparison allows for more detailed information about fire activity and how it is captured by different sensors to be produced.

As shown by (Engel et al., 2021a), the regionally tuned BRIGHT_AHI performs slightly better in terms of omission and commission errors compared to FTA_AHI, which uses global assumptions (Engel et al., 2021a; Xu et al., 2017). The statistics provided for the FRP value comparison in terms of concurrently observed fire event clusters suggest an almost perfect association between the two datasets used by (Xu et al., 2017) with a slope of 0.99 and an $R^2 = 0.98$. We found a 1.29 slope for the fitted linear model through the origin and a Pearson's r = 0.49 ($R^2 = 0.24$), suggesting a low/moderate association with a clear underestimation of FRP for MOD14/MYD14 when it comes to concurrently observed hotspots in the spatial extend of superclusters. When the data are compared on a fire supercluster level without a concurrency constraint, the association becomes stronger (r = 0.67, R^2 = 0.45), but the bias increases with a 1.38 slope for the fitted linear model towards BRIGHT_AHI (Figure 2.9) as a result of temporal resolution differences. Similar biases in direction and magnitude were also documented by Roberts et al. (2015), in an intercomparison of METEOSAT SEVIRI and MODIS FRP estimates for single fire events, over Europe, Africa and South America. This suggests that the GEO and LEO sensor spatial resolution differences are systematically influencing FRP estimates.

On the grid cell level, BRIGHT_AHI seems to perform better than FTA_AHI when both datasets are compared to MOD14/MYD14. Using a 0.5^o grid cell aggregation, (Xu et al., 2017)) found a slope of 0.54 for fitted linear model. Meanwhile here, BRIGHT_AHI shows a slope of 0.87 and a Pearson's r of 0.74 (R^2 = 0.55) on the pixel-by-pixel comparison with MOD14/MYD14 (Figure 2.9), in an approximately 20 times finer resolution grid than the one used in (Xu et al., 2017). The differences between BRIGHT_AHI and FTA_AHI in this context could be also be explained due to the fact that (Xu et al., 2017) used a shorter time period (1 vs 5 months), for different intensity events (mainly agricultural fires vs megafires), over a larger area (East Asia and Australia vs a sub-region of Australia). More research is needed to draw robust conclusions on algorithm suitability in different conditions.

2.5. Conclusions

The aim of this paper was to explore the capabilities and limitations of newly developed geostationary products for fire monitoring. FRP estimations from BRIGHT_AHI were compared to the widely used FRP retrievals from MOD14/MYD14 during the extreme Black Summer Fires that devasted South-Eastern Australia in 2019-2020. Intercomparison on a pixel level revealed a strong association between the two, something that increases the confidence of BRIGHT_AHI, whereas focusing on the temporal variability of FRP showcased an increased utility value when time dense measurements are available. Our findings suggest that geostationary products can be used in fire monitoring contexts which will also help enhance our understanding of wildfire dynamics from space.

Chapter 3. One year of near-continuous fire monitoring on a continental scale: Comparing Fire Radiative Power from polar-orbiting and geostationary observations

This chapter is based on: Chatzopoulos-Vouzoglanis, K., Reinke, K.J., Soto-Berelov, M., Jones, S.D., 2023. One year of near-continuous fire monitoring on a continental scale: Comparing fire radiative power from polar-orbiting and geostationary observations. International Journal of Applied Earth Observation and Geoinformation 117, 103214. https://doi.org/10.1016/j.jag.2023.103214

Abstract

Geostationary and polar-orbiting remote sensors have different opportunities to observe wildfires. While polar-orbiting sensors have been favoured in wildfire observations, geostationary sensors offer a higher observation frequency. Here, we assess the utility of the Himawari-8 AHI geostationary product and compare it to established polar-orbiting observations from TERRA/AQUA MODIS and SNPP VIIRS for 12 months of fire activity in Australia (2019-2020). Fire Radiative Power (FRP) estimates from AHI (BRIGHT/AHI) are compared to the MODIS (MOD14/MYD14) and VIIRS (VNP14IMG) polar-orbiting products, through varying spatial and temporal aggregations. Results suggest that all products capture similar wildfire dynamics across the continent. For near-simultaneously observed hotspots, the agreement is high between BRIGHT/AHI and the individual polar-orbiting products ($r = 0.74$-0.77, $p<0.01$). Land cover and region-specific comparisons show similar FRP estimate distributions between products, although with scale differences due to the varying spatial resolutions. Derived diurnal FRP cycles on the other hand, highlight the dense temporal information that BRIGHT/AHI offers in contrast to the other products. This is further emphasized with individual event comparisons, where BRIGHT/AHI reports fire activity continuously while the polar-orbiting products only offer fragmented observations when available. In conclusion, AHI observes similar spatiotemporal patterns and FRP estimation distributions to MODIS and VIIRS during different seasons across Australia. While BRIGHT/AHI's coarser spatial resolution underestimates the FRP estimations captured by its counterparts, its higher observation frequency demonstrates significant advantages. This analysis further raises the confidence in BRIGHT/AHI for

continuous wildfire monitoring across Australia while revealing new opportunities that take advantage of its denser observation record.

3.1.Introduction

Wildfires are important phenomena with major effects on local communities and ecosystems, but also on a global scale as they generate carbon emissions. Remote sensing has been used extensively throughout the last decades to detect and monitor wildfires using mostly Low-Earth Orbiting (LEO) platforms (Giglio et al., 2021; Schroeder et al., 2014; Xu et al., 2020). Meanwhile, sensors on GEOstationary (GEO) platforms have also been studied regarding their suitability for wildfire monitoring (Engel et al., 2021a, 2021b; Roberts and Wooster, 2008; Wickramasinghe et al., 2020, 2016; Xu et al., 2021, 2017, 2010).

Fire Radiative Power (FRP) describes the upward welling energy associated with a fire and may be considered a proxy for fire intensity (Kaufman et al., 1998; Wooster et al., 2005, 2003). Usually FRP is derived using the sensor's middle-infrared (MIR) channel centred around $4\mu m$ and the model developed by (Wooster et al., 2005, 2003); which has been used in several products such as the MODIS MOD14/MYD14 (Giglio et al., 2021), VIIRS VNP14IMG (Schroeder and Giglio, 2018) as well as the Advanced Himawari Imager (AHI) BRIGHT/AHI product (Engel et al., 2022).

LEO platforms usually revisit a specific location on the Earth twice a day, one during daytime and one during night-time. In contrast, GEO platforms offer continuous daily observations for a single location in their observed disk, but at the expense of lower spatial resolution. The trade-off between the spatial and temporal resolution of hotspot observations is important for understanding the benefits and limitations of each when observing fire in the landscape. Examples of intercomparisons between satellite sensors with different spatial and temporal resolutions are reported throughout the literature (Fensholt et al., 2011; Martínez et al., 2013; Wickramasinghe et al., 2020). Intercomparisons of FRP products have been conducted in LEO-vs-LEO (Li et al., 2018a) and LEO-vs-GEO (Xu et al., 2017) settings, usually on the basis of fire hotspot detection and FRP estimation capabilities (Engel et al., 2020; Fu et al., 2020; Xu et al., 2021, 2017). In general, GEO satellites omit smaller or lower intensity fires as a result of spatial resolution and saturation thresholds on the MIR channel (Hall et al., 2019). However, newer generation satellites (e.g., Himawari-8 AHI) have improved instruments with higher spatial resolution compared to older generation ones (e.g., METEOSAT-SEVIRI), and higher spatial resolution GEO sensors being developed (Wooster et al., 2021).

Hotspot comparison studies have demonstrated some of the limitations of GEO sensors for fire detection. For example, 90% of fire hotspots captured by the 375m VIIRS FRP product (VNP14IMG) were shown to be missed by the AHI product developed by the Japan Aerospace Exploration Agency (JAXA) in eastern China during 2019 (Chen et al., 2022), notably due to the region characterised mostly by smaller agricultural fires. Meanwhile, (Xu et al., 2017) developed their own product from AHI data using an adaptation of the Fire Thermal Anomaly (FTA) algorithm (Wooster et al., 2015) and found that AHI omitted 66% of the hotspots captured by MOD14/MYD14 across Eastern Asia and Australia for June 2015. The more recently developed AHI product for Australia called the Biogeographical Region and Individual Geostationary HHMMSS Threshold (BRIGHT) (Engel et al., 2021b) reported 54% omission errors compared to MOD14/MYD14 for the continent of Australia between April 2019 and March 2020 (Engel et al., 2021a).

Beyond the detection capabilities, studies have compared FRP estimations between LEO and GEO products for detected hotspots (Chatzopoulos-Vouzoglanis et al., 2022; Li et al., 2020b; Xu et al., 2021, 2017). Many such intercomparisons, whilst detailed in their description, are limited in their analysis to regional case studies (e.g., (Chatzopoulos-Vouzoglanis et al., 2022) or short time periods (Xu et al., 2017). To unpack the relative performance of FRP estimation capabilities, larger scale studies are required where the analysis can be applied across whole of continents and across seasons. In larger spatial-scale studies (Xu et al., 2017) FRP estimations are usually compared across different spatial subsets, with estimations resampled on coarser grids with the intention to be compared to emission inventories or used as inputs to atmospheric models (e.g., 0.5^{o} in Xu et al., (2017), 0.25^{o} in (Li et al., 2019a)), 0.1^{o} in (Andela et al., 2015))). Other aggregations include hotspot groupings into individual fire clusters (Roberts and Wooster, 2014) or broader regions (Chen et al., 2022). These studies also span across different study periods, ranging from days to months, enabling a detailed insight into relative performance.

When comparing coincident observations, LEO and GEO sensors have been shown to capture comparable FRP trends and magnitudes. For instance, during the extreme wildfire season of the Black Summer of 2019-2020 in south-eastern Australia (Fryirs et al., 2021), (Chatzopoulos-Vouzoglanis et al., 2022) found moderate and strong positive correlations of FRP estimations to exist between coincident observations of AHI (BRIGHT/AHI) and MODIS (MOD14/MYD14) when examining individual fire clusters and hotspot-to-hotspot comparison, respectively. Meanwhile, (Xu et al., 2017) found almost perfect agreement with a very strong positive correlation between Himawari-8 (FTA) and MODIS FRP (MOD14/MYD14) estimations during June 2015 across a variety of land covers in East Asia and Australia. (Xu et al., 2021) also demonstrated that in the Americas, GOES-13 and GOES-16 have high agreement for near-coincident FRP observations with MODIS FRP on a fire cluster and regional level. Similarly, (Li et al., 2020b) found a strong positive correlation between GOES16 and VIIRS FRP (VNP14) on a fire cluster and regional level across south-eastern USA. While the findings of these studies are significant, transferable conclusions are hard to be drawn as there is no consistency on the chosen spatial scales, study period lengths, fire regimes, land covers and climatic characteristics of each study area. This is especially true for the continent of Australia, which is underrepresented in similar studies but has a unique set of fire regimes that are very sensitive under climate change (Fairman et al., 2016).

Despite their spatial resolution limitations, GEO sensors provide a temporally dense FRP record that can assist in timely wildfire detection and provide detailed diurnal FRP information. A considerable amount of research (Ichoku and Ellison, 2014; Li et al., 2021; Mota and Wooster, 2018; Zheng et al., 2021) has been conducted using diurnal FRP profiles and temporal integrations of FRP to calculate the Fire Radiative Energy (FRE) and derive fuel consumption rates and biomass burning emissions, largely based on the works by (Ichoku and Kaufman, 2005; Wooster et al., 2005). Therefore, the use of GEO sensors and hotspot detection algorithms are becoming more critical, especially as the expected diurnal behaviour of wildfires shows increasing irregularities (e.g. high night-time intensities) caused by a changing climate and weather conditions (Balch et al., 2022; Freeborn et al., 2022). Meanwhile, inconsistencies in FRP peaking times across diverse African biomes (Mota and Wooster, 2018) and seasonal differences in agricultural fire peaking activity in China (Chen et al., 2022) indicate that LEO FRP might be insufficient for estimating a fire's diurnal cycle. Understanding the relative agreement between LEO and GEO derived estimates of FRP provides insights into how, when, and where the spatial and temporal trade-offs occur.

This study compares GEO derived FRP estimates using the new BRIGHT/AHI FRP product (Engel et al., 2022) against established LEO FRP estimations from MODIS (MOD14/MYD14) and VIIRS (VNP14IMG), on a continental scale for an entire year. The aim is to extend previous works focused on specific regions, seasons and magnitudes of wildfire events and examine different spatiotemporal scales of FRP comparison (Chatzopoulos-Vouzoglanis et al., 2022; Xu et al., 2017). Thus, FRP estimates from April 2019 to March 2020 across the whole of Australia are compared to identify the level of agreement between data sources across different seasons, land covers, and fire regimes.

3.2. Study area and data

3.2.1. Study area and period

The study was conducted across the continent of Australia from 1st of April 2019 to 31st of March 2020. It represents a year of observations across different fire regimes including extreme fire events as observed in south-eastern Australia (Fryirs et al., 2021). The study area was further segmented into 12 broad land cover classes provided by Geoscience Australia (Figure 3.2) (Lymburner et al., 2015). The land cover layer is based on a two-year (2014-2015) time-series dataset of MODIS vegetation indices and has a spatial resolution of 250m, which was resampled to match the spatial resolution of the examined datasets. The study area was also divided to north and south of the Topic of Capricorn (-23.5^{o} of latitude, which separates the northern tropics from the southern temperate zone) and east-west of the 140º of longitude using a data-driven approach based on hotspot density breaks visually identified (see Results – Figure 3.3). Finally, four local-scale case studies were chosen that represented the dominant land covers of the study area and showed significant fire activity across the examined datasets and are depicted in Figure 3.2.

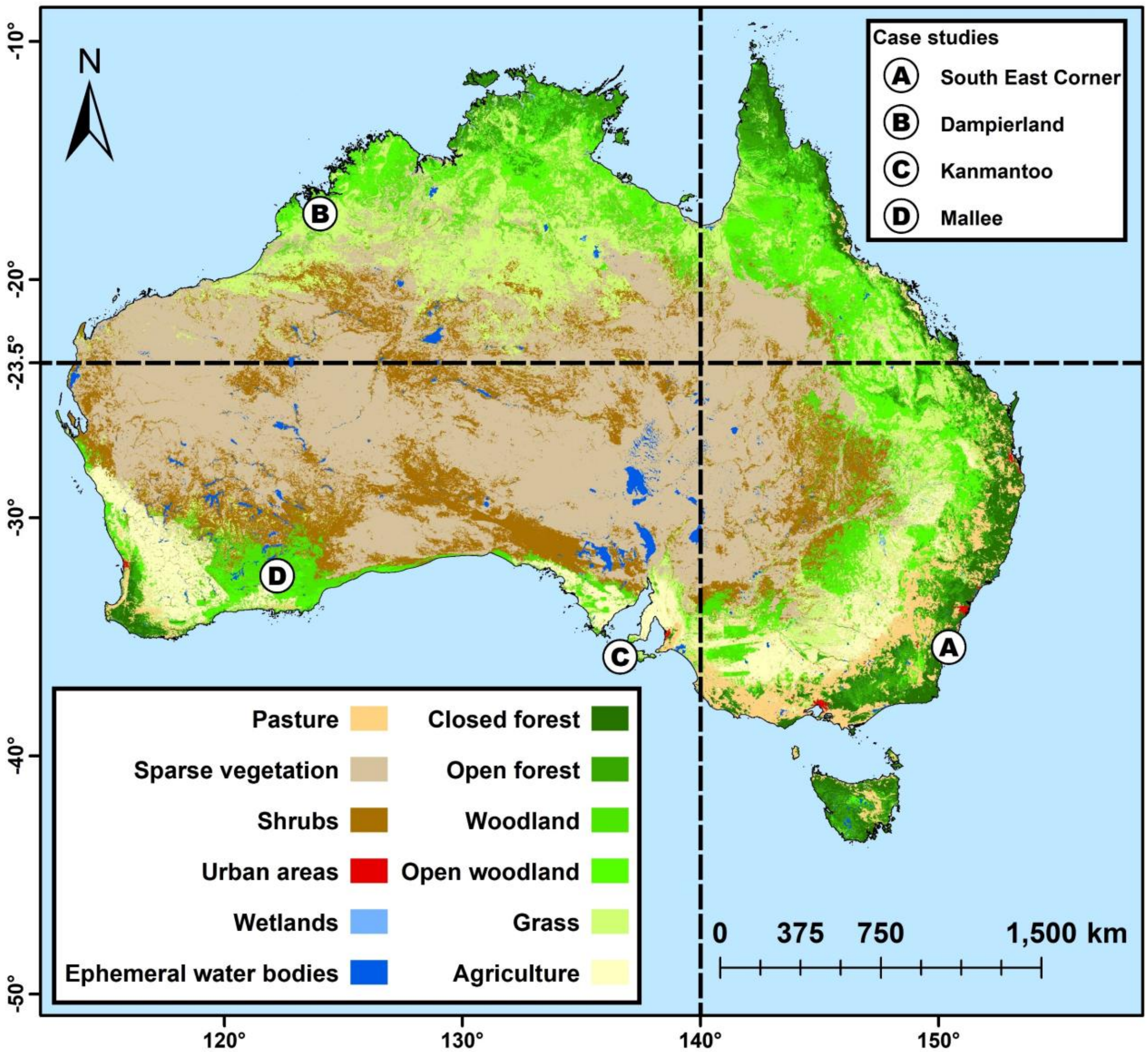

Figure 3.1 Land cover map of Australia used in this study. The land cover classes are generalisations based on the original classes presented in the dataset by (Lymburner et al., 2015). *The horizontal (east-west) dashed line corresponds to the Tropic of Capricorn at -23.5º latitude and the vertical (north-south) dashed line corresponds to 140º of longitude. These breaks define one of the major stratifications used in this study. The four labelled case studies represent different dominant land covers across the study area, have a significant number of hotspots across datasets and are explored in the methodology. The coordinate system used is WGS84.*

3.2.2. Hotspot Data acquisition and Pre-processing

The Advanced Himawari Imager (AHI) onboard the geostationary satellite ($140.7^{o}E$) Himawari-8 observes the full disk every 10 minutes, in 16 spectral channels and at spatial resolutions of 500m (channel 3), 1km (channels 1,2,4) and 2km (channels 5-16) at nadir (Bessho et al., 2016). The BRIGHT/AHI algorithm utilises imagery from AHI to detect wildfire hotspots across Australia (Engel et al., 2021a, 2021b), while hotspot FRP estimations are derived using the methodology suggested by (Wooster et al., 2003) (Engel et al., 2022). The FRP estimations used in this study were derived from Himawari-8 AHI data that were sourced from the Australian Bureau of Meteorology and processed using the methodology described in (Engel et al., 2022).

The polar-orbiting satellite hotspot datasets used for the intercomparison came from AQUA/TERRA MODIS and SNPP VIIRS. These include the MODIS Collection 6.1 MOD14/MYD14 FRP product at 1km spatial resolution (Giglio et al., 2021) and the VIIRS VNP14IMG FRP product at 375m (Schroeder and Giglio, 2018). The datasets were acquired using NASA's Level-1 and Atmosphere Archive and Distribution System (LAADS) (https://ladsweb.modaps.eosdis.nasa.gov/). Furthermore, both datasets implement the (Wooster et al., 2003) FRP estimation algorithm, enabling a more detailed direct comparison with BRIGHT/AHI.

MODIS hotspots with a scan angle greater than 30^{o} were excluded due to known errors in detection and FRP estimation quality (Freeborn et al., 2014b; Roberts et al., 2015), a common practise in the field (Engel et al., 2021b; Xu et al., 2017). However, no scan angle exclusion was implemented for VIIRS hotspots as no errors have been identified in the literature (Li et al., 2018a). Instead, VIIRS data were filtered using the fire detection confidence flag by excluding the low confidence hotspots, typically caused by sun glint, water presence and lower relative temperature anomaly (Schroeder and Giglio, 2018).

3.3.Methods

The selected datasets were first compared using varying sets of spatial and/or temporal fire hotspot aggregations to assess whether they were capturing similar fire behaviour trends. Then, the effect of each dataset's observation frequency was explored.

3.3.1. Exploring functional equivalence between datasets

3.3.1.1. Hotspot density and spatiotemporal progression

As a first step, the hotspot datasets were compared based on spatial distribution and density patterns for the whole year. First, the observed hotspots of each dataset were aggregated to a common 0.2^{o} regular grid over Australia. Then, the number of hotspots situated in each grid cell was normalised between 0-1. This way the plotted maps can be visually comparable and qualitative conclusions can be drawn about areas of similarity or discrepancy in hotspot density. From these data, spatiotemporal progression was visualised using time versus latitude/longitude graphs.

To examine temporal change across each coordinate and highlight spatiotemporal patterns in a two-dimensional manner, a new set of graphs were developed. The hotspots coordinates (longitude or latitude) were grouped in 1^{o} bins and then grouped by week. Finally, the data were plotted into a 2D colour mesh to create a spatiotemporal surface that indicates the temporal spread along one coordinate.

3.3.1.2. Hotspot matching and correlation

MODIS and VIIRS hotspots were resampled to the AHI grid following the methodology described in (Chatzopoulos-Vouzoglanis et al., 2022). This allowed for a one-to-one FRP observation comparison between the GEO and the polar-orbiting datasets and for correlation metrics to be computed. Resampling was implemented by either averaging (mean) or summing (total sum) spatiotemporal neighbouring LEO pixels to a BRIGHT/AHI pixel (i.e., using the superellipse spatial neighbourhood described in (Chatzopoulos-Vouzoglanis et al., 2022) with a time difference of <10 minutes). The summation resampling method corresponds to an accurate comparison in terms of energy exited per unit area alignment, although it does not account for sensor limitations associated with spatial resolution. As such, an averaging resampling method was implemented to examine the effect of sensor characteristics on the comparison.

As the distributions were heavily skewed, the datasets were log-transformed. A power-law model (linear in log-space) was selected and fitted to the original data as it more accurately described the relationship between the datasets. Furthermore, Pearson’s correlation coefficient was used to assess the linear association between the log-normalised data.

3.3.1.3. Regional comparison

The study area was split into four regions based on natural breaks and hotspot distributions observed and described in section 3.3.1.1. For each sub-region, the matched observations were plotted in violin plots per Land Cover (LC) to visually compare summary statistics and the distribution density of the FRP estimations. Averaged and cumulative aggregations of MODIS and VIIRS hotspots to the AHI grid were used to examine the impact of pixel size on the FRP magnitudes.

The data were log-transformed before plotting, so that the kernel-density estimation required for a violin plot would be computed on normally distributed data rather than the heavily skewed raw data. This way the values between the different intervals of 10^a ($a \in Z$) are uniformly spaced and the violin plots become easier to visualise and interpret.

3.3.2. Exploring temporal information differences

3.3.2.1. Diurnal FRP cycle based on spatial and temporal subsets

The average diurnal FRP cycles for different quadrants of the study area and period were computed to identify differences between the temporal coverage of each sensor. The data were filtered by location and period of interest (months of expected high and low fire activity), then grouped by local hour of the day, and their distributions were plotted as boxplots. Finally, the total number of hotspot detection per hour were also plotted as a measure of fire activity.

3.3.2.2. Small area FRP time-series comparison examples

The hotspots from each dataset were aggregated to the same 0.2^o grid (Section 3.3.1.1) and subsampled to hourly data by taking the maximum FRP observation in an hour. Then, four locations were chosen as representatives of all three EO datasets and the generalised LC classes (Section 3.3.1.3) on the basis of hotspot density numbers and aggregated FRP magnitude.

To explore broad time-series association, the dataset arrays were converted to equidistant hourly arrays for the period of available hotspots. Given the expected diurnal variability of FRP and following previous work on similar aggregations (Andela et al., 2015; Zheng et al., 2021), a Gaussian function was fitted to the LEO datasets while a rolling maximum window was applied to BRIGHT/AHI due to its higher observation frequency. This resulted in less noisy time-series that followed a 24-hour cycle and highlighted the higher observation frequency aspects of BRIGHT/AHI.

The continuous time-series were further used to derive Fire Radiative Energy (FRE) metrics for each case study, in order to provide a quantifiable comparison between the datasets. FRE is a temporal integration of FRP that can be used to derive burning biomass emissions (Ichoku and Ellison, 2014; Ichoku and Kaufman, 2005; Zheng et al., 2021) and combustion completeness metrics (Li et al., 2018b; Roberts et al., 2005). FRE was computed by evaluating the time integral of the continuous FRP measurements (Roberts et al., 2005; Wooster et al., 2005) for the duration of the event, as given in Eq 3.1:

$$FRE = \int_{t_0}^{t_n} FRP\, dt \qquad \text{Eq 3.1}$$

3.4. Results

3.4.1. Functional equivalence between hotspot datasets

3.4.1.1. Continental scale evaluation of hotspot density and spatiotemporal spread

The spatial distribution of the observed hotspots across the continent of Australia for each dataset is shown in Figure 3.2. The similarity between the maps indicates functional equivalence of fire activity as recorded across each of the three hotspot datasets. High density clusters appear in the south-east and north of Australia, while low density clusters are found in areas in the south-west and east of the continent. Upon closer examination some disagreement is also evident. This is most prevalent in the far north-east of the continent (Cape York, Far North Queensland) where VIIRS reports a lower density of hotspots compared to either BRIGHT/AHI and MODIS.

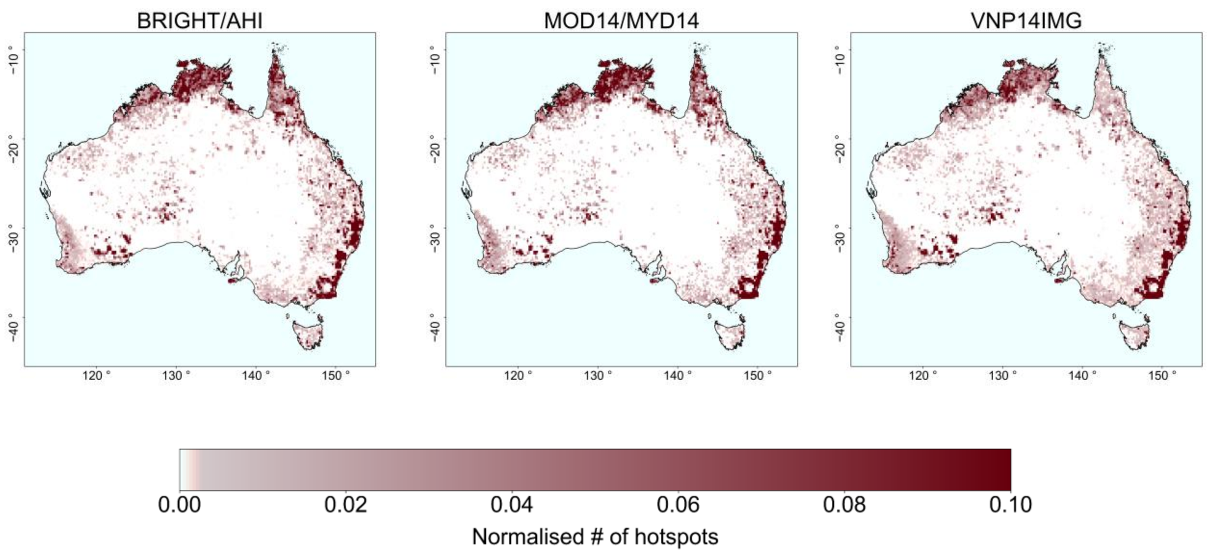

Figure 3.2 Fire activity for Australia between April 2019 and March 2020 as characterised by the normalised number of hotspots as identified by BRIGHT/AHI (left), MOD14/MYD14 (centre) and VNP14IMG (right).

Similarly, the spatiotemporal distribution patterns of hotspots (per week and rounded coordinate of longitude or latitude) appear almost equivalent for each of the hotspot datasets (Figure 3.4). All three datasets capture the long period of fire activity in northern Australia. Meanwhile, the beginning of the Black Summer Fires in September 2019 and its southerly progression is also captured by all three datasets, appearing as the most intense hotspot cluster (Figure 3.4 a, b, c). A similarly dense cluster is evident in the eastern-most part of the continent in the longitude-vs-time visualisations starting around the same period (Figure 3.4 d, e, f). The differences in the magnitude of the hotspot numbers between the datasets occur due to a combination of hotspot detection MIR threshold, spatial and temporal resolution.

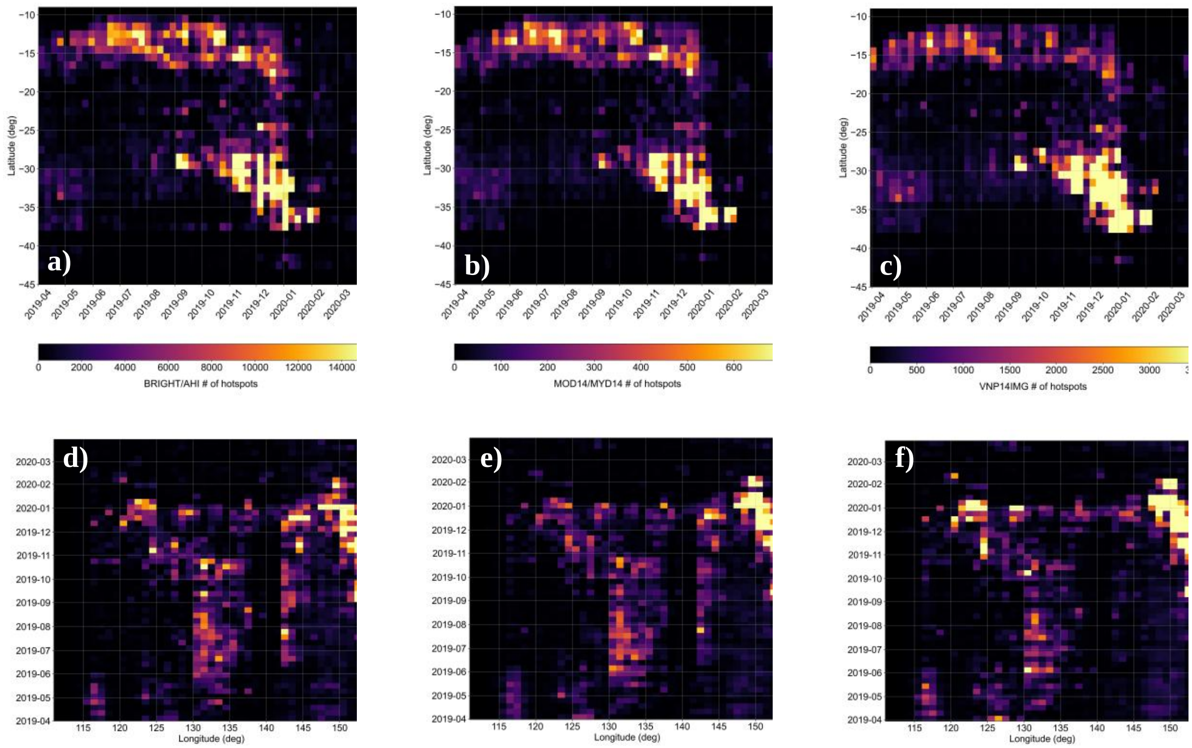

Figure 3.3 Spatial progression of hotspots shown through time (April 2019 to March 2020) in weekly intervals across all latitudes (top) and longitudes (bottom) for BRIGHT/AHI (a, d), MOD14/MYD14 (b, e) and VNP14IMG (d, f). The colour bars are adjusted to a specific range per dataset, for visual comparison of the patterns.

3.4.1.2. Hotspot matching and correlation

Hotspot-to-hotspot correlations between BRIGHT/AHI and the resampled LEO datasets are shown in Figure 3.4. The log-space linear relationship suggests that there is a power-law relationship between BRIGHT/AHI and the LEO datasets. The fitted power-law model in the original data shows that MODIS FRP is more similar to BRIGHT/AHI than to VIIRS FRP data. Meanwhile, the LEO datasets are strongly correlated with BRIGHT/AHI in log-space (Pearson's coefficients ranging from 0.74 to 0.77).

Figure 3.4 a) and b) demonstrate that BRIGHT/AHI overestimates the equivalent LEO hotspots (average FRP), especially when compared to VIIRS. However, for the summation resampling method (Figure 3.4 c), d)), VIIRS logs higher FRP for each BRIGHT/AHI pair, while MODIS underestimates very low BRIGHT/AHI observations (<25MW) and overestimates the >25MW observations. In addition, BRIGHT/AHI reaches a saturation value around 950MW creating a cut-off value in all four cases, something that is attributed to the known saturation of the MIR channel.

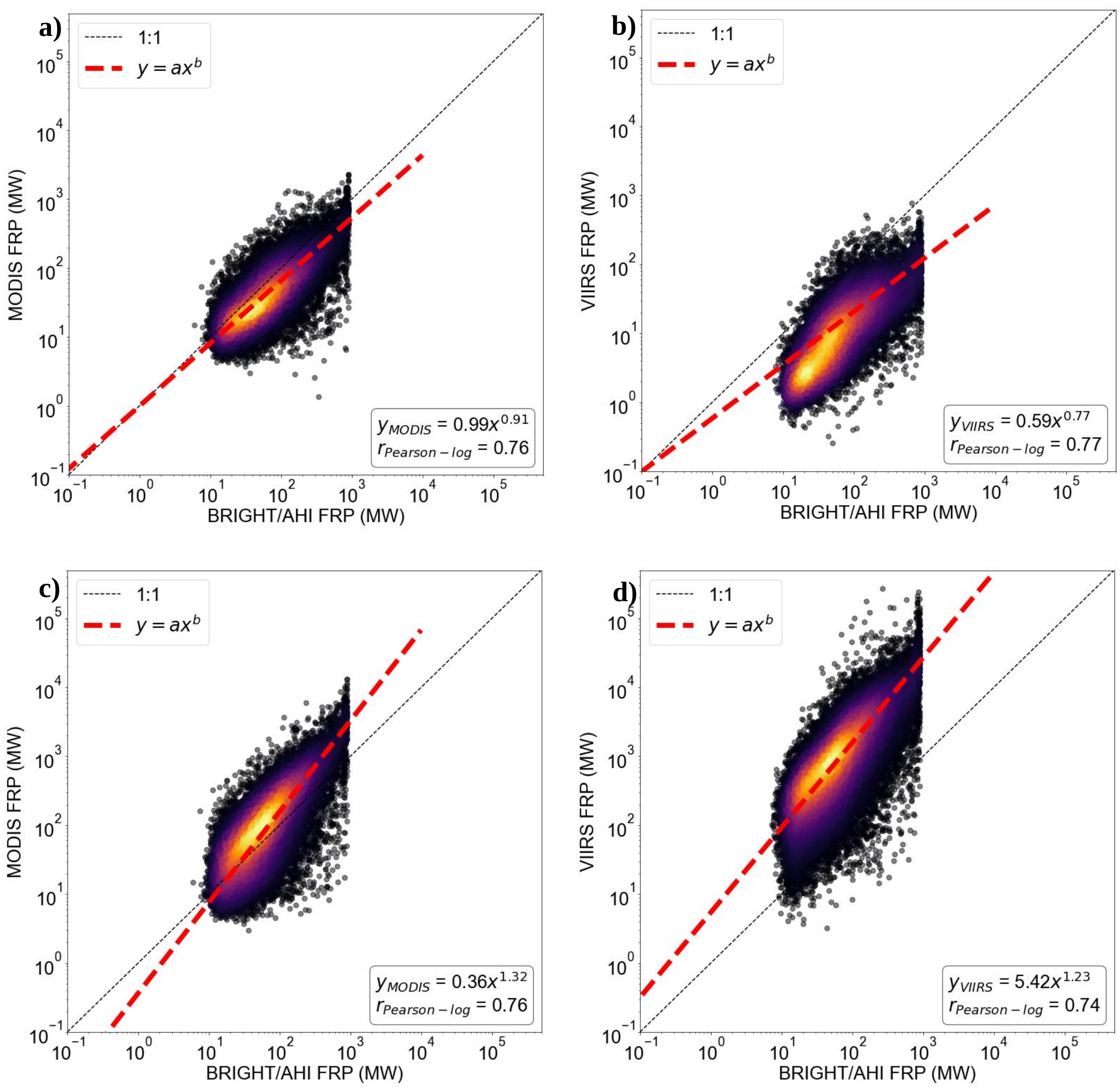

Figure 3.4 Scatterplots showing the matched BRIGHT/AHI hotspots with MODIS (a,c) and VIIRS (b,d) in Australia over the April 2019 to March 2020 period. The superellipse aggregation of the LEO data in the top row graphs (a, b) is implemented using the mean FRP of the spatiotemporal neighbours, while on the bottom row graphs (c, d) using the summation of each BRIGHT/AHI hotspot.

3.4.1.3. Regional and Landcover FRP distributions for matched hotspots

The violin plots in Figure 3.5 and Figure 3.7 summarize FRP estimation statistics and distributions across three broad vegetation classes. The LEO datasets systematically estimate a wider range of FRP values compared to BRIGHT/AHI, when resampled to the latter's grid using a summation aggregation. However, the FRP distribution relationships between datasets are inverted when LEO datasets are resampled using the averaging function instead.

The spatial resolution of the sensors has a notable impact on the FRP distributions throughout the study region, while the influence of vegetation type appears to be more regionally dependant (Figure 3.5). More specifically, the high-valued long-tailed FRP distributions reach a higher maximum with increasing spatial resolution (i.e., smaller IFOV). At the low-value end of the distributions MODIS reports the lowest minima. Meanwhile, vegetation type appears to mostly affect distributions in the southern regions, where the distribution densities are skewed towards the low-end in forests (compared to woodlands and grasslands), especially for BRIGHT/AHI. Finally, the truncation of the violin plots, particularly dominant in data for the south-west region, implies a saturation value for BRIGHT/AHI at approximately 950MW.

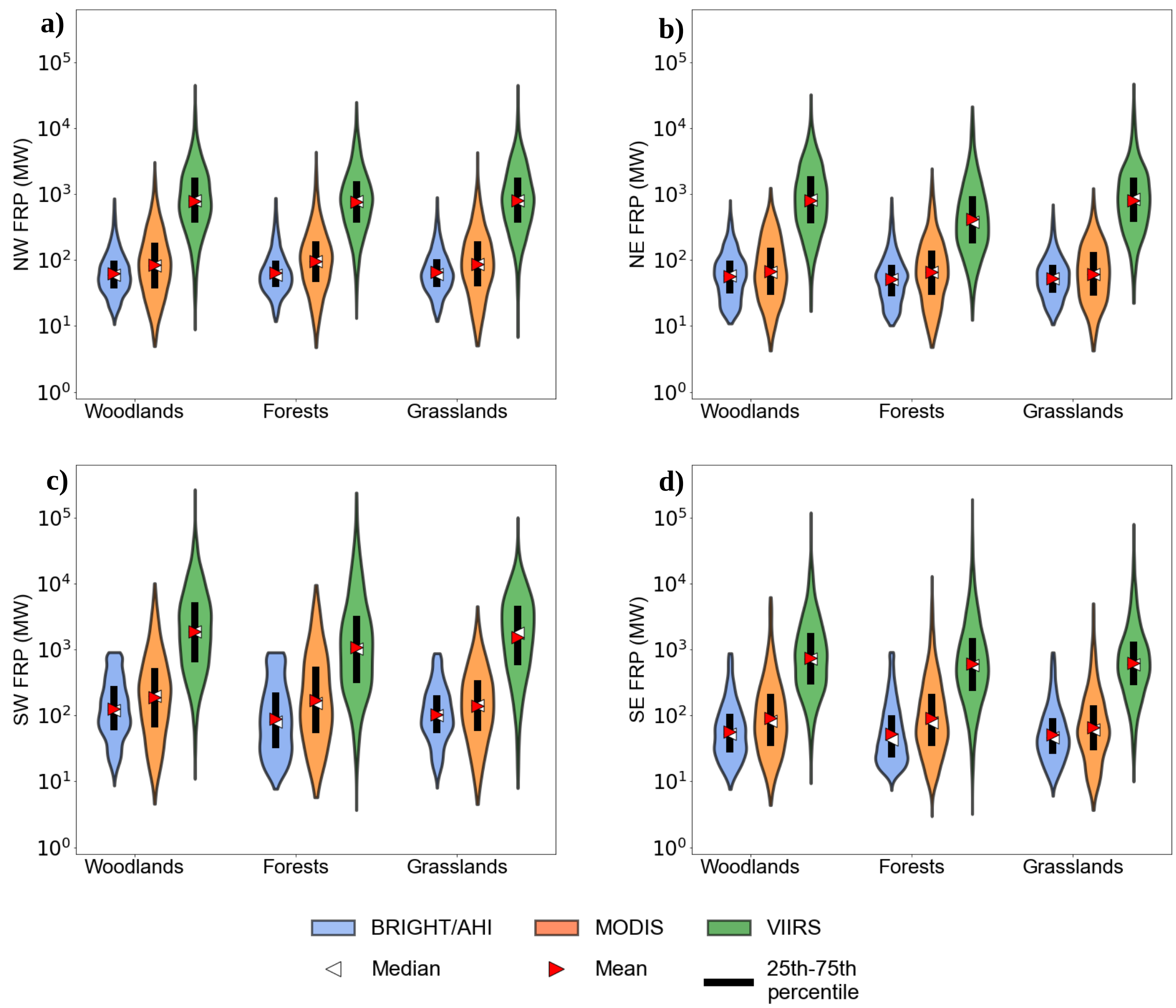

Figure 3.5 Distributions of FRP estimations for each vegetation class separated into each of the four quadrants as defined by the Tropic of Capricorn (top-bottom) and the 140º of longitude (left-right) over Australia and depicted in Figure 3.1. Where a) represents the northwest, b) represents the northeast, c) represents the southwest and d) represents the southeast sub-region. MODIS and VIIRS hotspots have been aggregated to show total FRP (sum) to match the coarser BRIGHT/AHI grid.

Figure 3.6 shows the violin plots for FRP per LC for all hotspot datasets, and where the LEO datasets are resampled to BRIGHT/AHI's grid using an averaging aggregation. BRIGHT/AHI shows overall higher FRP summary statistics compared to the LEO datasets, with FRP decreasing with increasing spatial resolution (i.e., smaller IFOV). Moreover, VIIRS FRP has a bi-modal distribution in the southern case study areas suggesting a larger accumulation of very low-intensity hotspots that have nevertheless been captured successfully by BRIGHT/AHI. Finally, on average more intense fires are being observed in the southern case study areas as compared to the northern case studies, this is as expected given the fuel loads associated with the landcovers.

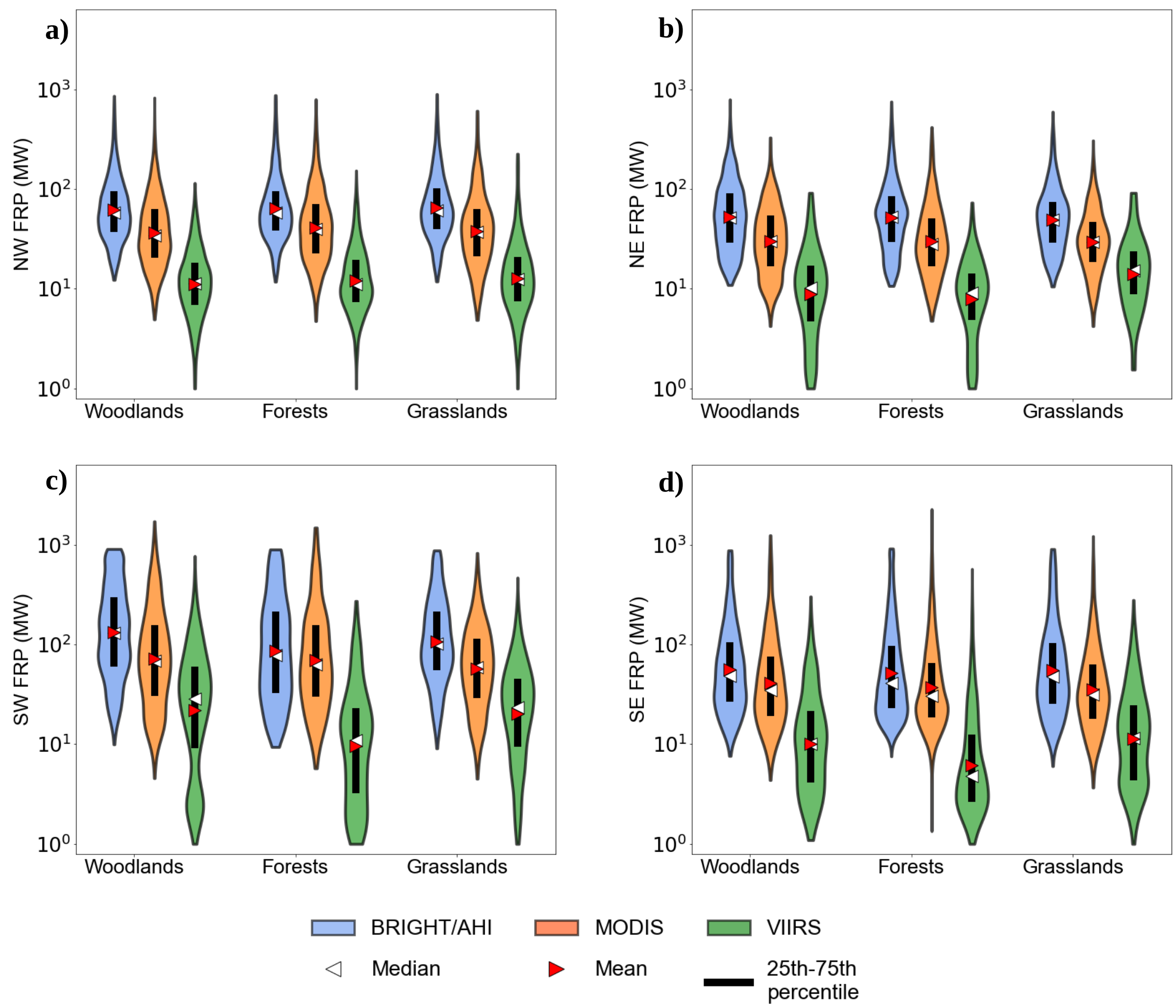

Figure 3.6 Distributions of FRP estimations for each vegetation class separated into each of the four quadrants as defined by the Tropic of Capricorn (top-bottom) and the 140º of longitude (left-right) over Australia and depicted in Figure 3.1. Where a) represents the northwest, b) represents the northeast, c) represents the southwest and d) represents the southeast sub-region. MODIS and VIIRS hotspots have been aggregated using the average FRP (mean) to match the coarser BRIGHT/AHI grid.

3.4.2. Independent dataset analysis and temporal insights

3.4.2.1. Diurnal FRP cycles

The average diurnal profiles of the FRP estimations for January 2020 and July 2019 (considered within high and low fire season for southern Australia, respectively) can be seen in Figure 3.7. Higher hotspot numbers and FRP summary statistics are reported for January compared to July across all hotspot datasets. However, BRIGHT/AHI offers a complete observation record across the whole day with clear peaks and troughs, and shows clear turning points of increasing and decreasing fire activity. More specifically, fire intensity is at its lowest range around 05:00 (local time) and then peaks around 15:00 during high fire season, a ten-hour difference. Meanwhile, fire intensity reaches its lowest FRP statistics around 07:00 and peaks around 13:00 during the low fire season. In contrast, the LEO datasets offer only a partial overview of FRP change per hour of day and miss certain aspects of diurnal fire activity such as the low activity in the early morning hours.

The same analysis north of the Tropic of Capricorn reveals a less obvious relationship between seasons for observed FRP, where fire intensity was marginally higher during January 2020 (Figure 3.8). However, BRIGHT/AHI and MODIS data observe higher fire activity in terms of the number of detected hotspots in July compared to January, something that is less pronounced in the VIIRS data. In the North, fire intensity peaks around 13:00 North regardless of season, while it reaches its minima during 06:00 in January and 07:00 in July. Once again, the LEO datasets do not have any observations during this time.

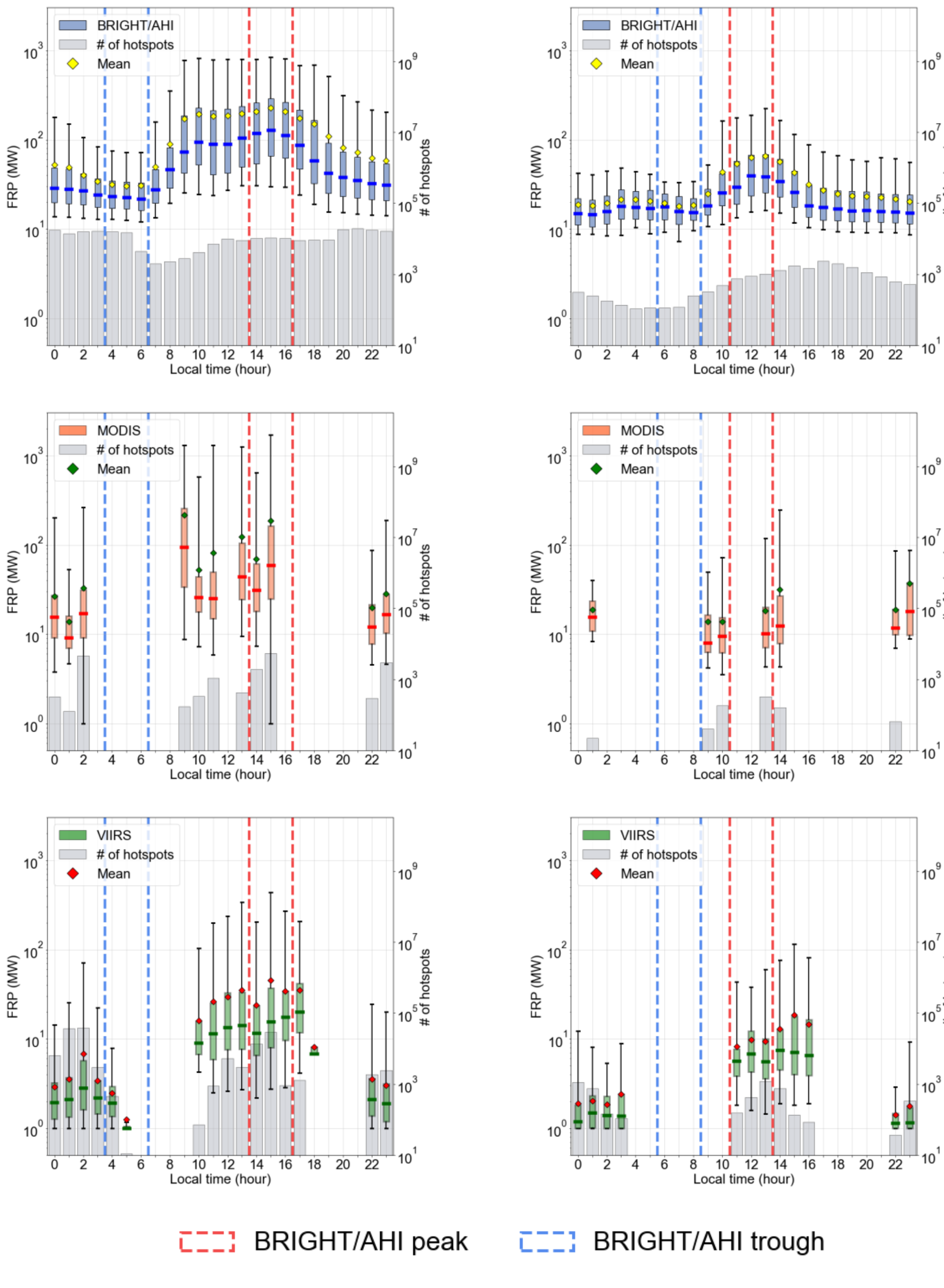

Figure 3.7 Box plots showing the diurnal FRP cycles for January 2020 (high fire season – left column) and July (low fire season-right column) in woodlands and forests across regions south of the Tropic of Capricorn. Each row corresponds to one of the examined hotspot datasets (BRIGHT/AHI top row, MODIS middle row, VIIRS bottom row). Number of observed hotspots is shown in grey. These hotspots correspond to the original independent observations captured by respective datasets. Red and blue dashed lines indicate peak and low activity in BRIGHT/AHI.

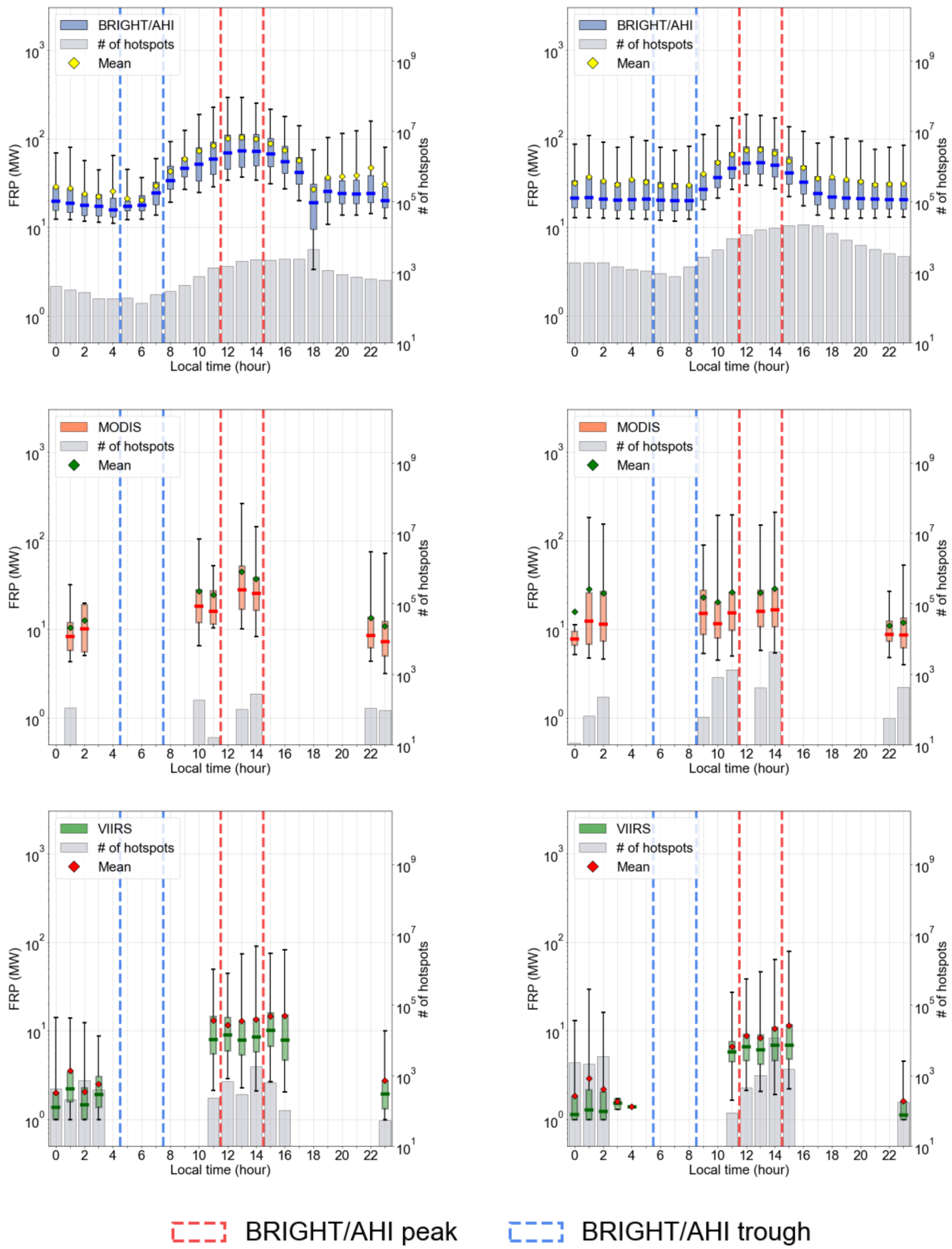

Figure 3.8 Box plots showing the diurnal FRP cycles for January 2020 (high fire season – left column) and July (low fire season-right column) in woodlands and forests across regions north of the Tropic of Capricorn. Each row corresponds to one of the examined hotspot datasets (BRIGHT/AHI top row, MODIS middle row, VIIRS bottom row). Number of observed hotspots is shown in grey. These hotspots correspond to the original independent observations captured by respective datasets. Red and blue dashed lines indicate peak and low activity in BRIGHT/AHI.

3.4.2.2. Small-area FRP time-series case studies

Four case studies across the continent as represented by individual 0.2^o grid cells were used to derive short and event-specific FRP time-series that spanned between four and eight days. Details on the locations regarding coordinates and dominant LC are reported in Table 3.1. FRE metrics show that MODIS significantly underestimates the first three events compared to the other two datasets, while it provides the highest FRE for the Black Summer Fires case study. Meanwhile, VIIRS consistently sits between BRIGHT and MODIS with its values being always closer to the former.

Table 3.1 Information for the small-scale case studies explored in this section. Each case study corresponds to a 0.2^o grid cell and the time series graphs can be seen in Figure 3.9.. The locations are depicted on the map of Figure 3.1.

Coordinates of grid point	**State**	**Bioregion name**	**Land Cover Class (mode)**	**Total FRE (GJ)**			**Duration**
				BRIGHT/AHI	**MODIS**	**VIIRS**	
Lon: 136.62 Lat: -35.84	South Australia	Kanmantoo	Forest (Open)	198.64	26.31	132.73	8 days
Lon: 124.02 Lat: -17.24	Western Australia	Dampierland	Grass	66.26	12.81	38.89	3 days
Lon: 122.22 Lat: -32.44	Western Australia	Mallee	Woodland	103.91	45.28	71.59	7 days
Lon: 150.42 Lat: -35.44	New South Wales	South East Corner	Forest (Closed)	145.92	183.25	151.86	4.5 days

Figure 3.9 shows the FRP time-series captured by the four fires examined in Table 3.1. Here, there is general agreement between BRIGHT/AHI and the diurnal FRP peaks captured by at least one LEO at a time, both in magnitude and local time. More specifically, BRIGHT/AHI agrees with VIIRS, whereas MODIS agrees with BRIGHT/AHI approximately half of the time.

On the coarser grid level, the datasets measure similar magnitudes of diurnal FRP, with the exception of the South East Corner case study, where the LEOs are in high agreement and estimate almost double the FRP values captured by BRIGHT/AHI. It is important to note that the time-series in Figure 3.9d) corresponds to a particularly intense megafire (Black Summer Fires), and MIR saturation can have a more significant impact on the FRP estimations.

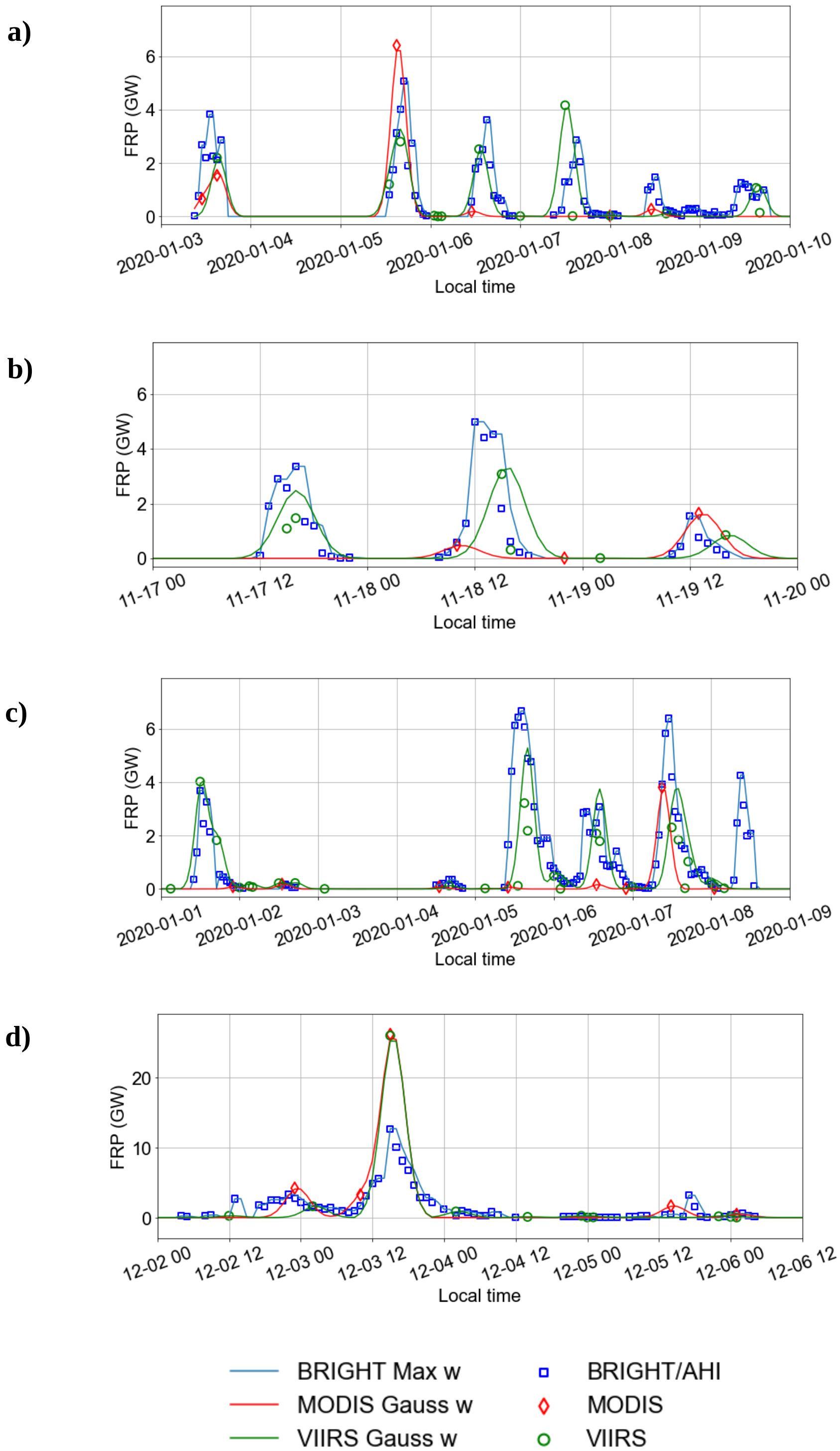

Figure 3.9 FRP time-series for four fire events (Table 3.1). Aggregated by summation FRP hotspots are plotted as single markers and connected with a fitted function. They correspond to 0.2o grid cells in a) Open forest in Kanmantoo (Kangaroo Island), b) Grasslands in Dampierland, c) Woodlands in Mallee and d) Closed forest in South East Corner (during the Black Summer Fires).

3.5. Discussion

With the increasing improvements and capabilities of GEO sensors for wildfire detection and monitoring, new observation opportunities are now available to better understand fire and its impact on the landscape and climate. Following previous work (Chatzopoulos-Vouzoglanis et al., 2022), this study reports on the equivalence and utility of the Himawari-8 BRIGHT/AHI hotspot product in comparison to commonly relied-upon LEO hotspot products. It does so on a continental scale by comparing fire intensity observations from LEO and GEO satellite sensors across different fire-prone land covers and fire seasons in Australia. Comparisons of continental wildfire density and spread patterns over a whole year and specific local fire events that span a few hours or days, allow us to assess the utility of BRIGHT/AHI data for each landcover.

At the continental scale, BRIGHT/AHI, MODIS and VIIRS FRP data were found to capture very similar spatiotemporal patterns of fire hotspot density and spread when using coarse spatiotemporal aggregations. However, pixel-level comparisons reveal differences due to spatial resolution variations and radiometric limitations of BRIGHT/AHI's 2km IFOV (e.g., MIR channel saturation). These are highlighted with the hotspot matching methodology (3.3.1.2), as multiple LEO pixels are aggregated and compared to a single BRIGHT/AHI pixel. Nevertheless, BRIGHT/AHI shows a strong positive correlation ($r = 0.76$) with the LEO-derived FRP for spatially and temporally matched hotspots.

When near-simultaneous FRP estimates on matched hotspots between the datasets are examined on a regional and land cover basis, BRIGHT/AHI captures similar FRP descriptive statistics to MODIS. In contrast, the higher spatial resolution and detection threshold of VIIRS result in a larger range of FRP values with different statistics, depending on the matching and aggregation methodology used (i.e., mean or summed aggregation). Overall, the results of the distribution analysis through the violin plots highlight the effect of spatial resolution on the FRP estimation which less evident for BRIGHT/AHI compared to MODIS but is more pronounced for BRIGHT/AHI compared to VIIRS. Nevertheless, other significant differences between the FRP estimate distributions are not easily identifiable, further increasing the confidence in the BRIGHT/AHI FRP estimates.

The comparison of diurnal FRP variability amongst AHI and LEO sensors shows that BRIGHT/AHI reveals considerably more detail. Regional diurnal trends with hotspot numbers and FRP ranges reveal insights about fire activity in a more complete manner when presented continuously by GEO sensors. The limited opportunities that LEO sensors have for fire observation makes such profiles hard to derive, especially when behaviour changes rapidly throughout the day (Balch et al., 2022). With the further launch, development, and continuation of GEO missions such as Himawari-8 and 9 (expected), diurnal cycle profiles could be established for different regions, land covers and seasons. It is hoped these enhanced diurnal profiles would lead to more timely active fire management, anomaly detection or long-term trend derivation, tools that can assist in better fire preparedness and suppression resources distribution and timings, as well as the quantification of the effects of a changing climate.

The examination of case study fires showed that, at a local scale and through the span of a few hours or days while an event is active, BRIGHT/AHI offers an almost continuous stream of fire information. Reconstructing the diurnal fire activity from these observations is quite straightforward. On the other hand, LEO sensors might have a single opportunity to detect the peak of fire activity throughout a day, which can be missed by the presence of clouds and/or smoke at the moment of overpass. For applications that require hourly (or timely) fire information, using LEO data will require certain assumptions to model the diurnal fluctuation, leading to higher uncertainties. Here, GEO observations can provide much more robust information.

The quantification of the uncertainties of the different products can provide more robust results when they are used in synergy for Fire Radiative Energy (FRE) calculation (Li et al., 2019a). Given the fire activity peaks that were missed by the different datasets analysed in this study, it can be inferred that substantial information needed for FRE calculation could be lost depending on the dataset of choice. For instance, MODIS FRE missed many FRE peaks and recorded significantly lower FRE than BRIGHT/AHI and VIIRS FRE for most 0.2^{o} grid cell case studies, resulting in an underestimation of the total FRE by a significant margin. The inconsistencies of MODIS FRP estimates can also be partially attributed to the different levels of uncertainty introduced by the scanning angle of a fire pixel (Freeborn et al., 2014b). Nonetheless, BRIGHT/AHI can saturate faster and underestimate the magnitude of FRP peaks in spatially small hotspot aggregations. When an extremely intense event was examined, FRE magnitude relationships of GEO and LEO were reversed, highlighting the LEO sensor’s advantages and the impact of BRIGHT/AHI’s MIR channel saturation. Nevertheless, these results correspond to events that were on high relative agreement between the datasets and may be harder to generalise.

In this study, at a local scale, BRIGHT/AHI tends to be in higher agreement with FRP fluctuations derived from VIIRS rather than with the established MODIS FRP product. This is quite interesting since (Li et al., 2020a) found that MODIS FRP estimations (MYD14) for wildfires across Africa are much lower than the respective VIIRS FRP estimations (VNP14IMG). The comparison that was implemented by (Li et al., 2020a) on varying spatial and temporal resolution aggregations reported up to 50% fire detection omissions by MODIS and a minimum of 42.8% lower FRP aggregations compared to simultaneous VIIRS estimations. These errors are attributed to MODIS not being as sensitive to lower intensity fires compared to VIIRS, as well as to pixel size increase towards the scan's edge (Li et al., 2018a), something that was accounted for in this study (see 3.2.2).

The results from the diurnal cycle modelling and the case study fires suggest that there are key periods of fire activity missed by LEO observations. These periods are significant because they can include rapid changes between low and high FRP, something that can be crucial for fire management. For example, the diurnal cycle graphs (e.g., Figure 3.7) show that LEO sensors have gaps in their records in the early morning and evening hours that correspond to rapid changes in fire intensity, due to fixed overpass times. The temporal continuity of GEO observations allows us to identify these periods of low and high fire activity without the need to make assumptions and regardless of geographical location and extent.

Our assessment is that BRIGHT/AHI FRP estimates are useful for characterising fire activity at a continental scale, across various land covers and seasons with a high observation frequency. Nevertheless, AHI's MIR channel saturation and its coarse spatial resolution tend to leave out low intensity fires and/or underestimate very high intensity ones, compared to the established LEO FRP datasets. With the imminent retirement of the TERRA/AQUA MODIS sensors, newer LEO sensors like VIIRS can still provide valuable information on fire activity, although more infrequently. Therefore, further validation of each dataset's omissions and drawbacks is needed, with possible multi-sensor fusion opportunities arising to take advantage of the different data streams.

3.6. Conclusions

In this paper, the BRIGHT/AHI FRP product was compared against the equivalent MODIS and VIIRS products. Despite its spatial resolution limitations, BRIGHT/AHI provides a good approximation of the MODIS and VIIRS FRP for simultaneously observed hotspots, while offering a much more detailed diurnal cycle of FRP due to its higher temporal resolution. The results suggest that newer geostationary products like BRIGHT/AHI can provide new information for fire monitoring that is lacking form Low-Earth orbiting sensors, especially when it comes to monitoring specific small-scale events through their rapidly changing life cycle. While this is not the first study to do such a comparison, it is the first do so on a continental scale. Hence, we argue that GEO sensors may be more suitable for fire monitoring beyond the timely detection stage and towards the fire severity and climate change direction. This new information should be used in conjunction with other data streams for better emission monitoring, fire preparedness and response, burn severity estimation and ecosystem recovery studies.

Chapter 4. Are fire intensity and burn severity associated? Advancing our understanding of FRP and NBR metrics from Himawari-8/9 and Sentinel-2

This chapter is based on: Chatzopoulos-Vouzoglanis, K., Reinke, K.J., Soto-Berelov, M., Jones, S.D., 2024. Are fire intensity and burn severity associated? Advancing our understanding of FRP and NBR metrics from Himawari-8/9 and Sentinel-2. International Journal of Applied Earth Observation and Geoinformation 127, 103673. https://doi.org/10.1016/j.jag.2024.103673

Abstract

Burn severity has been widely studied. Typical approaches use spectral differencing indices from remotely sensed data to extrapolate *in-situ* severity assessments. Next generation geostationary data offer near-continuous fire behaviour information, which has been used for fire detection and monitoring but remains underutilized for fire impact estimation. Here, we explore the association between remotely sensed fire intensity metrics and spectral differencing severity indices to understand whether and where they describe similar wildfire effects. The commonly used Differenced Normalised Burn Ratio (dNBR) severity index was calculated for Advanced Himawari Imager (AHI - 2km) and Sentinel-2 (20m) data and compared to different Fire Radiative Power (FRP) metrics derived from fire hotspot detections from AHI data across Australia. The comparison was implemented through different stratifications based on biogeographical region, land cover, fire type, and percentage of AHI pixel burned (fire fractional cover). The results indicate that FRP and dNBR metrics do not correlate in most scenarios, noting correlations being marginally stronger for hotter fires. However, correlations become significantly stronger when data are grouped using fire type information and fire fractional cover, with correlations peaking (r = 0.75) for large fires that burned 41-60% of an AHI pixel. In conclusion, remotely sensed fire intensity and severity proxies capture different aspects of wildfire impact, that only correlate with each other after using auxiliary data. Spectral differencing severity metrics have been used extensively during the past decades, however high-frequency fire intensity estimations have the potential to augment the existing information and reveal new ways of characterizing wildfire impact over large areas.

4.1. Introduction

Climate change and the projected worsening of fire weather are expected to increase the occurrence and severity of wildfires (Abatzoglou et al., 2019; Abram et al., 2021; Calheiros et al., 2021; Fairman et al., 2016). These events are important as they can cause rapid adverse changes to local environments with potential global effects (Fairman et al., 2022a). Remote sensing can offer information about vegetation condition over large spatial and temporal scales and it has been used to monitor wildfire impact and recovery dynamics (Gerrevink and Veraverbeke, 2021; Hislop et al., 2018).

Two important wildfire monitoring parameters used in remote sensing are related to the intensity and severity of a wildfire. Here, these two variables are described as the radiative power released by an active fire and the magnitude of spectral change that the burn caused, respectively. The Normalised Burn Ratio (NBR) is a spectral index that was developed for burned area and burn severity estimation (Key and Benson, 2006; López-García and Caselles, 1991). Field assessments of burn severity, such as the Composite Burn Index (CBI) (Key and Benson, 2006) and the Geometrically corrected version (GeoCBI) (De Santis and Chuvieco, 2009), are often used to establish an empirical relationship with NBR and extrapolate to larger areas for specific fire events and vegetation types. Differenced NBR (dNBR) values from pre- and post-fire scenes have been used to assess spectral change due to fire, as they demonstrate a strong correlation with GeoCBI compared to other spectral differenced indices (Gerrevink and Veraverbeke, 2021). However, pre-fire conditions, such as extremely low vegetation moisture can greatly influence the results of NBR-based burn severity indices, possibly deeming NBR unsuitable for use as a generalized burn severity metric (Gale and Cary, 2022). This is also the case in denser canopy forests, where spectral burn severity indices are more sensitive to top-of-canopy fire responses making it harder for NBR to be associated to different stratification of CBI and therefore harder to extrapolate (Fernández-Guisuraga et al., 2023a).

Bi-temporal spectral indices, such as dNBR, have become the tool of choice for assessing burn severity (Gale et al., 2022; Gibson et al., 2020). This results from a historical lack of continuously available satellite data that could capture other aspects associated with the rapidly evolving nature of wildfires (Keeley, 2009). For instance, fire intensity describes the energy released from burning biomass during a wildfire (Keeley, 2009), and it has been linked to direct effects on the fuel and ecosystems, such as biomass consumed by fire (Roberts et al., 2005; Wooster et al., 2005), and indirect effects on trees by heat exposure (Smith et al., 2016). Furthermore, brief exposure to low heat via radiation can affect the growth and survival of eucalypt tree species, subject to the bark moisture content (Subasinghe Achchige et al., 2022), as well as the net primary productivity of fire-resistant and mixed species (Sparks et al., 2018, 2017). Field burn severity classifications often fail to predict the mortality of trees that have been burned more recently, while remotely sensed spectral indices carry high uncertainties regarding tree mortality as well (Furniss et al., 2020; Volkova et al., 2022). Therefore, the estimation of only direct post-fire effects, such as dNBR, might be insufficient to quantify longer term tree survival and recovery (Sparks et al., 2016). Meanwhile, bi-temporal spaceborne LiDAR metrics examining forest recovery after wildfire do not show significant correlations with Landsat NBR and other spectral metrics, further stressing the need to complement severity studies with additional fire information (Huettermann et al., 2023).

Some remote sensors can estimate wildfire intensity by measuring the upwelling middle-infrared (MIR) radiation of a fire and converting it to Fire Radiative Power (FRP) (Wooster, 2002; Wooster et al., 2005, 2003). FRP and its time integration metric Fire Radiative Energy (FRE) are widely used for fire intensity monitoring and emission studies (Freeborn et al., 2014b; Ichoku and Ellison, 2014; Ichoku and Kaufman, 2005; Li et al., 2022; Nguyen et al., 2023). Despite the extensive literature on FRP/FRE studies regarding emissions and biomass consumption, the association between FRP and NBR metrics has only briefly been explored, with mostly non-significant associations being recorded (Henry et al., 2019; Heward et al., 2013). However, when data were aggregated to a coarser spatial resolution of ~0.5^{o}, MODIS FRE and NOAA/AVHRR dNBR showed significant correlations in Siberian forests (Ponomarev et al., 2023). Meanwhile, some studies are already using integrated FRP metrics from polar-orbiting sensors to describe severity (Sloan et al., 2022), with newer geostationary FRP products, such as the Biogeographical Region and Individual Geostationary HHMMSS Threshold (BRIGHT) (Engel et al., 2021a), enabling enhanced monitoring and estimation of FRP/FRE (Chatzopoulos-Vouzoglanis et al., 2023, 2022).

Fuel structure is also an important consideration when studying wildfire and its effects from space. Dense canopy cover can obstruct the line-of-sight of the sensor and lead to fire intensity underestimation or even a late detection (Johnston et al., 2018). The need to account for this complexity was shown by Roberts et al. (2018) where ancillary variables such as the Leaf Area Index (LAI) and tree cover percentage were used to make adjustments to improve intensity estimations. Changes in the total fuel load due to fire, captured by airborne LiDAR, have also been found to be linearly correlated to MODIS FRE, with even stronger correlations observed through the addition of canopy obstruction information and more frequent fire intensity observations (McCarley et al., 2020). Recent studies (Sparks et al., 2023a) provide further argument for the use of ancillary data, showing that the rate of spread and maximum FRP of small area fires is correlated to the rate of tree height growth. Each of these studies reveal opportunities for estimating fire impact across larger spatial areas via the use of additional variables. When coupled with an increasing frequency of observations of fire activity through geostationary satellites and constellations, there may be further improvements to these estimates.

As near-continuous active fire intensity information is becoming available from next-generation geostationary sensors, we have new opportunities to understand wildfires and their impacts. However, the association between wildfire intensity and burn severity is not well-understood nor documented. In this study we provide the first comprehensive investigation into the association of fire intensity measures with widely used remote sensing observations of burn severity. We define fire intensity as FRP and FRE and burn severity as NBR and dNBR. We explore the association between fire intensity metrics and spectral-differencing severity indices according to biogeographical region, vegetation type, land cover, fire type, and fire fractional cover. We test the following assumptions:

1) A strong positive correlation exists between fire intensity and burn severity,
2) Correlations increase as the fire fractional cover area increases,
3) Correlations are stronger for higher intensity fires,
4) Correlations are stronger when the height of the burned vegetation is low, canopy cover is sparse and fire observations are not obstructed by the canopy.

To test these assumptions, we compare geostationary (Himawari-8) and polar-orbiting (Sentinel-2) dNBR information with geostationary products of FRP (Engel et al., 2022) across the whole of Australia (~7500 wildfire hotspots) over a 12 month period (April 2019 and March 2020). We stratify the study area according to regional biophysical characteristics, land cover, fire type, and AHI pixel fire fractional cover -in order to investigate the relationship between fire intensity and severity as observed via satellites and help reveal underlying factors that drive these associations.

4.2.Methods

4.2.1. Study area and stratification

Australia was chosen as the study area as it includes a variety of land covers, vegetation types and fire regimes. Following previous work, data from April 2019 to March 2020 were used to account for seasonal variability across the continent (Chatzopoulos-Vouzoglanis et al., 2023). The study area was stratified using biogeographically homogenous regions (bioregions), defined as the Interim Biogeographic Regionalization for Australia (IBRA) (DAWE, 2000). In addition, the Australia’s State of the Forests Report (SOFR, 2018) was used to stratify the analysis based on canopy cover and density in forested areas (Table 4.1), as well as land cover information from Lymburner et al. (2015). Auxiliary raster data were resampled to a 2km resolution to be comparable to Himawari data.

Table 4.1 Description of datasets used to spatially stratify the study area.

Stratification dataset	Description	Reference
Interim Biogeographic Regionalization for Australia (IBRA)	A regionalization framework based on continental and regional climate information, ecological data, geology, and geomorphology.	(DAWE, 2000)
Australia's State of the Forests Report	The report includes a variety of forest variables (e.g., canopy cover and density, canopy height, tree species). It is derived from data captured between 2011 and 2016.	(SOFR, 2018)
Geoscience Australia Land cover	Land cover information derived by MODIS data for 2015.	(Lymburner et al., 2015)

4.2.2. Wildfire hotspot selection and fire intensity

Wildfire detections from Advanced Himawari Imager data that were processed using the BRIGHT algorithm (BRIGHT/AHI) and their associated FRP metrics were chosen for the study area and period (Chatzopoulos-Vouzoglanis et al., 2023; Engel et al., 2022, 2021a, 2021b). The dataset consists of ~170,000 hotspot locations (~2kmx2km pixels), 30,000 of which were randomly selected to manage data storage and processing restrictions. The 30,000 hotspots were cross-referenced using VIIRS hotspots (VNP14IMG) (Schroeder and Giglio, 2018) as a quality measure, resulting in ~7,500 high confidence BRIGHT/AHI hotspots. The time-series of FRP observations for each hotspot was used to derive additional metrics. The peak wildfire intensity was described by the Maximum FRP (MaxFRP) of the time-series, while FRE was calculated to describe the total (integrated) energy emitted by one hotspot. FRE was calculated on a 10-minute interval (FRE_{10}) using the following model:

$$FRE_{10} = \int_{t_0}^{t_n} FRP_t \, dt$$

4.2.3. AHI burn severity index

For the examined BRIGHT/AHI hotspot locations, full-disk reflectance data for NIR and SWIR channels from AHI (Bessho et al., 2016) were downloaded from Australia's National Computational Infrastructure (NCI) (https://nci.org.au). The pre- and post-fire conditions were defined by taking the median spectral value of each pixel in the seven days before the first detection and after the last detection, respectively. In the absence of a cloud mask for AHI during the study period, this was deemed an effective way to exclude clouds and other outliers. Finally, the pre- and post-fire NBR values were used to compute the dNBR (Key and Benson, 2006).

4.2.4. K-Means clustering used for determining fire type

The 7,500 BRIGHT/AHI hotspot locations were classified into four clusters using the K-Means clustering algorithm implementation in the Python programming language (Pedregosa et al., 2011). The variables used as inputs for the clustering included the MaxFRP for each location, the FRE_{10}, the duration of the fire in days (Persistence), and the dNBR information from the AHI data (4.2.3).

The probability density function of each of the four variables (MaxFRP, Persistence, dNBR, and FRE_{10}) was plotted to inspect their statistics and modality for each vegetation type (canopy height and density). After visual inspection of the distributions and the K-Means clustering result, the maximum separation was achieved on the MaxFRP and Persistence of the fires axes. These four clusters were then given a qualitative label by interpreting their value ranges over the two axes (hot and cool, long and short). This stratification was used to examine how the dNBR and FRP association fluctuates between fire types. The different fire type hotspots were also plotted on a map to examine their spatial distribution and density.

4.2.5. Sentinel-2 burn severity and fire fractional cover analysis

4.2.5.1. Sentinel-2 dNBR

Sentinel-2A and 2B data were acquired using the Geosciences Australia infrastructure (Krause et al., 2021), to increase the confidence in the dNBR metrics and extract the burned area within the BRIGHT/AHI pixel extent. For each fire type, ~400 random samples were selected (4.2.4) ensuring that each land cover would be represented with at least 30 hotspot locations, when available. This resulted in ~1700 locations, for which Sentinel-2 SWIR (Band 12) and NIR (band 8A) data were downloaded.

The pre- and post-fire periods were defined for each hotspot individually, by examining the first and last BRIGHT/AHI hotspot detection time and allowing a 30-day period buffer before and after the fire, respectively, to account for data scarcity. To achieve an acceptable tradeoff between data quality and completeness, Sentinel-2 scenes with at least 90% cloud-free conditions were chosen. Finally, data gaps and outliers were filtered out using the median of each pixel's time-series within the period of interest. Sentinel-2 dNBR was calculated as the average dNBR of all the pixels situated within a single AHI pixel.

4.2.5.2. Sentinel-2 fire fractional cover

The fire fractional cover (FFC) for each of the ~1700 BRIGHT/AHI pixels was calculated using the higher resolution dNBR from Sentinel-2. The burned and unburned areas within the BRIGHT/AHI pixels were separated using dNBR thresholds specific to each fire type (4.2.4). These thresholds were calculated using binary K-Means clustering on the Sentinel-2 dNBR values (20m pixels) within each BRIGHT/AHI hotspot (2km pixel). Subsequently, the minimum dNBR values for each burned area cluster were grouped by fire type. Finally, the average of the minimum dNBR values for each fire type was used as a threshold. The burned area percentage was calculated using the ratio of burned area estimations and the total area of the AHI pixel to represent the FFC.

4.2.6. Statistical analysis between intensity and severity metrics

Pearson's correlation coefficient (R) was used to assess the linear association between variables in each stratification (bioregion, fire type, FFC, land cover). For each grouping, Pearson's R was calculated between dNBR and FRE_{10} or MaxFRP pairs, where each pair corresponded to the extent of individual AHI pixels and the duration of the fire within each pixel. As the relationship between FRE_{10} and dNBR is not linear, FRE_{10} was log-transformed (Chatzopoulos-Vouzoglanis et al., 2023). The same metric was used for all other stratifications. Only significant correlations with a p-value smaller than 0.05 and a sample population (n) of at least 25 are used, while where possible correlations were calculated and compared for equally sized populations to reduce bias.

4.3. Results

4.3.1. Continental scale comparison of intensity and severity

Figure 4.1 shows correlation between dNBR and FRE_{10} or MaxFRP in the bioregions that had over 25 hotspots (40 out of 89 bioregions). FRE_{10} correlates to dNBR moderately or strongly more often than MaxFRP, in 7 out of 40 compared to 2 out of 40 bioregions respectively. Central Mackay Coast in the northeast demonstrates the highest correlation of r = 0.78 (p = 0.00) between both FRP metrics and dNBR.

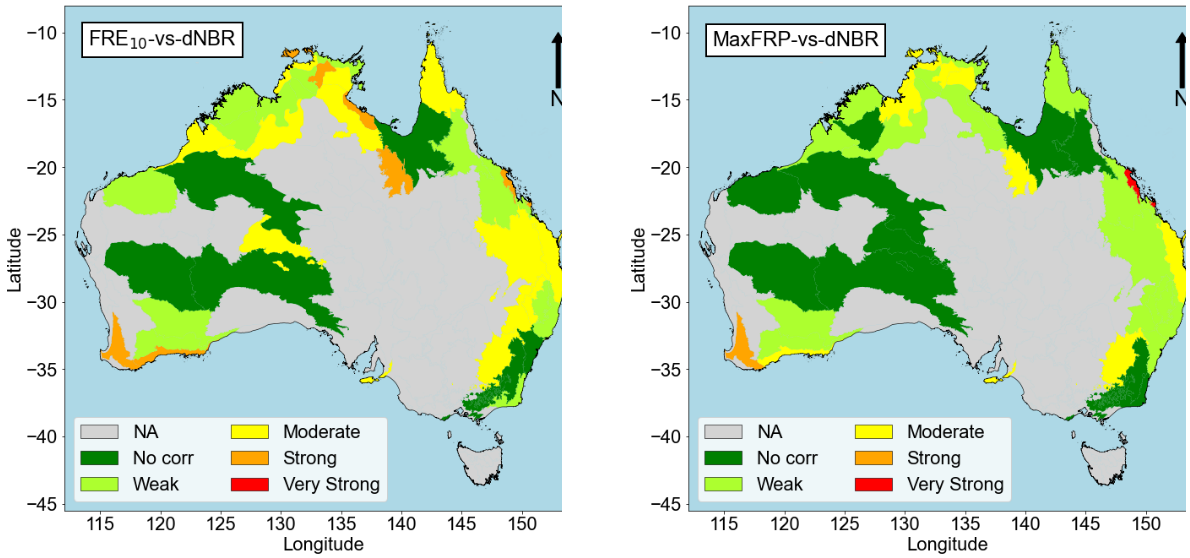

Figure 4.1 Correlation between dNBR and FRE_{10} (left) or MaxFRP (right) for the BRIGHT/AHI hotspots within each bioregion, where sample size is significant (n>=25). Very strong correlation corresponds to r>0.8, Strong to 0.6>r>0.8, Moderate to 0.4>r>0.6, Weak to 0.2>r>0.4 and No correlation to r<0.2.

Table 4.2 shows information about the bioregions where FRE_{10} and dNBR demonstrated a strong or very strong correlation as well as showing the dominant land cover and fire persistence. The most common land cover at hotspot locations is closed forest and woodland, while most of the fires burned for one to three days with highly variable FRE_{10}. When MaxFRP and dNBR correlations are examined however (Table 4.3), their correlation is strong and very strong only in two bioregions, both represented by mostly closed forest fires with high MaxFRP and Persistence.

Table 4.2 FRE_{10}-vs-dNBR statistics per bioregion where the correlation is strong or very strong (Figure 4.1). Only bioregions with n>=25 and a r>= 0.6 are included.

Bioregion	**r**	**P**	**Count**	**Dominant land cover**	**Persistence (days)**	**FRE_{10} (MJ)**
Central Mackay Coast	0.78	0.00	38	Closed forest	2.8	16088
Tiwi Cobourg	0.78	0.00	39	Closed forest	3.1	6733
Esperance Plains	0.74	0.00	51	Open forest	1.2	22974
Arnhem Plateau	0.66	0.00	117	Woodland	1.4	5802
Mount Isa Inlier	0.65	0.00	58	Sparse vegetation	1.1	6706
Gulf Coastal	0.64	0.00	118	Woodland	1.7	6889
Jarrah Forest	0.63	0.00	79	Closed forest	2.1	18956

Table 4.3 MaxFRP-vs-dNBR statistics per bioregion where the correlation is strong or very strong (Figure 4.1). Only bioregions with n>=25 and a r>= 0.6 are included.

Bioregion	r	P	Count	Dominant land cover	Persistence (days)	MaxFRP (MW)
Central Mackay Coast	0.83	0.00	38	Closed forest	2.8	674
Jarrah Forest	0.66	0.00	79	Closed forest	2.1	893

4.3.2. Density of hotspots according to vegetation height and canopy cover

Figure 4.2 shows the probability density functions of the BRIGHT/AHI hotspots classified by vegetation height. The distribution of dNBR values does not change significantly between categories, although progressively lower values of dNBR are observed as the vegetation height increases in forests. In contrast, the observation of persistence of fires along with their FRE_{10} increase with increasing vegetation height. The distribution of MaxFRP appears to be bimodal while the remaining variables present unimodal distributions.

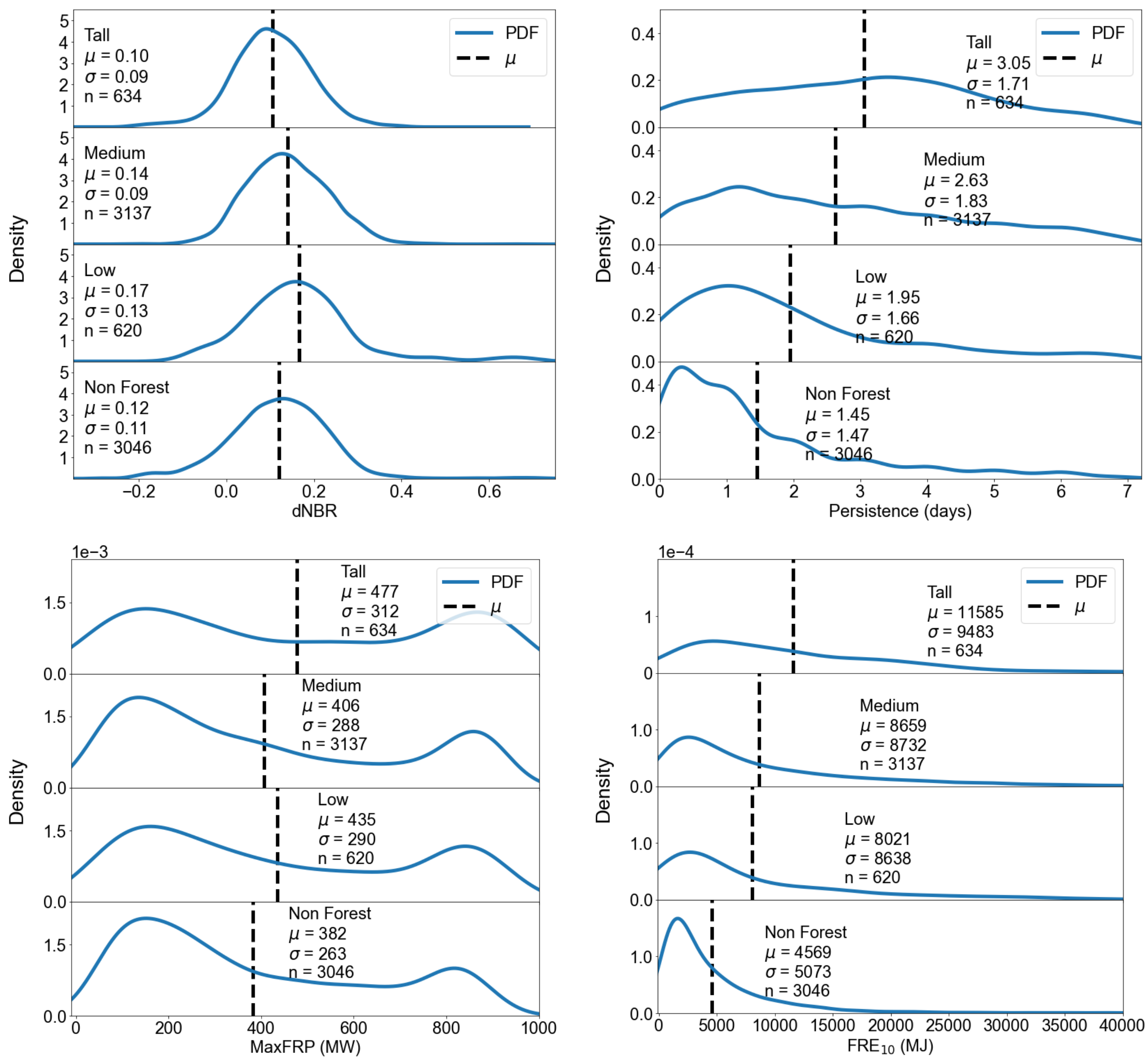

Figure 4.2 Probability Density Functions (PDF) of the BRIGHT/AHI hotspots classified according to the vegetation height. Tall class corresponds to >30m canopy height, Medium to 10-30m, Low to 2-10m and Non-forest to lower vegetation (SOFR, 2018). The variables dNBR, Persistence, MaxFRP and FRE_{10} are derived from AHI and BRIGHT data for individual and continuous wildfires that occupy a single AHI pixel.

Similarly, Figure 4.3 depicts the probability density functions of the BRIGHT/AHI hotspots classified by forest canopy cover. Once again, dNBR does not show significant differences between categories, while observed fire persistence increases with increasing canopy cover. MaxFRP and FRE_{10} also seem to increase with canopy density, although closed canopies that account for a small percentage of the hotspot population show lower statistics.

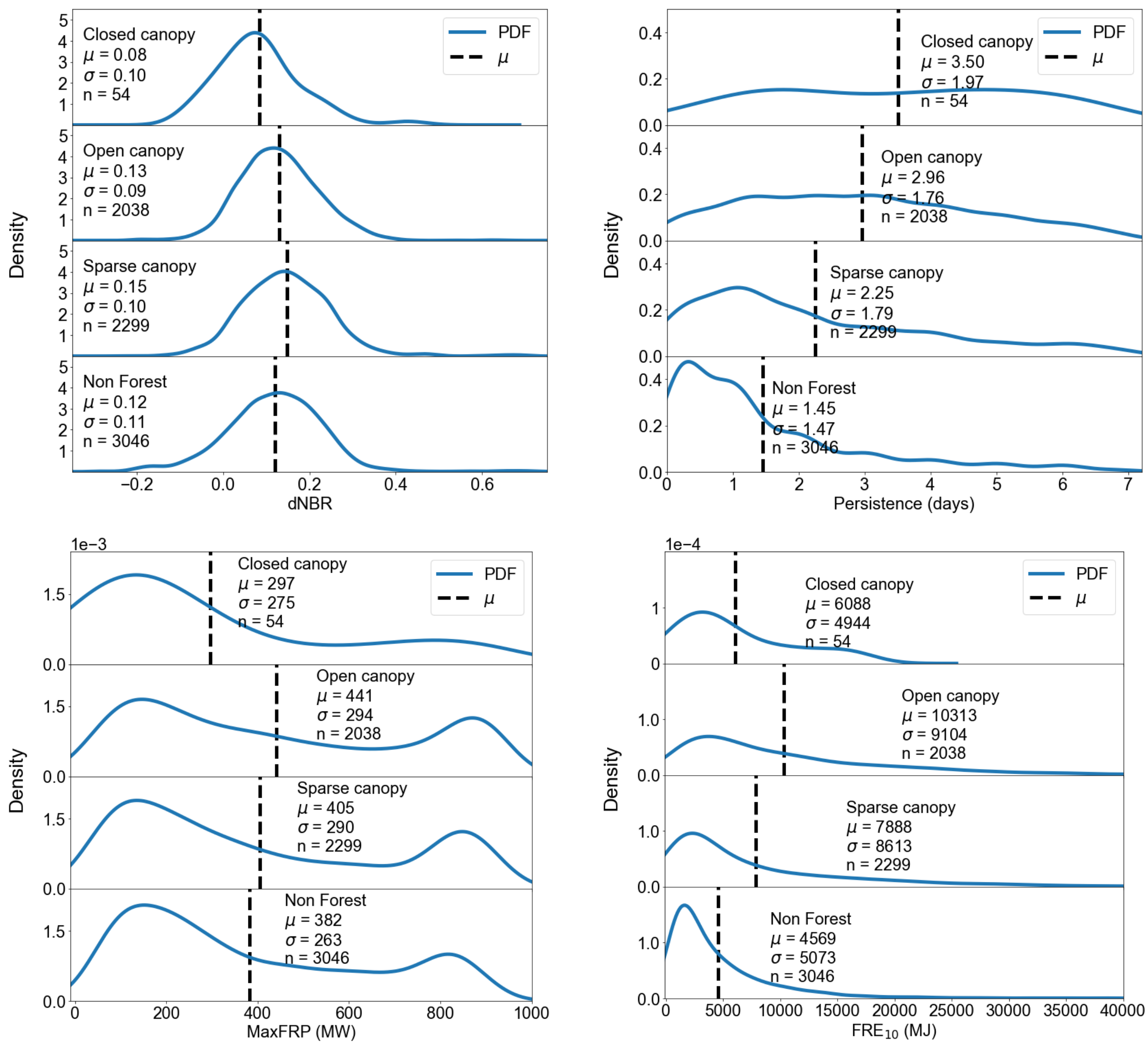

Figure 4.3 Probability Density Functions (PDF) of the BRIGHT/AHI hotspots classified according to the vegetation canopy cover. Closed canopy class corresponds to >80% forest crown cover, Open canopy to 50-80%, Sparse canopy (Woodlands) to 20-50% and Non-forest to <20% (SOFR, 2018). The variables dNBR, Persistence, MaxFRP and FRE_{10} are derived from AHI and BRIGHT data for individual and continuous wildfires that occupy a single AHI pixel.

4.3.3. K-Means clustering of fire types

The ~7500 VIIRS-validated BRIGHT/AHI hotspots were classified into four clusters using K-Means clustering and the variables dNBR, MaxFRP, FRE_{10}, and Persistence. The optimal visualization of the clusters in two dimensions where the maximum separation is achieved was defined using MaxFRP and Persistence (Figure 4.4) and their individual statistics can be seen in Table 4.4. Here, fires that burn for less than three days are classified as "short", while the ones that burn for four days on average are classified as "long". Similarly, fires that peaked at around 740MW are classified as "hot", with "cool" fires peaking at 220MW on average.

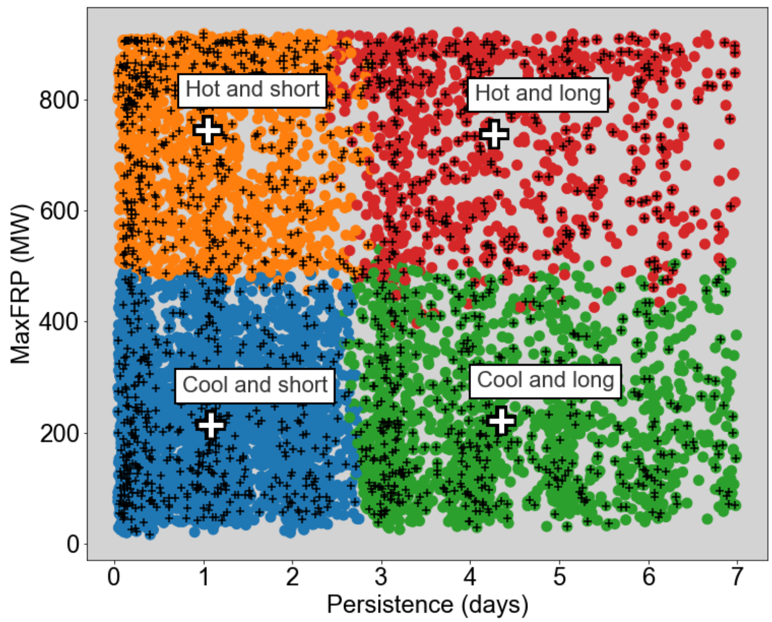

Figure 4.4 K-Means clustering applied to the dataset (n=~7500) and labelled to different fire types. White crosses represent the centroid of each cluster. Black crosses (n=~1700) represent the randomly sampled hotspots for later analysis that was conducted with coincident Sentinel-2 data.

Table 4.4 Mean cluster values (centroids) derived by K-Means. A qualitative description is added to make clusters easier to interpret.

Cluster	FRE_{10} (MJ)	Max FRP (MW)	dNBR	Dt (days)	σ_{dNBR}
Hot-and-short	10846.56	745.51	0.16	1.05	0.13
Hot-and-long	18874.15	738.35	0.15	4.26	0.12
Cool-and-long	5466.24	222.05	0.12	4.35	0.09
Cool-and-short	2742.16	213.77	0.12	1.08	0.09

Figure 4.5 shows the spatial distribution, kernel density and population of the different fire types over Australia. During the study period, hot fires occurred with a higher frequency in the south while most hot-and-long fires were observed in the southeast (Black Summer Fires). Cool-and-short fires are the most common across the continent, but they are particularly dense in the north. Hot-and-short, and cool-and-long fires have similar populations, while hot-and-long fires are the least frequent fires.

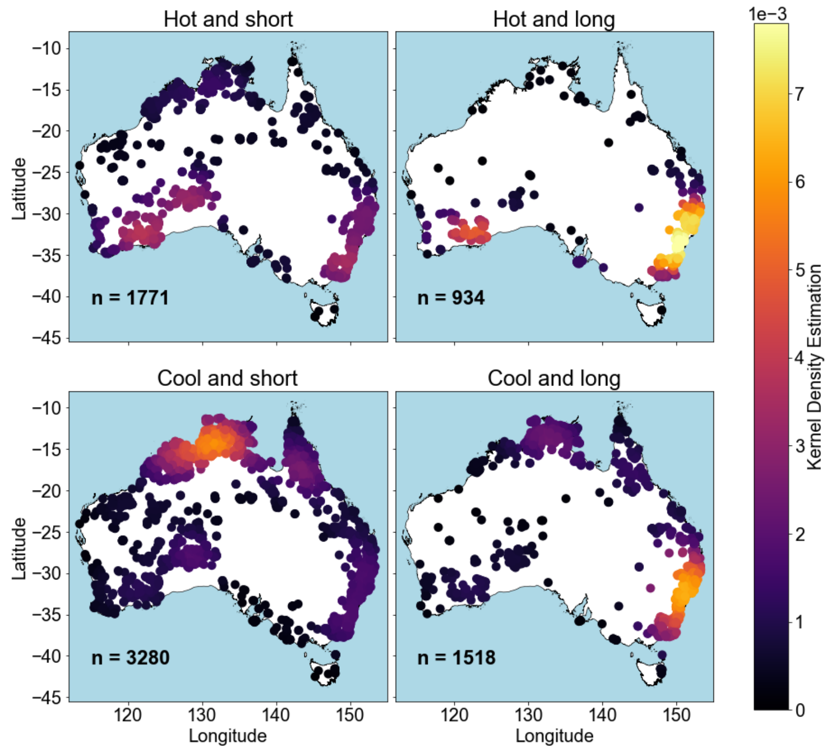

Figure 4.5 Spatial distribution and density of fire types over Australia. Fire types are derived using K-Means to cluster the dataset based on MaxFRP, FRE_{10}, Persistence and dNBR.

4.3.4. Sentinel-2 burn severity index and fire fractional cover analysis

The FRP and the Sentinel-2 Fire Fractional Cover (FFC) association varies depending on the fire type and is shown in Figure 1.1.1. Although FFC between fire types does not change significantly, there is a notable trend for hot-and-short fires where two groups are evident consisting of very low or very high FFC. Here, one group demonstrates high MaxFRP and seems to burn over 80% of the AHI pixels, while the second group of hotspots corresponds to a 20% FFC or less. Cool-and-short fires do not show any significant patterns, burning variable portions of the pixels. Finally, the correlation between FFC and MaxFRP is significant (r = 0.35-36) only in the case of hot fires. Results for FRE_{10} show a similar behaviour.

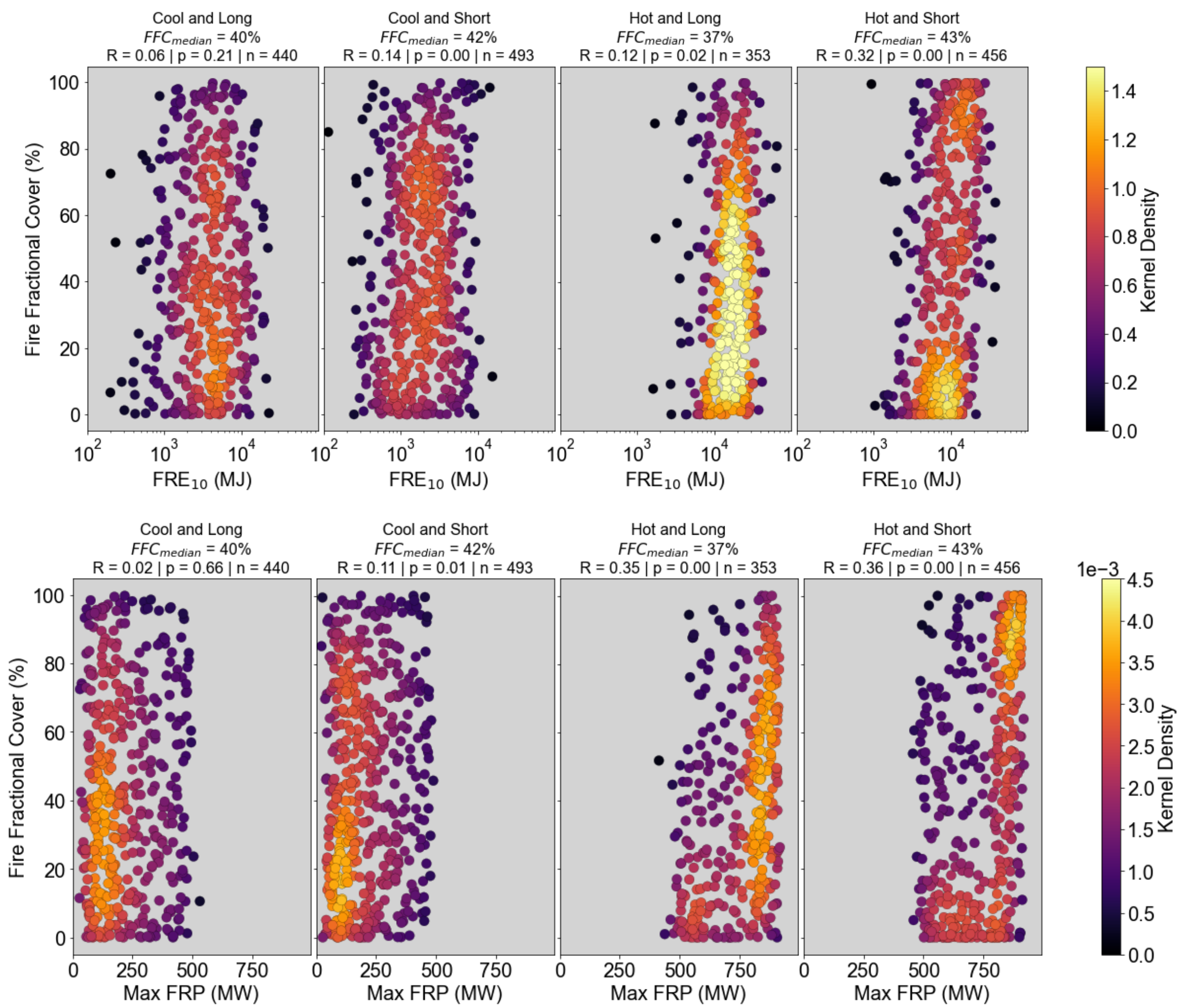

Figure 4.6 FRE_{10} (top row) and MaxFRP (bottom row) metrics plotted against Sentinel-2 FFC, showing kernel density and reporting the FFC median and correlation statistics for each plot.

The comparison between FRP-metrics and dNBR per fire type shows non-significant correlations for AHI data (Table 4.5). Meanwhile, Sentinel-2 data demonstrate weak correlations with MaxFRP in hot-and-short and hot-and-long fires, and a weak correlation only within the hot-and-short fires in the case of FRE_{10}.

Table 4.5 Correlations of dNBR and FRP metrics based on fire type. Pearson's correlation coefficient (R) and associated p-value ($p<0.05$ indicates a statistically significant correlation), and sample size (n) are provided. Green denotes significant correlations.

dNBR vs MaxFRP	Cool-and-long			Cool-and-short			Hot-and-long			Hot-and-short		
	R	p	n	R	p	n	R	p	n	R	p	n
Sentinel-2	0.02	0.69	440	0.15	0.00	493	**0.33**	0.00	353	**0.39**	0.00	456
AHI	0.07	0.12	440	0.15	0.00	493	0.27	0.00	353	0.17	0.00	456

dNBR vs FRE_{10}	Cool-and-long			Cool-and-short			Hot-and-long			Hot-and-short		
	R	p	n	R	p	n	R	p	n	R	p	n
Sentinel-2	0.08	0.09	440	0.21	0.00	493	0.11	0.05	353	**0.33**	0.00	456
AHI	0.04	0.43	440	0.14	0.00	493	0.10	0.07	353	0.14	0.00	456

The binary K-Means clustering used for the burned/unburned area classification (4.2.5) resulted in varying thresholds for the different fire types (Table 4.6). MaxFRP has a significant effect on the threshold derivation as the hot fires have a higher dNBR threshold compared to the cool fires. However, the persistence of the fire does not have a clear impact on the thresholds, as seen by the difference (0.01) among long and short fires.

Table 4.6 dNBR thresholds used to define burnt and unburned area based on Sentinel-2 data within a BRIGHT/AHI hotspot, derived by K-Means clustering (4.2.5)

	dNBR threshold
Hot-and-long	0.23
Hot-and-short	0.24
Cool-and-long	0.16
Cool-and-short	0.15

When setting equal sample sizes across groups, FFC reveals moderate and strong correlations between the FRP metrics and Sentinel-2 dNBR, and weak correlations with AHI dNBR (Table 4.7). A peak in correlations is observed between 23% and 60% of FFC, which is higher for MaxFRP for both dNBR datasets. Moreover, the FFC interval range for the constant sample size is increasing from 7% in the first group, to 20% in the 60-80% and 80-100% groups, indicating that the frequency of fires occupying larger percentages of an AHI pixel is decreasing with increasing FFC.

Table 4.7 Correlations of dNBR and FRP metrics based on groups equal number of observations (n=~290) and FFC interval. The FFC percentage corresponds to the percentage of an AHI pixel that was burned based on Sentinel-2 data. Green denotes weak, yellow moderate, and red strong correlations. For all correlations p<0.0.5.

dNBR vs MaxFRP	FFC 0-7%	FFC 7-23%	FFC 23-41%	FFC 41-60%	FFC 60-80%	FFC 80-100%
Sentinel-2	**0.45**	**0.58**	**0.71**	**0.75**	**0.67**	**0.54**
AHI	0.13	**0.31**	**0.34**	**0.32**	0.21	0.24

dNBR vs FRE_{10}	FFC 0-7%	FFC 7-23%	FFC 23-41%	FFC 41-60%	FFC 60-80%	FFC 80-100%
Sentinel-2	**0.37**	**0.51**	**0.66**	**0.59**	**0.56**	**0.42**
AHI	0.12	0.20	**0.31**	0.14	0.08	0.24

A further stratification based on land cover types (Table 4.8 and Table 4.9) repeats the correlation statistics for the FFC groups. Again, the correlations between Sentinel-2 dNBR and MaxFRP are higher compared to AHI dNBR and most land covers peak between 7% and 60% FFC. Furthermore, correlations are higher in land covers with more complex vegetation (woodlands and forests), while simpler structure vegetation lacks significant populations in higher FFC groups. The same analysis for FRE_{10} shows similar but less significant associations and therefore was not included here to avoid repetition.

Table 4.8 Sentinel-2 dNBR and MaxFRP association statistics per combination of FFC and land cover. Significant correlations are highlighted based on their strength, the p-value and sample size (>=25). Green denotes weak, yellow moderate, and red strong correlations.

S2 dNBR vs MaxFRP	FFC 0-7%			FFC 7-23%			FFC 23-41%			FFC 41-60%			FFC 60-80%			FFC 80-100%		
	R	p	n	R	p	n	R	p	n	R	p	n	R	p	n	R	p	n
Agriculture	0.65	0.08	8	0.50	0.10	12	0.20	0.67	7	-0.63	0.57	3	-	-	-	-1.00	1.00	2
Pasture	**0.48**	0.01	27	0.74	0.00	13	0.80	0.00	11	0.68	0.01	13	0.66	0.05	9	0.51	0.11	11
Shrubs	**0.53**	0.00	82	**0.64**	0.00	47	**0.82**	0.00	26	0.94	0.00	9	0.95	0.05	4	-	-	-
Sparse vegetation	**0.65**	0.00	64	**0.79**	0.00	28	0.83	0.00	16	0.50	0.07	14	0.69	0.00	17	1.00	1.00	2
Grass	0.20	0.56	11	0.66	0.00	20	0.84	0.00	23	0.80	0.00	24	**0.37**	0.01	44	0.32	0.14	23
Open woodland	0.16	0.51	20	**0.44**	0.00	45	**0.63**	0.00	39	**0.71**	0.00	47	**0.53**	0.00	35	0.39	0.07	23
Woodland	-0.03	0.88	28	**0.60**	0.00	40	**0.65**	0.00	39	**0.85**	0.00	46	**0.80**	0.00	50	**0.85**	0.00	39
Open forest	0.34	0.07	30	**0.56**	0.00	48	**0.75**	0.00	56	**0.79**	0.00	63	**0.71**	0.00	60	**0.64**	0.00	75
Closed forest	0.53	0.01	21	**0.44**	0.01	38	**0.73**	0.00	74	**0.75**	0.00	72	**0.63**	0.00	71	**0.47**	0.00	111

Table 4.9 AHI dNBR and MaxFRP association statistics per combination of FFC and land cover. Significant correlations are highlighted based on their strength, the p-value and sample size (>=25). Green denotes weak, yellow moderate, and red strong correlations.

AHI dNBR vs MaxFRP	FFC 0-7%			FFC 7-23%			FFC 23-41%			FFC 41-60%			FFC 60-80%			FFC 80-100%		
	R	p	n	R	p	n	R	p	n	R	p	n	R	p	n	R	p	n
Agriculture	0.14	0.74	8	0.18	0.58	12	-0.08	0.86	7	-0.91	0.27	3	-	-	-	-1.00	1.00	2
Pasture	0.31	0.12	27	0.50	0.08	13	0.53	0.09	11	0.33	0.27	13	-0.02	0.95	9	0.08	0.82	11
Shrubs	0.06	0.59	82	**0.40**	0.01	47	**0.50**	0.01	26	0.86	0.00	9	-0.27	0.73	4	-	-	-
Sparse vegetation	0.26	0.04	64	**0.51**	0.01	28	0.54	0.03	16	0.19	0.52	14	0.34	0.18	17	-1.00	1.00	2
Grass	0.13	0.71	11	0.43	0.06	20	0.64	0.00	23	0.74	0.00	24	**0.44**	0.00	44	0.25	0.26	23
Open woodland	0.15	0.52	20	0.08	0.61	45	0.19	0.25	39	**0.32**	0.03	47	0.06	0.72	35	0.36	0.10	23
Woodland	0.07	0.73	28	**0.48**	0.00	40	**0.39**	0.01	39	**0.52**	0.00	46	**0.54**	0.00	50	0.30	0.06	39
Open forest	**0.44**	0.02	30	0.26	0.08	48	0.17	0.22	56	-0.04	0.73	63	0.02	0.91	60	0.26	0.02	75
Closed forest	0.28	0.22	21	0.23	0.16	38	0.21	0.07	74	0.29	0.01	72	**0.39**	0.00	71	**0.30**	0.00	111

4.4.Discussion

Following previous work that established the confidence in fire intensity metrics derived by the BRIGHT algorithm (Chatzopoulos-Vouzoglanis et al., 2023, 2022; Engel et al., 2022), we explored the association of BRIGHT/AHI FRP to spectral differencing metrics used for burn severity estimation (dNBR). Similar studies compared MODIS FRP and Landsat NBR metrics, however, for a limited amount of case study fires (Henry et al., 2019; Heward et al., 2013). These demonstrated weak associations between metrics, due to temporal resolution limitations of polar-orbiting FRP observations. Our study expands the comparison beyond case study fires to encompass a continental scale for fires observed throughout an entire year, while including near-continuous geostationary FRP observations from AHI. The advantage of the higher temporal resolution of AHI enabled instantaneous FRP to be calculated in higher frequency from which estimations of MaxFRP and FRE_{10} could be derived with higher confidence. The results are stratified spatially using different variables representing biogeographical characteristics, land covers, vegetation types (height and density), and fire types. Our findings show that the two measures, FRP and dNBR, do not correlate well in general. However, slightly stronger correlations may be observed when hotter fires are examined, and when the dataset is stratified into subsets based on fire fractional cover using finer resolution Sentinel-2 data.

More specifically, FRP metrics and dNBR correlations do not reveal any significant patterns when examined for biogeographically homogeneous regions over the Australian continent (Figure 4.1). FRE_{10} shows moderate agreement with dNBR in more regions as compared to MaxFRP, especially on the east and north coast of Australia. FRE_{10} and MaxFRP correlations with dNBR are similar in the southwest coastal regions, while neither is correlated with dNBR in the southeastern corner of the continent, where the Black Summer Fires of 2019-2020 were particularly extreme and devastating (Fryirs et al., 2021). In general, these results indicate that for extreme events the two metrics capture different fire effects. Meanwhile the relatively higher agreement in the northern regions (Tiwi Cobourg, Arnhem Plateau, Gulf Coastal, Mount Isa Inlier - Table 4.2), which have dominant vegetation types with a complex structure (Table 4.2) and wildfires that burn cooler (Figure 4.5), suggests that dNBR and FRP metrics capture similar effects in these conditions.

The distributions of the dNBR values across different vegetation structure stratifications (Figure 4.2, Figure 4.3) demonstrate a low variability between categories and a negative association with vegetation complexity, i.e., simpler structure shows higher NBR change. On the contrary, the FRP and persistence values derived by the active fire information show a higher variability between vegetation types and a positive association. More established and complex vegetation burns for longer on average, with a higher average FRE_{10}, and a bi-modal distribution of MaxFRP where the higher mode increases with canopy height. This is significant as dNBR captures smaller changes for more intense and persistent fires in more complex environments, possibly due to canopy obstruction of the ground. The active fire metrics are more useful than dNBR to derive physically meaningful fire types to stratify the dataset (4.3.3), yet the correlation in this setting remain non-significant.

With the addition of Sentinel-2 data, we see that Sentinel-2 dNBR and AHI FRP metrics show more significant but weak correlations in the hotter fire types. Using the Fire Fractional Cover (FFC) information for each fire type the correlations become stronger, especially for partially burned AHI pixels. Among these, Sentinel-2 dNBR and MaxFRP correlate strongly in Woodlands and Forests, while moderate correlations are observed in the remaining land covers in the cases where data scarcity does not affect the statistics. AHI dNBR and MaxFRP demonstrate a similar behaviour but on fewer occasions. Overall, geostationary FRP metrics correlate well with Sentinel-2 dNBR after stratifying the analysis based on the percentage of the pixel burned (FFC). Since the same FRP estimate can result from a weakly burning large fire or a high intensity small fire, FRP estimates can be interpreted to be a function of both the fire intensity and the burning area. Stratifying by FFC helps reduce this ambiguity, leading to stronger correlations between FRP and dNBR. More complex vegetation type land covers also offer higher correlations, although this may be due to small population size in the other categories. In contrast to our initial assumptions, vegetation type appears to play an inverse role as correlations are stronger where vegetation is more structurally complex.

We expected higher correlations between the spectral differencing severity index and the fire intensity metrics, as these variables are commonly used independently to map wildfires effects. Nevertheless, the two metrics rarely correlate at continental or regional scales, with weak correlations being found when examining hotter fires only. Stronger correlations are achieved by introducing higher spatial resolution data (Sentinel-2 dNBR) and following a complex stratification methodology. The inclusion of the extreme Black Summer Fires in the dataset could have introduced bias for hotter fire types or land covers that were under-represented due to limitations on the dataset sizes. While our results are significant, future research could use larger datasets to explore different land cover effects and fire seasons in more depth.

Studies that used geostationary FRE to derive biomass burning emissions, suggest that biomass consumption estimation is possible for spatial resolutions that are typically coarse (between 0.1° and 0.5°) (Mota and Wooster, 2018; Nguyen et al., 2023). However, fire effects that play a role in the mortality and growth of individual trees require very fine spatial resolutions, which are typically not achievable with freely available satellite data (Sparks et al., 2023a). Meanwhile, the size and patchiness of burn scars along with the diurnal fluctuations of temperature and humidity can affect the ecology and vegetation recovery of local environments (Morgan et al., 2014; Williamson et al., 2022). Our results promote a synergistic use of the high-frequency FRP estimations from AHI and dNBR from Sentinel-2 for fire impact estimations that can potentially be finer than a 2km spatial resolution. By complementing existing burn severity assessment techniques with fire intensity data, we can increase our understanding of wildfire effects across large areas.

4.5. Conclusions

This study compared remotely sensed measures of wildfire intensity (FRP, FRE) and burn severity (dNBR). Contrary to our expectations, the findings demonstrate the lack of strong correlations between the two wildfire effect metrics. Sentinel-2 dNBR was weakly correlated to FRP metrics especially for lower intensity fires, however, AHI dNBR and FRP did not demonstrate significant correlations. Results show that when fire type and Fire Fractional Cover (FFC) information is combined, correlations can become strong between MaxFRP and dNBR in FFC groupings. Further stratification based on land cover and vegetation type does not reveal new insights, partially due to small sample sizes in some land cover categories. The limitations of dNBR to capture fire effects of the observed fire activity raise concerns regarding its utility in large area studies and in the absence of *in-situ* data. Future burn severity studies should consider incorporating active fire intensity information, especially when it is available at a high temporal frequency. Combining spectral difference and fire radiative power information may provide new insights into wildfire impact.

Chapter 5. Composite Wildfire Impact (CWI) rating: Integrating fire intensity and burn severity earth observations

Abstract

Current wildfire impact assessments at the landscape scale often overlook the complexity of active fire behaviour, focusing only on pre- and post-fire spectral differencing, despite remotely sensed active fire data being readily available. This study integrates high temporal resolution active fire intensity measures from geostationary satellite sensors and high spatial resolution normalised spectral differencing index products from polar-orbiting satellite sensors to produce a new approach for describing wildfire impact. Himawari-8 BRIGHT/AHI active fire detections and intensity estimations are combined with spectral differencing measures from Sentinel-2, to derive wildfire impact categories over Australia for one year of data, using a dimensionality reduction and clustering approach. The wildfire impact categories summarise fire hotspot commonalities based on their maximum and total fire intensity, duration, differenced Normalised Burn Ratio (dNBR), burned area patchiness, and pre-fire vegetation conditions, and reveal expected 2019-2020 Australian fire season patterns. Furthermore, land cover and vegetation type emerges as an important factor, with forests and woodlands reflecting more impactful fires compared to grasslands and shrublands. Comparisons with state government burn severity assessment projects reveal a moderate agreement, further stressing the need for more diverse information inclusion in such assessments. The proposed wildfire impact framework combines diverse remotely sensed wildfire behaviour information and can assist in a better understanding of wildfire effects on a continental scale. More research, leveraging longer temporal and spatial baselines and fire ecology expertise, is needed to refine the used nomenclature, as well as to reduce seasonal and regional biases for the improvement of wildfire impact assessments.

5.1. Introduction

Wildfires are a critical global environmental issue, with increasing frequency and severity, shifting fire regimes, and exacerbated by extreme fire weather conditions in the face of a changing climate (Calheiros et al., 2021; Cunningham et al., 2024; Jones et al., 2022). The detection, monitoring and characterisation of wildfires over large spatiotemporal scales is possible with earth observing satellites (Key and Benson, 2006; Wooster et al., 2021). Fire activity in the landscape can be described according to measures of fire intensity, i.e., the energy released from burning biomass, fire severity, i.e., the loss of biomass, and burn severity, i.e., a term that combines fire severity and ecosystem responses and is often used when remotely sensed and *in-situ* data are combined to describe fire effects (Keeley, 2009).

The severity of a fire is often quantified over large areas using remotely sensed normalised spectral difference indices to compare pre- and post-fire conditions (Collins et al., 2020; Fernández-Guisuraga et al., 2023a; Gerrevink and Veraverbeke, 2021). The Normalised Burn Ratio (NBR) and its pre- and post-fire difference (dNBR) have been associated with field-based and *in-situ* severity estimates, such as the Composite Burn Index (CBI) (Key and Benson, 2006) and the geometrically corrected CBI (De Santis and Chuvieco, 2009), with a plethora of studies using these metrics for burn severity assessments (Fernández-García et al., 2018; Meng et al., 2017; Parker et al., 2015; Viedma et al., 2020b).

Burn severity classification is usually implemented using simple thresholds (Finco et al., 2012; Sparks et al., 2015) or via aerial photo interpretation to train machine learning models (Collins et al., 2020, 2018; McCarthy et al., 2017). Nevertheless, spectral differencing methods can be limited, as thresholds need to be separately adjusted for each fire (Sparks et al., 2015), and dense canopy cover can cause underestimation of lower severity classes due to line-of-sight obstruction from the optical sensors (Gibson et al., 2020). Pre-fire vegetation conditions can also significantly affect burn severity estimations (Gale and Cary, 2022; Lee et al., 2024; Viedma et al., 2020b). For this reason, pre-fire NBR is often incorporated into indices such as the Relativised Burn Ratio (RBR) (Parks et al., 2014) and the Relative dNBR (RdNBR) (Miller and Thode, 2007) to normalise dNBR values for vegetation type and condition differences. However, the association between spectral indices and *in-situ* estimations of severity varies significantly across vegetation types due to combustion completeness and burned fraction of the observed area, species, height and vertical fuel connectivity differences, as well as fire history (Fernández-Guisuraga et al., 2023a; Miller et al., 2023; Parker et al., 2015; Roy and Landmann, 2005; Saberi and Harvey, 2023). These limitations of spectral differencing techniques, which commonly assess wildfire effects by comparing two static states (before and after the fire), highlight the need for more adaptive and robust methods that account for variations in fire behaviour, vegetation and environmental conditions when assessing wildfire effects.

In contrast to spectral differencing, active fire satellite observations provide snapshots of fire intensity during the course of the event. Fire hotspots can be detected by measuring the upwelling radiation of an active fire in the middle-infrared (MIR) part of the spectrum and use this information to estimate the fire intensity (Wooster et al., 2021). Certain low-earth orbiting (LEO) satellites, such as Aqua/Terra and SNPP, carry MIR-sensitive sensors that capture global fire intensity estimations twice a day at spatial resolutions ranging from 375m to 1km (Giglio et al., 2021; Schroeder and Giglio, 2018). Where near-continuous observations are available, integrated measures of fire intensity can also be described in more detail and with greater accuracy than those derived from sparse temporal observations. Newer geostationary sensors, such as the Advanced Baseline Imager (ABI) and the Advanced Himawari Imager (AHI), also have fire detection and intensity estimation capabilities, providing data every 10 minutes at 2km (Engel et al., 2022; Xu et al., 2021).

The instantaneous fire intensity of a fire can be described by the Fire Radiative Power (FRP - MW), while its time integration corresponds to the total exerted energy in the form of Fire Radiative Energy (FRE - MJ) (Wooster et al., 2005, 2003). Active fire earth observations are often used for timely fire detection (Engel et al., 2021b; Xu et al., 2021, 2020), fire intensity and burning biomass emissions estimations (Ichoku and Ellison, 2014; Li et al., 2022; Nguyen et al., 2023). Additionally, fire intensity and radiative transfer of heat to tree trunks have been linked to adverse effects on their growth, survival rates and a decrease in net primary productivity (Smith et al., 2016; Sparks et al., 2023b, 2018, 2017; Subasinghe Achchige et al., 2022). Active fire data can provide valuable insights into fire ignition, progression, and duration, offering opportunities for more informed wildfire characterisation.

Despite the value of active fire data, there remains a notable disconnect between fire intensity metrics and burn severity indices. Studies have shown unexpectedly weak correlations between FRP and spectral indices such as dNBR (Chatzopoulos-Vouzoglanis et al., 2024; Heward et al., 2013). For example, Himawari-8 AHI-derived fire metrics such as maximum FRP and FRE exhibited weak associations with Sentinel-2 dNBR during Australia's 2019-2020 fire season. This weak relationship persists, though it slightly improves for high-intensity fires (Chatzopoulos-Vouzoglanis et al., 2024). These findings suggest there may be utility in combining active fire observations with burn severity metrics to provide a more comprehensive characterisation of wildfires and typology of impact than either one alone. Nonetheless, we recognise that the combination of active fire and reflectance data is not a new concept (Roy, 1999), and it is implemented in the MODIS burned area calculation (MCD64A1) (Giglio et al., 2018).

In this study, we investigate the outcomes of integrating fire intensity estimates with burn severity data using a clustering approach and propose a new wildfire impact rating system. We coin the term “composite wildfire impact” (CWI) to mean the composite effects on vegetation, ecosystems and the landscape as described by remotely sensed spectral changes and the release of energy from burning biomass. The rating system is applied to Australia, utilising active fire data from BRIGHT/AHI (Engel et al., 2022) and burn severity metrics from Sentinel-2 over one year (April 2019 – March 2020). Our aim in combining active fire and burn severity metrics is twofold: i) to propose a new classification scheme for describing and categorising fire impact, and ii) to demonstrate the insights gained from this integration.

5.2.Data and Methods

5.2.1. Study area and period

The study area encompasses Australia (including Tasmania), covering a variety of climatic regions and land covers, from savannas in the north, to temperate forests in the southeast, and arid shrublands in the west. The land cover was characterised using the Dynamic Land Cover Dataset (DLCD v2.1) provided by Geoscience Australia. The dataset includes 22 land cover classes, mapped using MODIS data at 250m over the continent using observations made between January 2014 and December 2015. The overall accuracy of the dataset is 81.5% (Lymburner et al., 2015). The study period extends from April 2019 to March 2020 and includes one of the most extreme wildfire seasons experienced on the continent (Abram et al., 2021; Collins et al., 2021; Fryirs et al., 2021).

5.2.2. Geostationary and polar-orbiting derived wildfire data

Active fire detections and FRP estimations from the Himawari-8 BRIGHT/AHI dataset (Bessho et al., 2016; Engel et al., 2022, 2021b, 2021a) are chosen as a high-confidence dataset following past work by Chatzopoulos-Vouzoglanis et al. (2024, 2023, 2022). Each data record corresponds to a 2km AHI pixel that includes a fire, which is cross-referenced by checking co-occurrence with VIIRS VNP14IMG fire detections (Schroeder and Giglio, 2018). A randomly selected subset of the original dataset (~170,000 active fire detection records) comprised of ~1700 records is used, including only fires with a maximum duration of seven days, to further limit the effect of outliers and false detections in the analysis (Chatzopoulos-Vouzoglanis et al., 2024). From this dataset, the maximum FRP, the FRE and the duration of a fire hotspot were selected for analysis (Table 5.1), as they were considered to adequately describe the important aspects of each continuous fire event.

Sentinel-2 Near Infrared (narrow bandwidth NIR centred at 865nm – band 8A) and Short-wave Infrared (SWIR centred at 2190nm – band 12) data at a spatial resolution of 20m were acquired from the Geoscience Australia Open Datacube (ESA, 2015; Krause et al., 2021). The Geoscience Australia Sentinel-2 data is already atmospherically corrected and transformed into surface reflectance values using the MODTRAN4 radiative transfer model (Li et al., 2010). These datasets were used to compute the NBR pre- and post-fire at 20m spatial resolution for the extent of each 2km BRIGHT/AHI pixel, using the first and last BRIGHT/AHI detection to define the active fire phase. Consequently, the average dNBR over the 2km BRIGHT/AHI pixel extent was computed (similar to Chatzopoulos-Vouzoglanis et al. (2024)). The Fire Fractional Cover (FFC) was calculated as the percentage of Sentinel-2 pixels within each 2km BRIGHT/AHI pixel extent classified as burned, defined by applying a threshold of dNBR≥0.15. Finally, the pre-fire NBR was also separately included as an indicator of pre-fire vegetation health (Table 5.1). This choice was made as the data was already available from the dNBR calculation, and as it is often included in different burn severity indices such as RBR and RdNBR (Miller and Thode, 2007; Parks et al., 2014).

Table 5.1 Summary table of the BRIGHT/AHI and Sentinel-2 variables used in the analysis, including a brief description of each variable and measurement units.

Variable	Description	Unit	Dataset
MaxFRP	Maximum FRP from a fire in a single AHI pixel	MW	BRIGHT/AHI hotspots
FRE	Integrated FRP from a fire in a single AHI pixel. This is log-transformed in the analysis (FRE_{log}) as the value distribution is highly skewed.	MJ	BRIGHT/AHI hotspots
Duration	The duration of fire in a single AHI pixel	Days	BRIGHT/AHI hotspots
$dNBR_{\mu}$	The average dNBR value for all the Sentinel-2 pixels situated within a BRIGHT/AHI pixel/hotspot	Unitless	Sentinel-2 bands 8A and 12
FFC	Fire Fractional Cover, or the percentage of the AHI pixel that was burned based on a dNBR threshold	%	Sentinel-2 bands 8A and 12
NBR_{pre}	The average NBR value for all Sentinel-2 pixels within an AHI pixel before a fire	Unitless	Sentinel-2 bands 8A and 12

5.2.3. State-issued burn severity data

Burn severity data issued by state authorities are used to gauge the CWI ratings developed in this study. The New South Wales Department of Climate Change, Energy, the Environment and Water (NSW DCCEEW, 2020) and Victorian Department of Energy, Environment and Climate Action (VIC DEECA, 2020) in Australia conducted burn severity mapping following the 2019-2020 Black Summer fires using Sentinel-2 data. The data is classified into ordinal severity ratings at a 20m spatial resolution using a Random Forest classifier and training data collected through aerial photo interpretation (Collins et al., 2018; Gibson et al., 2020). While these datasets might be biased towards the after-fire reflectance and normalised spectral differencing methods, they are the only source of ground truth data available for comparison with the results of this study. The two burn severity datasets also differ in terms of severity ratings, descriptions, and derivation methods. For this study, the two rating schemes were reclassified into a single scheme (Table 5.3) to match each other's class descriptions.

Table 5.2 Severity rating description and matching nomeclature of the VIC and NSW Black Summer Fires (2019-2020) severity assessments (NSW DCCEEW, 2020; VIC DEECA, 2020). Excluded classes were not used in this study.

VIC severity ratings and description		**NSW severity ratings and description**		**Matched Severity Rating**
6	Canopy Burnt (> 20% of canopy consumed)	5	Extreme (full canopy consumption)	6
5	High canopy scorch (> 80% of canopy scorched)	4	High (complete canopy scorch, partial canopy consumption)	5
4	Medium canopy scorch (20-80% of canopy scorched)	3	Moderate (partial canopy scorch) – 3	4
3	Low canopy scorch (<20% of canopy scorched but understorey burnt)	2	Low (burnt understorey, unburnt canopy)	3
2	Unburnt (>90% canopy and understorey unburnt)	1	Unburnt	2
1	Non-woody vegetation (Unclassified)	-	-	Excluded*
0	No data	-	Reserved class	Excluded*

5.2.4. Data analysis

The methodology is summarised in the flow chart of Figure 5.1. Following the data selection, pre-processing and construction of the dataset described in 5.2.2 and Table 5.1, dimensionality reduction and clustering techniques were applied to the dataset. Then an ensemble clustering technique was used to combine all the outputs and the CWI ratings were derived using the consensus clusters. Finally, the CWI ratings were compared to the burn severity ratings described in 5.2.3 and Table 5.3.

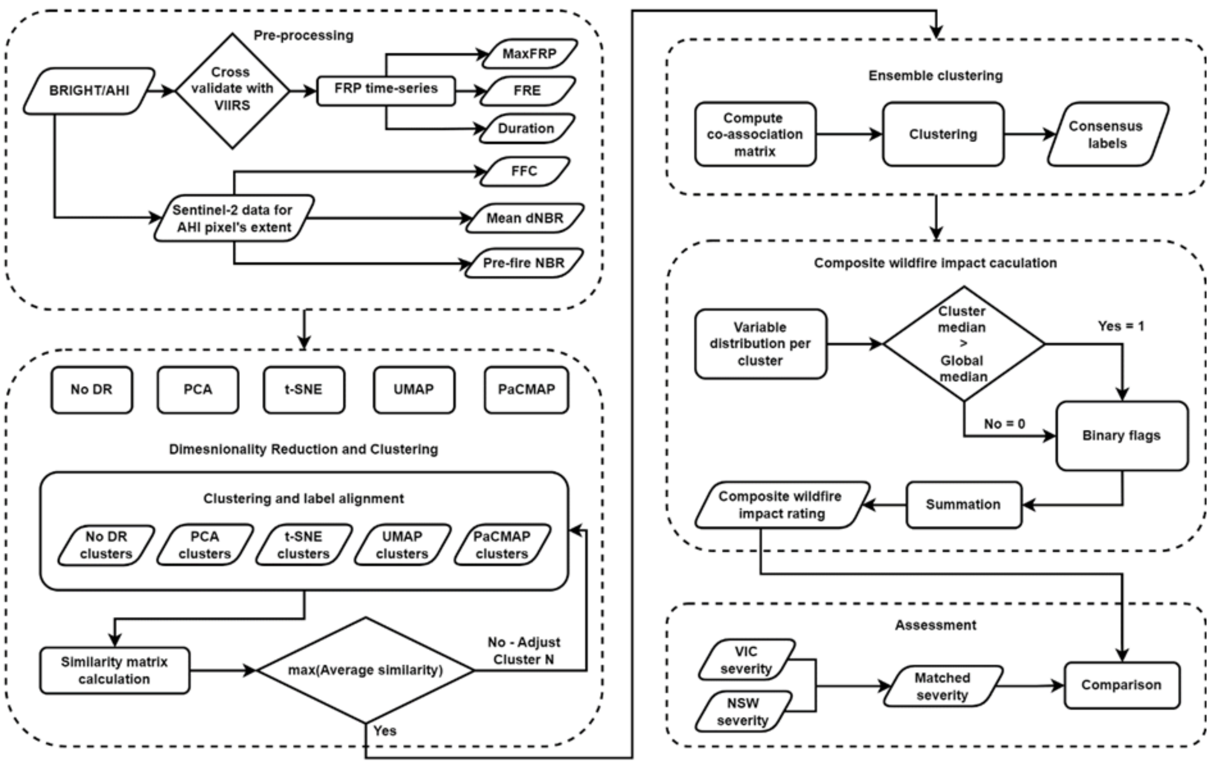

Figure 5.1 Flowchart of the methodology used to derive the composite wildfire impact ratings in this study.

5.2.4.1. Dimensionality Reduction and Clustering (DRC) techniques

Wildfire characterisation studies often use unsupervised methodologies to categorise large and diverse datasets. The methods followed in such studies include a dimensionality reduction (DR) technique which is most often a Principal Component Analysis (PCA) followed by a clustering technique to create meaningful fire categories in the absence of ground truth data (Fernández-Guisuraga et al., 2023b; Viedma et al., 2020a; Zubkova et al., 2022). While PCA does not require any assumptions regarding the feature distribution, it produces components that are a linear combination of the original features (Jolliffe and Cadima, 2016) and therefore is unable to model non-linear associations that may be present in diverse environmental datasets.

Meanwhile, there exist DR techniques that can deal with non-linear feature associations and reproject a dataset in two dimensions, while preserving local and global neighbourhood between data records. Such techniques include the t-distributed Stochastic Neighbour Embedding (t-SNE) (van der Maaten and Hinton, 2008; Van Der Maaten and Hinton, 2012), the Uniform Manifold Approximation and Projection for Dimension Reduction (UMAP) (McInnes et al., 2020, 2018) and the Pairwise Controlled Manifold Approximation (PaCMAP) (Wang et al., 2021), which are popular tools in various fields e.g., machine learning, and bioinformatics (Becht et al., 2019; Belkina et al., 2019; Huang et al., 2022; Mallick et al., 2023). t-SNE and UMAP are better at preserving the local structure of the data, with t-SNE being more computationally expensive than UMAP (McInnes et al., 2020). Meanwhile, PaCMAP is one of the latest non-linear DR techniques developed to preserve both the local and global data structure (Wang et al., 2021). An in-depth review and comparison of these tools is beyond the scope of this paper and is already covered in some of the cited studies, however, they were chosen as representative examples of what the state-of-the-art DR can offer to wildfire characterisation compared to PCA. In this study, dimensionality reduction was applied prior to clustering to reduce noise due to collinear features, while improving the performance of distance-based clustering methods that are known to perform poorly when applied to high-dimensional datasets (Aggarwal et al., 2001).

5.2.4.2. Dimensionality Reduction Implementation

Each dataset variable (Table 5.1) was standardised independently to have a zero mean and a unit variance and then processed with PCA, t-SNE, UMAP and PaCMAP. For PCA, the first three principal components (PCs) had an eigenvalue equal or greater than one, and thus were retained for further analysis as their variance was greater than the variance of any single feature (Fernández-Guisuraga et al., 2023b; Kaiser, 1960; Zubkova et al., 2022). In the case of t-SNE, the hyperparameters were chosen based on the default value or upper ranges suggested by the Python library scikit-learn, i.e., perplexity (similar to number of neighbours) was set to 50, number of iterations to 1000 and the dataset was reduced to two dimensions (Pedregosa et al., 2011). Similarly, for UMAP and PaCMAP the number of neighbours was set to 50 and 10 respectively, while the other hyperparameters were kept to their default values. While there is a wide range of possible values for these hyperparameters, minimal experimentation was conducted as small changes in their range did not affect the results significantly, and fine tuning these models is beyond the scope of this study. However, as the initialisation conditions can have a more significant impact on the results of t-SNE, UMAP and PaCMAP (Wang et al., 2021), the initial conditions for the embedding were set based on PCA and the random-state parameter was selected through an iterative process that maximised cluster similarity across all DRC outputs.

Agglomerative Hierarchical Clustering (Pedregosa et al., 2011) using the ward linkage criterion (Ward, 1963) to minimize the variance of the clusters that are being merged was implemented to the three PCs and the two dimensional components of t-SNE, UMAP and PaCMAP. The clustering method was chosen based on previous studies (Fernández-Guisuraga et al., 2023b; Zubkova et al., 2022) and visual inspection of the resulting clusters compared to other methods (e.g., K-Means).

The optimal number of clusters used was set as the one that maximized the cluster similarity among the DR methods. First, a contingency table was constructed for each pair of clustering outputs, where the cluster labels from one clustering method were arranged along the rows and the ones from the second method along the columns. The values in each cell represented the number of records corresponding to the intersection of labels from the two clustering outputs, capturing the co-occurrence of labels between the methods (Agresti, 2019). Next, the cluster labels between each pair of clustering outputs were aligned using the Hungarian algorithm (Kuhn, 1955), which identifies the optimal one-to-one matching between two sets. The alignment was based on the Jaccard Index (ratio of intersection over union) between the two cluster outputs to ensure that the clusters with the highest overlap were matched (Kotu and Deshpande, 2015). Finally, the similarity score between the aligned outputs was calculated as the ratio of commonly clustered records over the total records, and the number of clusters that provided the higher similarity was chosen. While the above methodology assumes a similar sensitivity to cluster number across the DR outputs, it is acknowledged that this was a practical compromise, as the structure of each DR output may respond differently to the same number of clusters.

5.2.4.3. Ensemble clustering

The lack of validation data made it difficult to determine the optimal DRC technique. As a result, an ensemble clustering technique was employed to integrate and preserve information from multiple outputs, using the methodology proposed in Fred and Jain (2005). The co-association matrix was calculated by counting the occurrence in the same cluster for each pair of records between two different clustering outputs. This was repeated for all possible pairs of clustering outputs and resulted in an $n \times n$ matrix for n records where each cell had the ratio of total occurrences divided by total possible occurrences (number of clustering outputs in the ensemble). Then, agglomerative hierarchical clustering was applied on the co-association matrix to map the different data partitions and produce the consensus labels of the ensemble clustering (Fred and Jain, 2005).

5.2.4.4. Composite wildfire impact calculation

The median of each variable for the data in each cluster was used as a descriptive statistic to summarise the central tendency of each cluster variable. This cluster-specific median was then compared to the global dataset median for that variable. A binary flag was assigned based on whether the cluster median was higher or lower than the global median. Subsequently, the binary flags for each cluster were aggregated into an impact rating R (where $R \in [0, n]$, with n representing the total number of variables). The ratings were then manually assigned six ordinal labels ranging: “Very Low”, “Low”, “Medium”, “High”, “Very high”, and “Extreme”.

5.2.4.5. Assessment

The calculated CWI ratings were compared to the reclassified state-issued burn severity ratings (Table 5.3). The state-issued burn severity ratings (20m) within the extent of each BRIGHT/AHI hotspot (2km) were aggregated using the mean value of the ordinal values to achieve a consistent spatial resolution between the two datasets and retain the effect of all severity ratings into the final aggregation. This approach addresses potential bias that a median or majority voting aggregation method would introduce, especially for smaller fires.

5.3. Results

5.3.1. Data exploration

Reporting both Pearson’s and Spearman’s correlation for every pair of variables, Figure 5.2 presents the results in a pairwise plot that includes scatterplots illustrating the association between the BRIGHT/AHI and Sentinel-2 variables. $MaxFRP$ and FFC have bi-modal distributions, while log-transformed FRE and $dNBR$ values are pseudo-normally distributed, and Duration and NBR_{pre} values are left-skewed. Strong correlations were found between $MaxFRP$ and FRE, $dNBR$ and FFC, however their scatterplots reveal a non-linear aspect in their associations. $MaxFRP$ and $dNBR$ have a moderate correlation that increases non-linearly as values increase. Additionally, relationships between $MaxFRP$-NBR_{pre}, $MaxFRP - FFC$, $FFC - Duration$ reveal clusters with varying point densities.

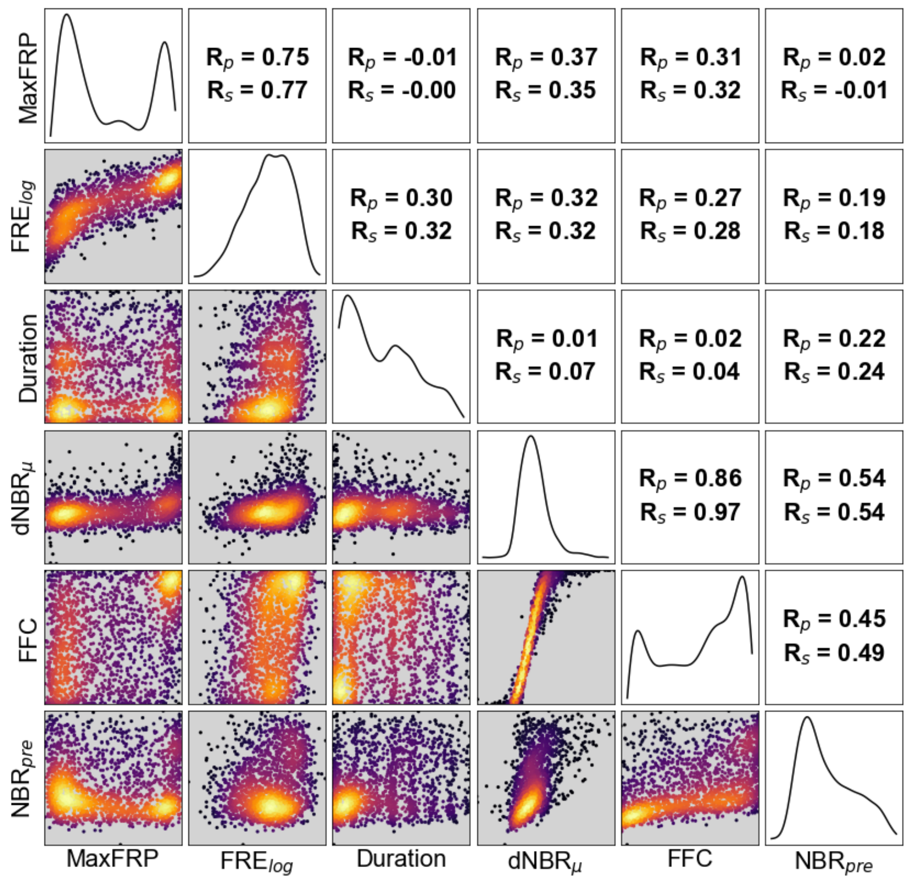

Figure 5.2 Pairwise variable comparison. The diagonal presents each variable's probability density function, Pearson's (R_p) and Spearman's (R_s) correlation coefficients are shown above the diagonal, and the pairwise scatterplots are shown below the diagonal. The colour gradient in the scatterplots signifies density, with lighter colours representing higher density and vice versa.

5.3.2. Dimensionality reduction and clustering tuning

While the components of the non-linear methods were harder to interpret, PCA offered insights for the dataset through its components (PCs) (Figure 5.3). Using the Kaiser criterion (5.2.4.2) the first three PCs were analysed, describing 45%, 23% and 18% of the variance, respectively. PC1 explained 45% of the variance in the dataset, with $dNBR_{\mu}$, FFC and NBR_{pre} contributing most, while $MaxFRP$ and FRE also played a role. This relation is reversed in PC2, with the active fire metrics contribution being more significant, however, this component only described 23% of the variance. Finally, PC3 explained 19% of the variance and was mostly affected by the fire duration variable.

In addition, the PCA biplot revealed that the contribution of most of the variables was roughly equal in the components, except for the duration that had a much smaller contribution, as signified by the arrow length in Figure 5.3. Moreover, the direction of the arrows suggests that the active fire metrics and normalised spectral differencing metric groups did not correlate with each other (almost perpendicular to each other), while the intra-group correlations are positive (pointing in the same direction).

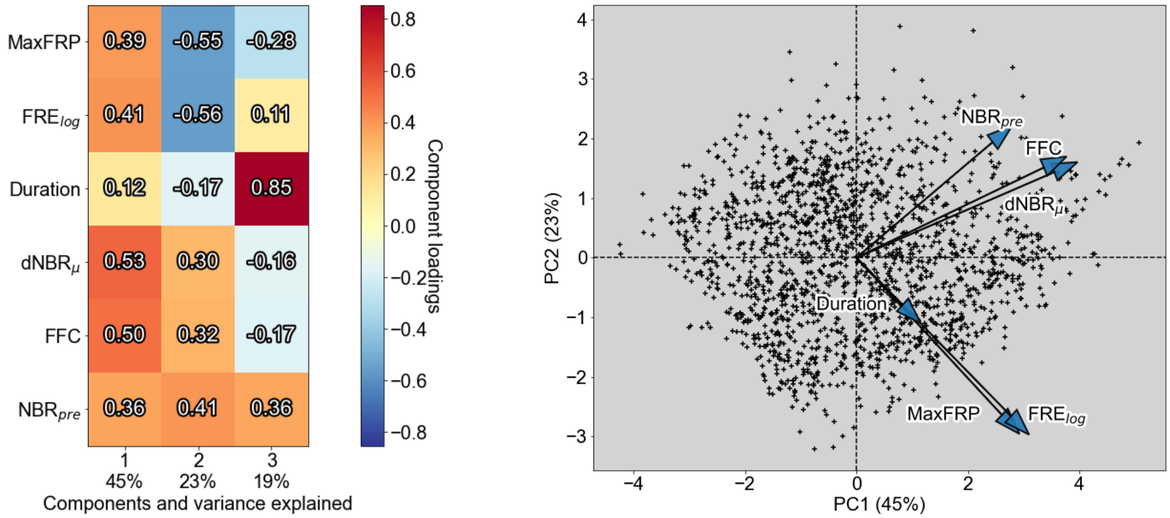

Figure 5.3 First three components of PCA (Kaiser criterion) and component loadings (left). PCA biplot of dataset fires across the first two principal components, with arrows indicating the direction and contribution of each variable, scaled by a factor of 10 for readability (right).

After trialling cluster numbers between 2 and 16 (step = 2), the maximum average similarity among pairs of clustering outputs was achieved using 8 clusters for all DR techniques. Additionally, limited experimentation with the random state parameter, using values ranging from 0 to 100, identified that a random state of 6 produced the highest similarity when evaluated on an eight-cluster output (Figure 5.4). The random state parameter affects the random number generator used for the various stochastic processes followed in the different DR technique computations. Setting its value to be constant increases reproducibility and eliminates randomness, as the same results are produced with each run (Pedregosa et al., 2011).

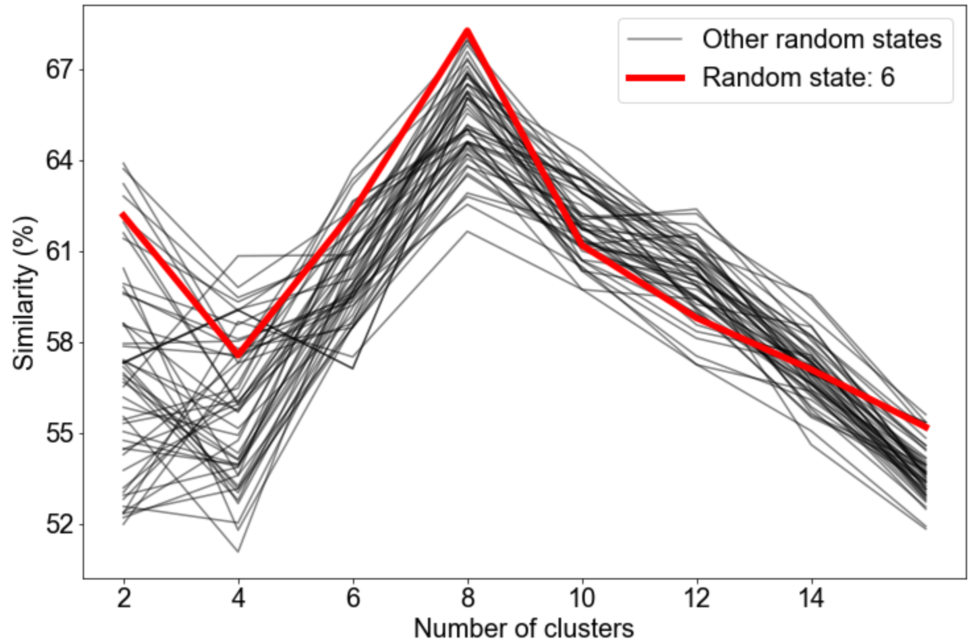

Figure 5.4 Total similarity between cluster outputs using a different number of clusters and initialisation parameter of random state. The red line corresponds to the random state number that maximised the similarity in the 8th cluster.

Table 5.3 shows the pairwise similarity scores between DRC results (5.2.4.2) along with each method's average similarity score. While the optimal number of clusters was selected based on maximising overall similarity among DR outputs, these results are informative as they quantify how consistently each DR method agrees with the others in assigning records to clusters. Higher similarity indicates that the DR outputs yield comparable cluster structures, implying robustness to methodological variations. UMAP is the method with the highest average similarity (72.9%) and it is 79.2% similar to PaCMAP that has an average similarity of 71.1%. PCA is the least similar method with an average similarity of 64.5%, followed by t-SNE with 65.4%. Overall, the range of the average similarities is 8.4%, suggesting moderate differences in how each DRC method captured the data's cluster structure.

Table 5.3 Similarity between clustering outputs, represented by the percentage (%) of records that have been clustered together in each pair of methods. Some cells are left empty to avoid repletion of values. The last column corresponds to the average similarity for each method.

	NoDR	**PCA**	**t-SNE**	**UMAP**	**PaCMAP**	**Average**
NoDR	-	-	-	-	-	67.5
PCA	61.2	-	-	-	-	64.5
t-SNE	59.4	65.3	-	-	-	65.4
UMAP	73.9	67.9	70.7	-	-	72.9
PaCMAP	75.5	63.5	66.0	79.2	-	71.1

5.3.3. Ensemble clustering

The co-association values corresponding to each pair of records are presented in Figure 5.5. These values were derived from applying ensemble clustering to the six-variable dataset, to preserve common information among the different DRC outputs. Clustering the co-association matrix and sorting the records along the x and y axes according to the consensus labels, creates a clearer representation of the consensus clusters. The nine consensus clusters are also presented in Figure 5.5, and they are shown by the light green co-association value squares. The number of clusters was chosen as the one that maximised the average inter-cluster co-association values, minimised the average intra-cluster co-association values, and did not allow for the creation for disproportionally small clusters, which was the case for higher values.

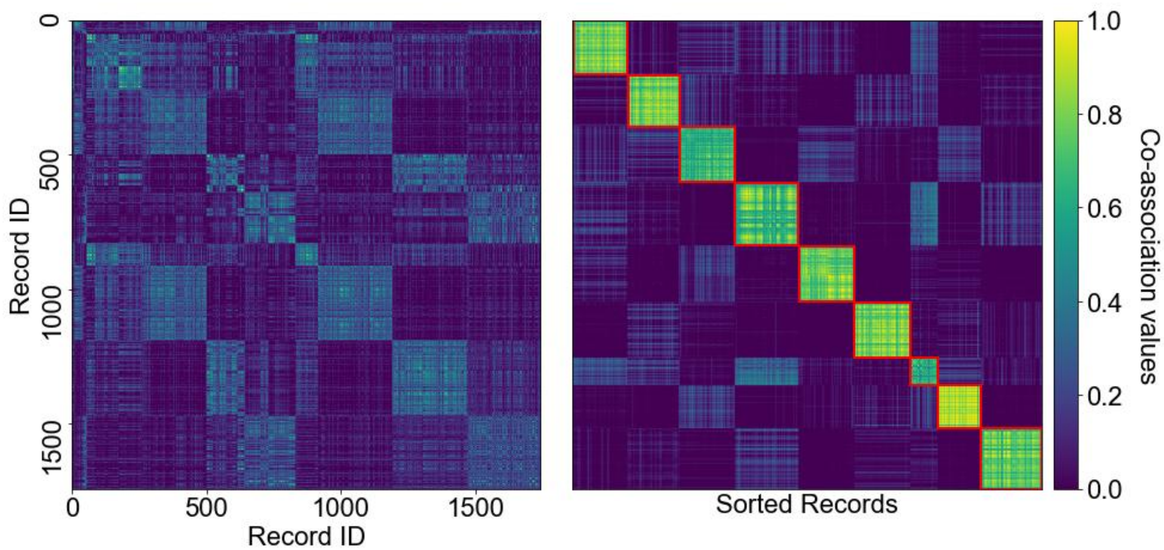

Figure 5.5 Co-association matrix before clustering (left) and after clustering and sorting of the record indices according to the consensus clusters (right). The clusters are represented by the red boxes on the right graph.

5.3.4. Wildfire impact assessment

The variable distributions per consensus cluster are presented in Figure 5.6. The clusters are sorted from top to bottom based on decreasing $dNBR_{\mu}$, while the green and red shades signify whether the variable median is higher or lower than the global variable median, respectively. Clusters 5 (C5) and 3 (C3) have the highest statistics overall, signifying wildfires of high impact, while C9 and C2 include fires with low values in most variables, most likely corresponding to lower impact fires. However, the remaining clusters have nuanced differences between each other, that make them less straightforward to characterize based on a single notion. For example, the fire intensity variables of C4 and C1 were low, with higher normalised spectral differencing variables, while C6 had high fire intensities and lower normalised spectral differencing values.

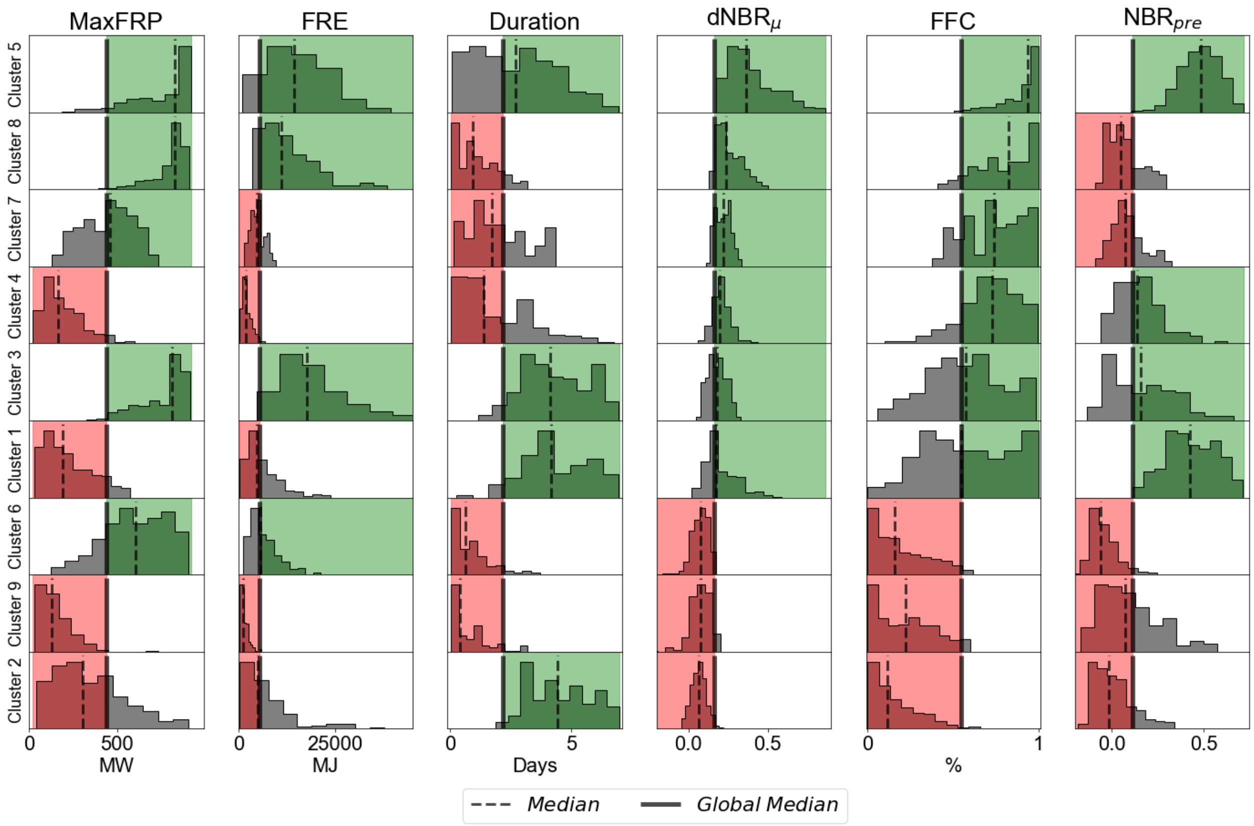

Figure 5.6 Variable distribution per consensus cluster. The x axis of the graph corresponds to the six variables of the datasets, while the y axis corresponds the different cluster labels. The shade indicates whether the cluster variable median is higher (green) or lower (red) than the global variable median.

In addition, the generalised land covers in each cluster were derived and presented in Table 5.4, as they correspond to an assumed gradual increase in accumulation of biomass. Clusters C1, C3 and C5 represent locations where forests are the major land cover, woodland and mixed cover clusters are represented by C2, C4, C7, C8, and C6 includes mostly grassland and shrublands.

Table 5.4 Distribution of land covers (Lymburner et al., 2015) in each cluster.

Land covers	**Clusters**								
	1	**2**	**3**	**4**	**5**	**6**	**7**	**8**	**9**
Agriculture	0%	4%	0%	1%	1%	4%	0%	0%	6%
Grasses and shrubs	2%	43%	11%	39%	1%	68%	34%	33%	48%
Woodlands	3%	32%	38%	31%	1%	22%	53%	47%	23%
Forests	95%	21%	51%	29%	97%	6%	13%	21%	23%

Figure 5.7 presents the relationships arising from combining the information from Figure 5.6 and Table 5.4, and reveals a connection between land cover and impact. Here, forests occupy the higher impact

space, while grasslands/shrublands are represented by medium impact ratings. Table 5.5 shows the majority impact category and the number these occurred per land cover type. Specifically, forests had predominantly extreme CWI ratings and the most occurrences (307), woodlands had a majority of high CWI impact ratings (128), grasslands and shrublands had a majority of medium CWI ratings (142), and agriculture had a majority of very low ratings and the fewest occurrences (14).

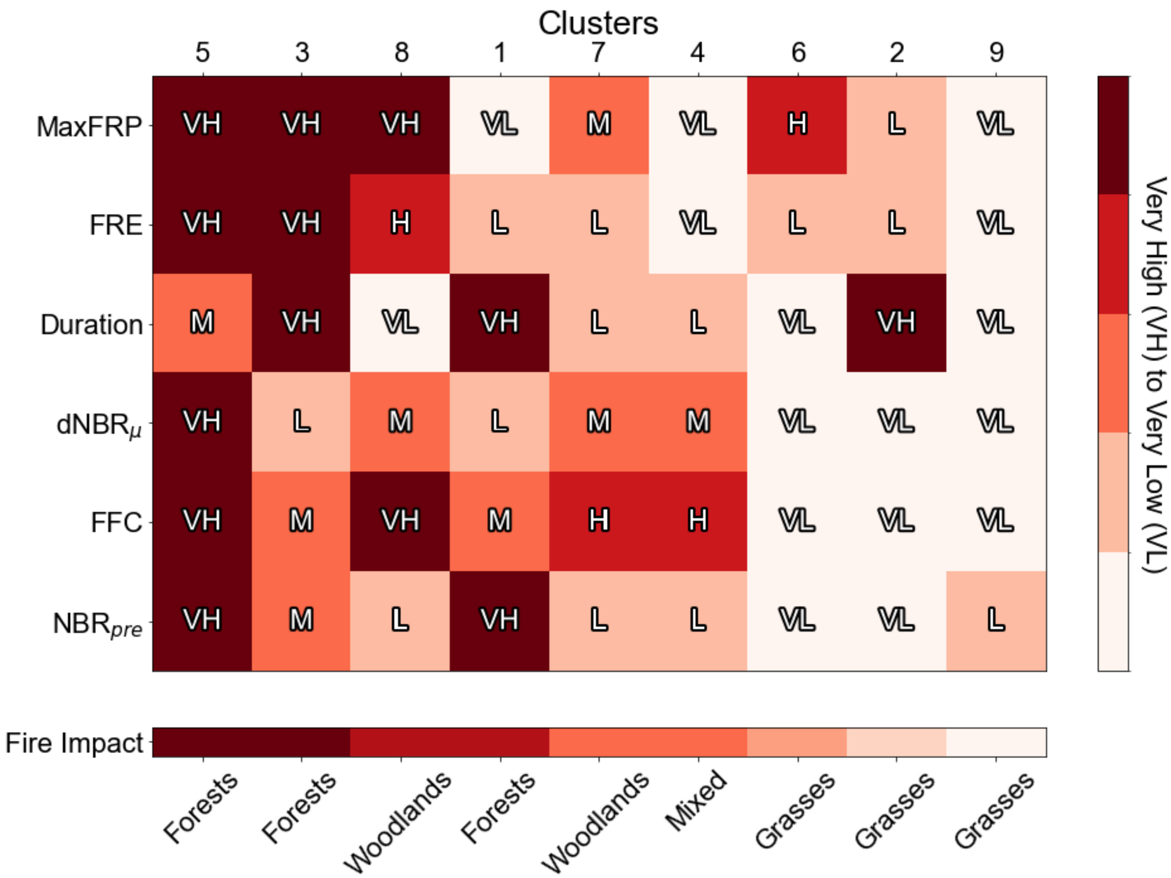

Figure 5.7 Qualitative representation of the variable medians per cluster. The clusters are sorted from highest to lowest fire impact, which corresponds to the flag accumulation. The variable medians are categorised qualitative as Very High (VH), High (H), Medium (M), Low (L) and Very Low (VL).

Table 5.5 Majority (mode) composite wildfire impact rating and number of occurrences within each land cover type.

	CWI rating mode	**Occurrences**
Agriculture	Very Low	14
Grasses and Shrubs	Medium	142
Woodlands	High	128
Forests	Extreme	307

The CWI ratings were also visualised over Australia, revealing spatial patterns of specific ratings (Figure 5.8). Namely, the fires in the southeast that correspond to the Black Summer Fires have extreme ratings, with very high and extreme ratings also being present in the southwest. The fires in the north are mostly of high impact, while the fires closer to the middle (border of Western and South Australia) create a medium impact cluster. Finally, lower impact fires are spread randomly across the continent.

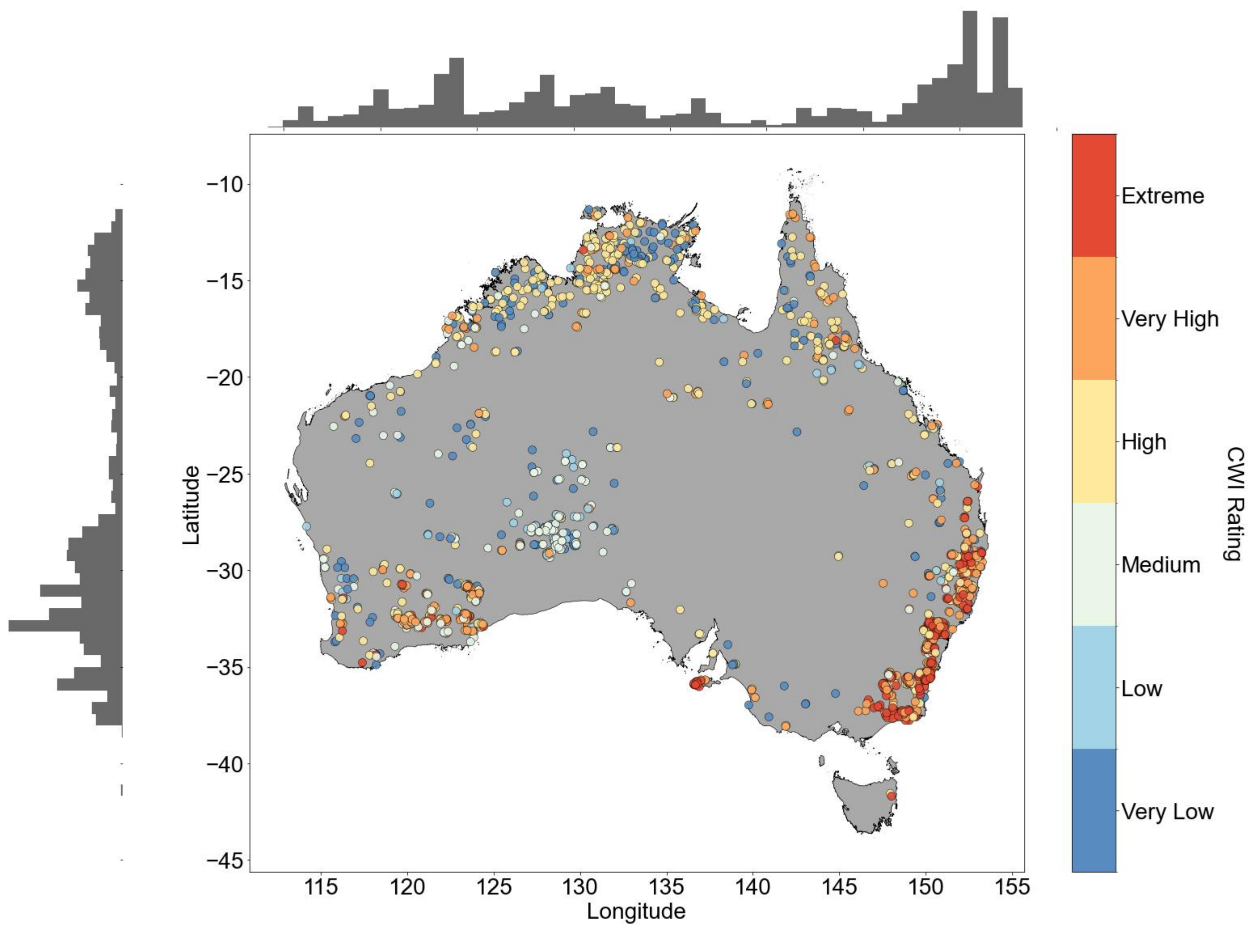

Figure 5.8 CWI rating map of Australia for the fires observed between April 2019 and March 2020. The histograms showcase the density of the hotspots along the longitude (top) and latitude (left).

5.3.5. Composite wildfire impact and state-issued severity ratings comparison

When the CWI ratings were compared to the matched state ratings for NSW and VIC (5.2.3), they showed moderate agreement, with a Spearman's R of 0.46 (Table 5.6). The PCA clustering exhibited a slightly stronger correlation with the state ratings with a Spearman's R of 0.52. Kendall's τ also indicated a moderate association between the two groups of ratings, with PCA being the closest to the state ratings (0.44), while the NoDR clustering was the least associated (0.36). The total number of fire events situated within NSW and VIC were 580, and all statistics presented were statistically significant ($p < 0.01$).

Table 5.6 Comparison of the harmonised VIC and NSW state burn severity ratings to the composite wildfire impact rating from all dimensionality reduction and clustering techniques presented in this study. As the CWI and severity ratings are ordinal data, two rank correlation metrics are presented, namely Spearman's R and Kendall's τ. All p-values from the coefficient calculations are below 0.01 and therefore the statistics are significant. The statistics correspond to 580 fire events situated within NSW and VIC.

	Spearman's R	Kendall's τ
NoDR	0.43	0.36
PCA	0.52	0.44
t-SNE	0.47	0.40
UMAP	0.48	0.42
PaCMAP	0.46	0.40
Consensus	0.46	0.40

5.4.Discussion

This study demonstrated how near-continuous active fire information from geostationary satellites can complement current methods based on pre- and post-fire normalised spectral differencing, advancing our understanding of wildfire impact on a continental scale. By combining and aligning two cohorts of wildfire metrics from Himawari-8 and Sentinel-2 into a single dataset, this approach builds and expands on ideas from fire regime characterization studies (Fernández-Guisuraga et al., 2023b; Zubkova et al., 2022). The fire intensity and spectral differencing dataset was transformed and clustered into six distinct wildfire impact categories, often aligned with specific dominant land cover types. The association between the proposed wildfire impact ratings and state-issued burn severity ratings, which rely exclusively on normalised spectral differencing, was moderate. This suggests that the two rating systems capture somewhat different dimensions of wildfire impact, highlighting potential limitations in both approaches. The moderate correlation implies that integrating active fire metrics from geostationary satellites may provide complementary insights not fully captured by traditional spectral-based severity methods alone.

Traditional and state-of-the-art dimensionality reduction techniques were used to transform the fire intensity and spectral differencing dataset into a space where fire hotspot similarities could be more effectively modelled through clustering. The different DRC techniques produced similar but not identical results, with similarity scores ranging from 65% to 73%. Therefore, ensemble clustering was employed to amplify shared patterns and retain diverse information. However, PCA, rather than the ensemble approach, aligned more closely with the ground truth when compared to the state-issued burn severity ratings from VIC and NSW. This was expected, as the first principal component (PC), which accounted for 45% of the dataset's variance, was influenced primarily by the Sentinel-2 NBR just as the state ratings did.

While the ensemble method was sufficiently close to the ground truth (NSW and VIC burn severity ratings) to boost confidence in its results, it differed enough to warrant rethinking wildfire impact assessments by integrating this new perspective. Nonetheless, UMAP could be a promising candidate for a simplified, single-model approach, as it had the highest average similarity with the other models and was positioned between PCA and the consensus clustering in terms of performance (Table 5.3). Thus, future studies should consider using UMAP to streamline their methodology and reduce the need for multiple complex models.

The interpretation of the CWI clustering results can be further developed by combining the information from Figure 5.6 (variable distribution per cluster) and Table 5.4 (land cover types per cluster) into a qualitative description of each cluster. For example, clusters with denser vegetation and potentially higher biomass availability demonstrated high fire intensity metrics, accompanied by equally high $dNBR_{\mu}$ and FFC (C3, C5). However, even when fire intensity metrics were low in forested areas, the impact was significant based on the normalised spectral differencing information (C1). Meanwhile, areas with mostly grassland and shrubland fires and potentially lower biomass, demonstrate lower $dNBR_{\mu}$ and NBR_{pre} values, and patchier fires (C2 and C9), even when fire intensity increased (C6). Finally, areas with medium biomass availability were the most variable but included consistently shorter fires, higher $dNBR_{\mu}$ and higher FFC than the global medians. Having these additional dimensions of information when describing fire could potentially be helpful when trying to assess the effects on ecosystem functioning, especially when multi-year periods are examined (Marcos et al., 2021).

In this study, composite wildfire impact refers to the composite effects of wildfires on vegetation, ecosystems, and the landscape, as quantified by remotely sensed fire intensity and spectral differencing metrics. It encompasses the immediate physical intensity of the fire using FRP metrics, fire duration, pre-fire vegetation health indicators, burned area patchiness (fire fractional cover), and subsequent vegetation damage measured by NBR metrics. Although the proposed impact ratings currently lack a clearly defined ground truth, we offer a conceptual definition for each rating as a first step, based on interpreting the variable distributions within each cluster and within the limits of our dataset (Table 5.7). We recognise that the CWI ratings follow a similar trend to spectral-differencing burn severity, with nuanced differences within each category, distinguishing hotter fires from cooler fires, shorter from longer durations, and fragmented from wall-to-wall burns, occurring in areas with varying vegetation condition. The impact ratings are also biased towards denser vegetation, with forests occupying the upper range of ratings and grasslands the lower.

Table 5.7 Conceptual description of the different composite wildfire impact ratings based on the median and variable distributions of the clusters used in this study. The dominant land cover classes are also presented.

CWI Rating	Intensity	Duration	Severity	Fire Fractional Cover	Pre-fire vegetation	LULC Majority	Cluster
Extreme (a)	Hotter	Long	High	Any	Any	Forests	3
Extreme (b)	Hotter	Any	High	Wall-to-wall	Healthy	Forests	5
Very High (a)	Hotter	Short	High	Wall-to-wall	Not healthy	Woodlands	8
Very High (b)	Cooler	Long	High	Any	Healthy	Forests	1
High (a)	Hotter	Short	High	Wall-to-wall	Not healthy	Woodlands	7
High (b)	Cooler	Long	High	Wall-to-wall	Healthy	Mixed	4
Medium	Hotter	Short	Low	Patchy	Not healthy	Grasslands	6
Low	Cooler	Long	Low	Patchy	Not healthy	Grasslands	2
Very Low	Cooler	Short	Low	Patchy	Not healthy	Grasslands	9

Examining the spatial distribution of CWI ratings across Australia reveals familiar patterns of the 2019-2020 fire season. Most extreme and very high impact ratings overlap with the southeastern Australian forests and the Black Sumer fires, which were one of the most extreme wildfires on record in Australia (Collins et al., 2021; Levin et al., 2021; Rumpff et al., 2023). Extreme ratings are also found on Kangaroo Island off the coast of South Australia, where nearly half of its area was burned during the 2019-2020 fire season (Bonney et al., 2020). Another notable cluster of high impact rating is observed in the southwest, particularly in the southern portion of the Great Western Woodlands, where younger woodlands prevail due to frequent fires over recent decades (Jucker et al., 2023). The medium impact cluster in the south-central part of Australia is the lowest impact cluster with a consistent spatial pattern, and it corresponds to shrublands and sparse vegetation based on the 2015 land cover map by Lymburner et al. (2015) and is in line with Table 5.5 (CWI rating mode per land cover). Lastly, the tropical savannahs of northern Australia are a distinct and recurring fire zone (Maier and Russell-Smith, 2012; Oliveira et al., 2015), with 2019-2020 likely experiencing intense fire weather conditions influenced by the preceding year's El Niño-Southern Oscillation (Bui et al., 2024).

In line with findings from other studies (Gale and Cary, 2022; Lee et al., 2024), pre-fire vegetation height and density, broadly represented by the pre-fire NBR and the land cover layer in our study, had an influence on severity (dNBR) and impact (CWI). Areas with taller, denser vegetation and higher pre-fire

NBR (e.g., forests) exhibited the highest dNBR values within the extreme impact clusters, while grasslands and shrublands demonstrated the lowest severity and CWI ratings. However, this may be partially an artefact of the extremity of the 2019-2020 fire season, which disproportionally affected the forested regions of southeastern Australia. Other sources of uncertainty in the CWI ratings arise from the influence of post-fire surface residues, such as ash and char, on dNBR values independently of vegetation impact. These reflectance effects follow a non-linear pattern with increasing fire intensity and duration, with char initially reducing surface reflectance, and white ash at higher intensities increasing it again (Roy et al., 2010; Smith et al., 2005). This may distort the interpretation of dNBR and it could be a consideration for future work. Moreover, the length of the study period, which does not account for intra-seasonal variations, as well as the spatial constraints of this study would require further investigation to replicate to other areas of the world. Repeating this methodology with data from different years and regions could provide a deeper understanding of how weather, seasonal and geographical variations influence wildfire impact. Additionally, incorporating biomass availability, fuel structure and condition data could allow for a more robust interpretation of the wildfire impact differences across land cover types. Future research should focus on refining the ground truth definition of composite wildfire impact and could benefit from incorporating validation sources not limited to pre- and post-fire spectral differencing assessments. Furthermore, the binary flag attribution based on the cluster and global variable median comparison (5.2.4.4) could be improved by developing more nuanced fuzzy rules for variable ranges and thresholds and adjusting the ordinal labels to better reflect wildfire impact in collaboration with fire ecology experts or local authorities.

5.5. Conclusions

This study presents a novel conceptual framework for assessing wildfire impact by integrating near-continuous active fire data from Himawari-8 (BRIGHT/AHI) with normalised spectral differencing information from Sentinel-2. Combining these two cohorts of independent metrics that describe different aspects of fire behaviour and activity can offer a more comprehensive view of wildfire effects on vegetation, ecosystems, and the landscape. Our approach expands on traditional pre- and post-fire burn severity assessments, capturing factors such as fire duration, burned area patchiness and pre-fire vegetation conditions. Future research should further refine the conceptual definition of wildfire impact, incorporating feedback from fire ecology experts and using additional validation sources. This framework offers a promising path for improving the characterisation of wildfire effects, particularly as climate variability increasingly shapes fire behaviour and impacts ecosystems. Expanding this methodology across different regions and timeframes can enhance our understanding of wildfire dynamics and contribute to more effective fire management strategies.

Chapter 6. Summary and Synthesis

This chapter concludes this dissertation's work by discussing and connecting key findings of the research objectives set in the introduction. It also situates the findings within the current body of knowledge, and discusses the implications, as well as future research avenues. In addition, it outlines the steps needed to progress this research into an operational global framework for wildfire impact characterisation.

6.1. Summary

This dissertation explored the utility of geostationary (GEO) active fire observations, available with a significantly higher temporal frequency than equivalent polar orbiting products, for better-informed wildfire impact characterisation. The suitability of geostationary sensors, particularly AHI, was first assessed and a conceptual framework that utilises this information in conjunction with burn severity Sentinel-2 data was proposed. The research aim was divided into four research questions corresponding to chapters 2 through 5. The main findings and implications of each research question are presented below.

<u>Research Question 1</u>: How do measures of fire radiative power from geostationary satellites compare with those from polar-orbiting satellites for an extreme wildfire event?

During the 2019–2020 southern hemisphere summer, south-eastern Australia faced extreme fire weather conditions, including prolonged drought and record high temperatures, which led to dry fuel accumulation and the catastrophic Black Summer Fires (Fryirs et al., 2021). Studying such events enables insights to be derived within these extreme conditions. This is important as extreme wildfires are becoming more frequent and having devastating consequences (Godfree et al., 2021; Wintle et al., 2020). The first research question assessed the Fire Radiative Power (FRP) estimation capabilities of Himawari-8 AHI compared to the established AQUA/TERRA MODIS data (Giglio et al., 2021). AHI data processed with the BRIGHT/AHI active fire detection algorithm (Engel et al., 2022, 2021b, 2021a) and the FRP model developed by Wooster et al. (2005, 2003) were compared to equivalent FRP estimations from MODIS (MOD14/MYD14). The intercomparison focused on concurrent and overlapping hotspot FRP estimations, and fire superclusters representing temporally and spatially continuous events. Additionally, the complete diurnal FRP cycles were compared between the two products for the entire region, in different seasonal settings, and biogeographically uniform subregions, providing a more independent perspective on the strengths and limitations of these products during extreme fire events.

The results revealed a strong correlation between the concurrent and overlapping hotspots of the BRIGHT/AHI and MOD14/MYD14 products (Pearson's r = 0.74), with a constant FRP underestimation from BRIGHT/AHI due to AHI's MIR channel saturation at 400K (Hall et al., 2019). Within the extent of fire superclusters, comparing the integrated FRP of only concurrent hotspots between BRIGHT/AHI and MOD14/MYD14 shows a moderate correlation (r = 0.49), while the correlation increases to 0.67 when all the detected BRIGHT/AHI hotspots are included. Additionally, both products capture similar spatio-temporal spread patterns, yet BRIGHT/AHI significantly outperforms MOD14/MYD14 when comparing complete FRP records. The higher temporal resolution of BRIGHT/AHI highlights diurnal cycle variations, consistently capturing maximum and minimum FRP periods throughout the day, unlike MOD14/MYD14, which lacks such temporal continuity.

The findings of Chapter 2 established the relative confidence and utility of BRIGHT/AHI to monitor spatial and temporal fire intensity patterns during extreme wildfires via satellite observations. This study also sets the stage for broader testing of BRIGHT/AHI FRP across Australia over a year of fire activity, covered in Research Question 2.

Research Question 2: How do measures of fire radiative power from geostationary satellites compare with those from polar-orbiting satellites when examining an entire year of wildfire activity, for the whole of Australia to capture seasonal and geographical variations?

The second research question expanded on the work conducted in the first research question by intercomparing GEO FRP estimations of the BRIGHT/AHI with equivalent polar-orbiting products from AQUA/TERRA MODIS (MOD14/MYD14) and SNPP VIIRS (VNP14IMG) (Schroeder and Giglio, 2018). The study assessed the effect of different land covers, seasons, and fire regimes on the BRIGHT/AHI FRP estimations. Thus, it was conducted for fires across Australia between April 2019 and March 2020.

When compared, BRIGHT/AHI and the established low-earth polar orbiting (LEO) products, MOD14/MYD14 and VNP14IMG, captured similar hotspot density and fire spread patterns across Australia. Strong correlations (r = 0.74-0.77) were observed between concurrent active fire hotspots from the GEO and LEO products, although with the known underestimation of FRP by BRIGHT/AHI caused by the saturation of the MIR channel of AHI (Hall et al., 2019). On a regional and land cover level, BRIGHT/AHI captured similar FRP descriptive statistics to MODIS, while the higher spatial resolution (375m) and sensitivity of VIIRS to smaller fires resulted in a broader range of FRP values.

BRIGHT/AHI's continuous observations provided detailed insights into diurnal fire activity, unlike LEO sensors, which often missed key periods of fire activity due to their limited temporal coverage. These findings were consistent across different fire seasons and climatic regions (northern and southern Australia). The seasonal average diurnal FRP cycle analysis further emphasised the completeness of the BRIGHT/AHI FRP record, in contrast to the LEO products that entirely missed the low fire activity time during the early morning hours. Such information provides valuable insights that can assist with fire suppression efforts and management. Additionally, after a temporal analysis of wildfires in four example subregions (0.2^o by 0.2^o), BRIGHT/AHI and VNP14IMG showed stronger agreement in capturing the temporal FRP patterns compared to MODIS, which missed a significant portion of peak fire activity.

Results from Research Question 2 highlight the temporal resolution advantage of BRIGHT/AHI, further increasing the confidence in its ability to characterise fire activity. BRIGHT/AHI data allowed for better reconstruction of fire activity over time, particularly during rapid fluctuations in fire intensity, which are critical for fire management and response efforts.

Research Question 3: What is the relationship between different earth observation measures of fire intensity (i.e., active fire) and burn severity (i.e., impact of fire)?

For the third research question, commonly used burn severity metrics, i.e., the Normalised Burn Ratio (NBR) and the differenced NBR before and after a fire (dNBR), were compared to GEO (BRIGHT/AHI) FRP metrics, based on the hypothesis that these two cohorts of metrics of wildfire behaviour would be expected to correlate. To date, the association between spectral differencing and FRP derived fire metrics have not received much attention in the literature. Furthermore, no studies have examined GEO data, which provide a superior temporal FRP record (as seen in Chapters 2 and 3). The study was conducted over Australia for a year of fire activity (2019-2020), similar to that used in Chapter 3, enabling the comparison of BRIGHT/AHI FRP to AHI dNBR and Sentinel-2 dNBR over various fire types, biogeographical regions, and land covers.

The correlations between FRP metrics and dNBR across biogeographically homogeneous regions were generally low. The Fire Radiative Energy (FRE), which corresponds to the time-integrated FRP of a pixel-area fire, showed a moderate agreement with dNBR in certain bioregions, particularly along Australia's east and north coasts ($r = 0.4$-0.59). Meanwhile, the Maximum FRP of a fire pixel (MaxFRP) and FRE performed similarly in southwest Australia, with only one region demonstrating a strong correlation ($r = 0.63$-0.66).

In extreme events such as the Black Summer Fires of 2019-2020, which represented the majority of hotter fires, neither FRP metric correlated well with dNBR. This suggests that FRP and dNBR metrics capture different aspects of fire activity in extreme weather and complex vegetation conditions (forests). Meanwhile, a higher agreement between FRP metrics and dNBR was observed in northern regions, where wildfires burned at cooler temperatures and across simpler structure vegetation (savannah grasslands and woodlands).

The correlations at the hotspot level were also weak, with a marginal increase for the hotter fires. The correlations were stronger when the Sentinel-2 dNBR was used instead of the AHI dNBR, suggesting that AHI dNBR was compromised by its significantly lower spatial resolution as compared to Sentinel-2 and the fact that dNBR calculation is not as time-sensitive to justify its usage. The fire fractional cover (FFC), or the percentage of the AHI pixel classified as burned using a dNBR threshold value based on fire type was computed and used to stratify the analysis into less and more burned AHI pixels. Although this approach significantly increased the FRP-dNBR correlations, fire-type-specific dNBR thresholds for burnt area classifications introduce a bias between hotter and cooler fires. As such, hotter and cooler fires with the same dNBR would be classified into different FFC groups and always have a gradient between their dNBR values, forcing the correlations to rise.

This Research Question (detailed in Chapter 5) reveals the diversity in wildfire information that can be extracted by different LEO and GEO metrics. Traditionally, burn severity metrics, such as NBR, have been used to assess wildfire effects on vegetation in conjunction with *in-situ* severity assessments (De Santis and Chuvieco, 2009; Gerrevink and Veraverbeke, 2021; Key and Benson, 2006). Meanwhile, active fire metrics describe active fire intensity that has been linked to a variety of fire effects on the vegetation, e.g., tree growth alterations and mortality (Smith et al., 2017; Sparks et al., 2023a, 2018, 2017; Subasinghe Achchige et al., 2022), and atmosphere, through emissions (Ichoku and Ellison, 2014; Li et al., 2022; Nguyen et al., 2023). The lack of correlation between the two groups of metrics suggests that an opportunity exists in combining the two to better understand fire effects.

Research Question 4: How can cross-platform fire intensity and severity measures be used to derive new metrics of wildfire characterization and impact in the landscape?

Burn severity and active fire metrics each have their own distinct advantages and limitations as explored in Research Question 3. Research Question 4 extends this work by proposing the combination of these two cohorts of metrics into a new, comprehensive fire impact rating. A conceptual framework that integrates the independent wildfire-relevant metrics studied in chapters 2-4, using an unsupervised dimensionality reduction and clustering (DRC) method is presented. As explained in section 5.2.4.1, dimensionality reduction was applied prior to clustering to reduce noise, and improve the performance of the chose distance-based clustering. A new rating was derived for the Australian continent for one year of fire activity (2019-2020) and then compared with local state burn severity assessments from Victoria (VIC) and New South Wales (NSW). This new rating is named Composite Wildfire Impact (CWI) and it represents the composite effects on vegetation, ecosystems and the landscape as observed by remotely sensed spectral changes and the release of energy from burning biomass.

The BRIGHT/AHI variables (MaxFRP, FRE, Duration) were combined with Sentinel-2 variables (dNBR, FFC, pre-fire NBR) into a single dataset. Exploratory data analysis revealed weak and non-linear correlations between the active fire and spectral differencing variables, prompting the use of DRC methods to identify clusters of similar fires. Namely, PCA and state-of-the-art non-linear methods (i.e., t-SNE, UMAP, PaCMAP) were employed alongside hierarchical clustering to group similar fire types. While the clustering outputs of each DRC method showed moderate similarities (65-73%) with one another, the absence of validation data prevented us from drawing firm conclusions about the actual fire impacts they represented. As a result, an ensemble clustering approach was used to aggregate results that preserves commonalities but also retains some divergent information.

Each ensemble cluster's variables were compared against global statistics, with clusters classified based on the central tendency of their variables. Fires in clusters with higher values were labelled as having a higher CWI rating. Key findings show that the most impactful fires during the study period were concentrated in southeastern Australia, Kangaroo Island, and the Great Western Woodlands, aligning with known extreme wildfires and fire-prone regions. The CWI rating showed a moderate agreement with VIC and NSW state fire management assessments, which are based on aerial photo interpretation and a random forest classification of dNBR values. These results indicate the confidence in the proposed methodology and its capacity to capture diverse fire-related information that is not always described by spectral differencing techniques alone.

The findings of Chapter 5 contribute to the broader understanding of wildfire dynamics in Australia, with global application opportunities. Near-continuous geostationary active fire data in conjunction with traditional spectral differencing indices can enhance post-fire impact assessments and help to understand ecological processes of recovery, offering a comprehensive approach to wildfire characterization and its impacts.

6.2.Synthesis

This thesis challenges the paradigm of assessing wildfire impact based only on spectral differencing methods. Remotely sensed spectral differencing measurements of burn severity, such as the Normalise Burn Ratio (NBR), often lack generalisability and can be prone to errors due to inconsistencies in vegetation type and structure, fuel moisture, fire history (Fernández-Guisuraga et al., 2023a; Gale and Cary, 2022; Gibson et al., 2020; Miller et al., 2023; Parker et al., 2015; Saberi and Harvey, 2023). We have shown that Fire Radiative Power (FRP) metrics can be reliably estimated with high-temporal-resolution geostationary satellite sensors, offering critical advantages for modelling active wildfire behaviour dynamics. Furthermore, these FRP metrics were found to not correlate with NBR-based metrics across varied

Australian ecosystems – ranging from dry savannas and rainforests in the north to temperate and alpine forests in the south. These findings presented an opportunity for proposing a novel conceptual framework that integrates multi-sensor earth observations active fire and burn severity metrics to describe the impact of wildfires on vegetation, ecosystems, and landscapes.

6.2.1. Limitations

While the work conducted in this dissertation from 2020 to 2024 provides novel insights, several limitations must be acknowledged. The selected 12-month study period captured seasonal variation in fire activity at a continental scale, but it coincided with an extreme fire season in southeastern Australia. This likely skewed the dataset towards higher intensity fires. Using a longer study period with fire seasons of varying intensity could alleviate the current bias towards extreme events and reveal more transferable insights between the fire seasons.

Secondly, FRP metrics derived from geostationary thresholds have inherent limitations compared to equivalent LEO sensors, primarily based on their coarser spatial resolution. These include biases due to sensor saturation during very intense fires, underestimation of energy release from smaller or lower-temperature fires, and detection thresholds influenced by satellite view angle and atmospheric conditions (Freeborn et al., 2014b; Hall et al., 2019; Roberts et al., 2015).

Thirdly, spectral severity indices such as the differenced Normalized Burn Ratio (dNBR) have known constraints. These metrics are often hard to correlate with *in-situ* measurements of severity and generalise over large areas (Fernández-Guisuraga et al., 2023a; French et al., 2008; Gale and Cary, 2022), while their signal can be affected by processes not related too wildfire effects (Roy et al., 2010, 2006; Smith et al., 2005).

In the absence of an established wildfire impact definition in the literature, we proposed a new conceptual definition focused on the combined effects of fire on vegetation, ecosystems, and landscapes, quantified through remotely sensed fire intensity (FRP) and burn severity (NBR) metrics. However, incorporating ground truth measurements and additional ecological metrics in future studies would further enhance accuracy, reliability, and ecological relevance.

6.2.2. Proposing a conceptual framework for wildfire impact

Here, we propose a novel conceptual framework for assessing wildfire impact on a large scale using available earth observations. This framework combines geostationary estimations of active fire intensity, available in high temporal frequency, with high spatial resolution spectral differencing metrics that quantify the effects of wildfires on surface reflectance. We know that these two sources of information offer different insights on wildfire effects (Chatzopoulos-Vouzoglanis et al., 2024), alluding to possible benefits stemming from their combination. Furthermore, wildfire risk, behaviour, and effects are heavily dependent on variables such as weather, climate, pre-fire vegetation condition, density, and structure (Fernández-Guisuraga et al., 2021; Gale et al., 2023; Jucker et al., 2023; Lin et al., 2024). While our Composite Wildfire Impact rating utilises pre-fire reflectance information in the form of NBR as a proxy of pre-fire vegetation condition; fuel structure and available biomass cannot be accurately captured by pre-fire reflectance, especially in denser canopies (Gale et al., 2021). Therefore, this conceptual framework could be expanded using other available sources of information about wildfire drivers and effects (Figure 6.1), which can contribute to new holistic ways to measure, map, and record wildfire impact.

Figure 6.1 illustrates the conceptual framework for wildfire impact characterisation proposed in this dissertation. It combines remotely sensed information of pre-, during, and post-fire attributes with wildfire drivers. The incorporation of fuel condition before the fire, biomass availability and change due to fire, fire history, local fire weather and broad climatic drivers can expand each of the concepts surrounding wildfire impact and greatly enhance the proposed wildfire impact metric.

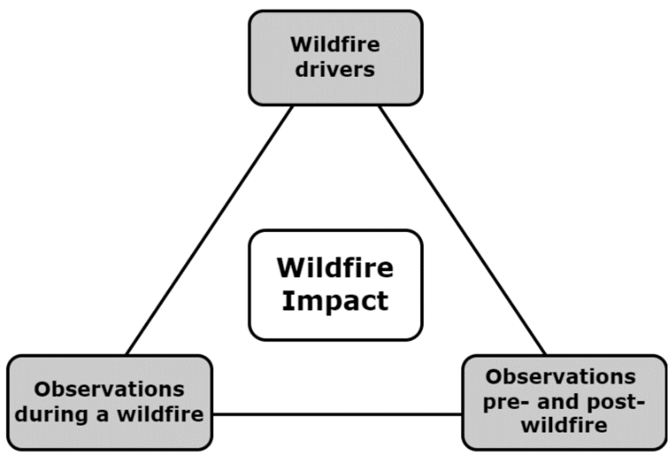

Figure 6.1 Concept of a wildfire impact assessment framework. The framework combines various information sources that affect wildfire behaviour pre-, post- and during the wildfire. It also incorporates wildfire drivers that can affect wildfire impact substantially.

Active remote sensing sensors, such as LiDAR and Synthetic Aperture Radar (SAR), can measure variables describing fuel and biomass attributes and improve the composite wildfire impact concept. In particular, airborne LiDAR estimates of understory fuel have been linked to burn severity (Gale et al., 2023), while spaceborne LiDAR, such as the Global Ecosystem Dynamics Investigation LiDAR (GEDI), have been used for above ground biomass estimation (Dubayah et al., 2020; Silva et al., 2021). Meanwhile, many studies have experimented with C- and X-band SAR from the current satellite missions (e.g. Sentinel-1, TerraSAR/TanDEM-X) to detect and model biomass changes (Qi et al., 2019; Santoro et al., 2022). However, the available C- and X-band SAR sensors do not penetrate the canopy due to their small wavelength (Ji et al., 2024). This will improve with future satellite missions, such as ESA's BIOMASS and NASA's NISAR, which will include polarimetric P- and L-band SAR systems that can penetrate the different canopy layers and deliver better biomass indicators (NISAR, 2018; Quegan et al., 2019). Additionally, repeating such measurements before and after a fire can be used to derive biomass consumption rates whose uncertainty is often an issue in biomass burning emissions studies (Li et al., 2018b; Nguyen et al., 2023; Wooster et al., 2021). Accurate measures of biomass and biomass consumption can also improve the calculation and validation of the CWI rating, by creating an association between active fire and burn severity metrics to biomass change.

Fire history is another variable to consider when assessing wildfire impact, as it affects the fuel availability and how well the ecosystem can bounce back (Dixon et al., 2023; Tortorelli et al., 2024). This information can be particularly useful in the case of short-interval reburns, where the burn severity is often over- or underestimated by CBI and NBR-based indices based on past severity (Saberi and Harvey, 2023). High-frequency and high-confidence geostationary FRP information could help assess wildfire effects when field and spectral differencing information fail to capture the whole picture in the case of short reburns. Meanwhile, fire history layers can become more comprehensive by integrating the record of fire intensity or wildfire impact and improve our understanding of the compounding fire effects on future vegetation distributions, risks, and fire regimes.

Multi-year cycles of variability in local sea surface temperatures and atmospheric pressure have been linked to the extremity of fire seasons worldwide. These periodic phenomena are called climate teleconnections (CTs), and they have been associated with fluctuations in wildfire-relevant variables, such as biomass accumulation, fuel moisture, soil evapotranspiration, burned area and fire weather (Cardil et al., 2023). For instance, the Australian 2019/2020 fire season was heavily influenced by the Indian Ocean Dipole (IOD) and the El-Niño Southern Oscillation (ENSO) CTs in the preceding two years, which led to unprecedented droughts (Wang and Cai, 2020). With wildfire activity intensifying under climate change globally (Jain et al., 2024; Jones et al., 2024; Mariani et al., 2018; Richardson et al., 2022), monitoring the potential feedback loops created between climate and wildfires (Liu et al., 2019) can assist in forecasting the impact of fire seasons and even the magnitudes of FRP and FRE. A few studies have already experimented with the latter using machine learning models trained on fuel, topography, population density, vegetation indices and weather variables; however, these models still have significant errors (Dong et al., 2024; Thapa et al., 2024). Meanwhile, certain wildfire attributes (i.e., duration, spread rate, size, intensity, impact), which can be captured effectively by GEO sensors as shown in this dissertation, have been linked to increasing land surface temperatures of burned areas (Zhao et al., 2024). Therefore, more effort is needed to assess climate effects on wildfires and vice-versa to assist with the adaptation of new climatic norms.

The proposed wildfire impact metric can benefit a variety of end users. Fire managers and ecologists currently assess biodiversity loss and ecosystem recovery trends using the extent and patchiness of high severity fires (Haslem et al., 2024). These assessments could be expanded to include fire intensity and emissions (Balch and Williams, 2024), and potentially impact, to better describe wildfire effects. Moreover, post-fire ecosystem recovery, tree mortality and emission studies could be enhanced by including the composite fire intensity and severity effects into their methodologies, on the basis that fire intensity and radiative heat have been shown to harm tree growth regardless of burn severity (Smith et al., 2017; Sparks et al., 2023a, 2018, 2017; Subasinghe Achchige et al., 2022), inevitably affecting carbon sequestration (Fairman et al., 2022b). We believe this dissertation can push for a paradigm shift in how we assess wildfire effects, towards a more holistic approach.

Figure 6.2 presents a flowchart illustrating the framework, distinguishing between wildfire drivers, remotely sensed indicators, and the resulting effects that contribute to wildfire impact. Drivers include long term climate change, with CTs being intertwined with local fire weather extremes that affect biomass and fuel conditions, as well as fire history. The remotely sensed information includes the variables used in this dissertation, which could be expanded to include biomass/fuel information extracted from LiDAR and SAR data. Finally, ecosystem responses, emissions, biomass loss and recovery could be used to interpret the composite impact of all the above. The dashed lines indicate this framework is also dynamic and can be expanded with the help of new and emerging information and technology.

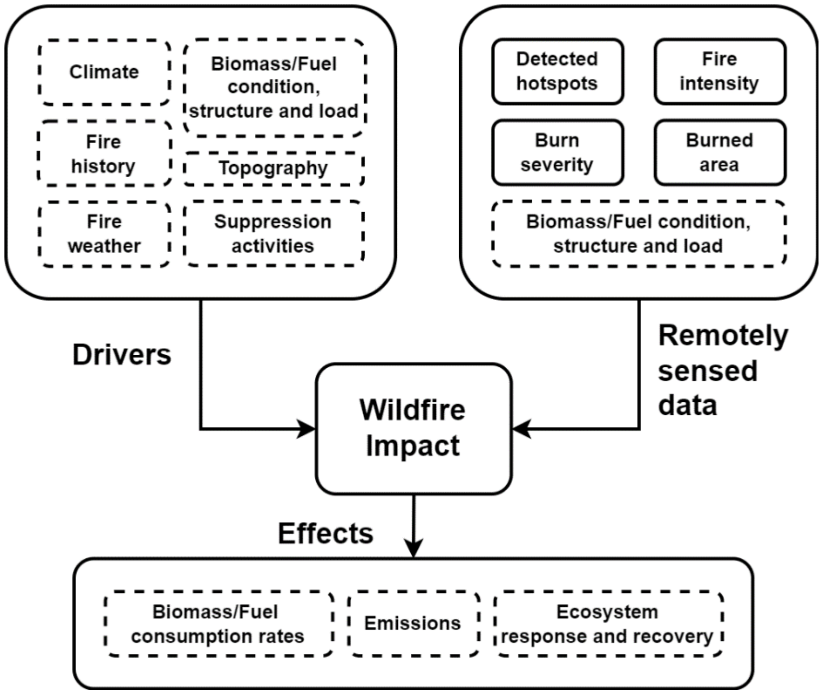

Figure 6.2 Implementation scheme of the proposed framework, along with the distinction between drivers, effects, and available remote sensing data around wildfire impact. The solid lines indicate the data and concepts used in this dissertation, while the dashed lines indicate additional parameters that can be incorporated.

Adopting this proposed framework for wildfire impact assessments could set the wildfire research community in a better position to holistically characterise the impacts of wildfires on a range of ecosystem services, enhancing our capacity to monitor, model, and mitigate these impacts on both a regional and global scale. By combining multi-sensor, active fire metrics with traditional spectral indices, this approach provides a nuanced view of ecosystem functioning, capturing both immediate fire dynamics as well as longer-term ecological responses and effects on the local and global climate. This framework can also inform adaptive management strategies and improve our understanding of ecosystem resilience and recovery processes, thus supporting informed policy and conservation efforts.

6.2.3. Technology outlook

The current generation of geostationary sensors consists of nearly identical instruments that make wildfire-relevant MIR observations (3.9μm) over the full earth's disk every 5-15 minutes at 2km covering different regions of the earth. Such instruments include the ABI (Advanced Baseline Imager) on board the GOES-R satellites over the Americas (Schmidt et al., 2020; Schmit et al., 2005), while over east Asia and Australia we have the AHI (Advanced Himawari Imager) of Himawari-8 and 9 (Bessho et al., 2016), the AMI (Advanced Meteorological Imager) of Geo-Kompsat-2A (Kim et al., 2021), and the AGRI (Advanced

Geosynchronous Radiation Imager) of Feng-Yun 4a and 4b (Yang et al., 2017). Another available GEO sensor is the SEVIRI (Spinning Enhanced Visible and Infrared Imager) onboard Meteosat's Second Generation (MSG) platform that provides geostationary wildfire observations over Europe and Africa at a lower spatial resolution of 3km (Wooster et al., 2015). In 2022, the European Space Agency (ESA) launched a satellite with the third generation of Meteosat's satellite imagers (MTG-I), which will offer two products in wildfire-relevant channels (3.8μm) at 1km and 2km spatial resolution (Holmlund et al., 2021), while a second satellite is scheduled to launch soon (Lekouara et al., 2024). These instruments and their predecessors are vital for meteorological as well as wildfire applications.

Meanwhile, future GEO missions are planned that aim to improve this legacy. The United States' National Oceanic and Atmospheric Administration (NOAA) has designed a new mission to substitute and improve the GOES-R record and provide the next generation of GEO observations for environmental monitoring from the early 2030s into the mid-2050s (Lindsey et al., 2024). This GEO constellation of two satellites is named Geostationary Extended Observations (GeoXO), and it will offer MIR observations at a 1km spatial resolution (Lindsey et al., 2024). This 2-fold improvement in ground sampling distance will benefit future fire detections and FRP estimations, bridging the gap between polar-orbiting fire detections (e.g., MODIS, VIIRS and Sentinel-3 SLSTR) and current generation GEO sensors, thus allowing for the detection of smaller and cooler burning fires (Lindsey et al., 2024). As the geostationary technology progresses and bridges the spatial resolution gap with the polar-orbiting sensors, wildfire variables that are linked to wildfire impacts on the wildland-urban interface, such as the daily fire growth rate (FGR) based on MODIS burned area data (Balch et al., 2024), will be available in much smaller intervals providing an additional lens for tracking and managing wildfires and their effects.

In parallel with geostationary missions, the remote sensing industry has started to invest in micro-satellite constellations (CubeSats) for wildfire monitoring. These constellations aim to reduce fire detection times through large member rates in their constellations, higher spatial resolution and on-board processing. However, there is evidence suggesting that their advertised spatial resolution is over-estimated by a few orders of magnitude compared to what they actual can sample on the ground (Valenzuela et al., 2024). In addition, most CubeSat missions for wildfire detection and monitoring are still at an early, sometimes even conceptual, stage and we will have to wait and see what this new technology has to offer. Notable examples are a philanthropic Google-backed activity named FireSat (Earth Fire Alliance, 2025), which aims to detect fires of 5x5m size and assist fire suppression efforts, University of South Australia's Kanyini satellite mission, which will be able to detect fire smoke (Lu et al., 2024), as well as Forest-2 of OroraTech (Schöttl et al., 2024). While these technological advancements are quite promising, we are cautious that the further commercialisation of information may push us away from the open-source data model followed by the large, centralised missions of national space agencies (NASA, ESA, JAXA etc.). We hope that through international collaboration and initiatives, these data can be used for the improvement of wildfire monitoring in a non-for-profit manner.

6.3. Conclusion

This research has combined active fire products with spectral differencing data used to assess burn severity and proposed a novel dynamic conceptual framework of wildfire impact. This framework is a foundational step in assessing the composite impacts of wildfire on vegetation, landscapes, and ecosystems at broader spatial scales, as these are captures by remote sensing data. It is hoped that the work completed in this dissertation will inspire and generate a new paradigm of wildfire impact products and research, which will be vital for adapting our understanding of ecosystem resilience and wildfire dynamics within the context of climate change.

References

Abatzoglou, J.T., Williams, A.P., Barbero, R., 2019. Global Emergence of Anthropogenic Climate Change in Fire Weather Indices. Geophysical Research Letters 46, 326–336. https://doi.org/10.1029/2018GL080959

Abram, N.J., Henley, B.J., Sen Gupta, A., Lippmann, T.J.R., Clarke, H., Dowdy, A.J., Sharples, J.J., Nolan, R.H., Zhang, T., Wooster, M.J., Wurtzel, J.B., Meissner, K.J., Pitman, A.J., Ukkola, A.M., Murphy, B.P., Tapper, N.J., Boer, M.M., 2021. Connections of climate change and variability to large and extreme forest fires in southeast Australia. Communications Earth & Environment 2. https://doi.org/10.1038/s43247-020-00065-8

Aggarwal, C.C., Hinneburg, A., Keim, D.A., 2001. On the Surprising Behavior of Distance Metrics in High Dimensional Space, in: Van Den Bussche, J., Vianu, V. (Eds.), Database Theory — ICDT 2001, Lecture Notes in Computer Science. Springer Berlin Heidelberg, Berlin, Heidelberg, pp. 420–434. https://doi.org/10.1007/3-540-44503-X_27

Agresti, A., 2019. An introduction to categorical data analysis, Third edition. ed, Wiley series in probability and statistics. John Wiley & Sons, Hoboken, NJ.

Andela, N., Kaiser, J.W., Van Der Werf, G.R., Wooster, M.J., 2015. New fire diurnal cycle characterizations to improve fire radiative energy assessments made from MODIS observations. Atmospheric Chemistry and Physics 15, 8831–8846. https://doi.org/10.5194/acp-15-8831-2015

Balch, J.K., Abatzoglou, J.T., Joseph, M.B., Koontz, M.J., Mahood, A.L., McGlinchy, J., Cattau, M.E., Williams, A.P., 2022. Warming weakens the night-time barrier to global fire. Nature 602, 442–448. https://doi.org/10.1038/s41586-021-04325-1

Balch, J.K., Iglesias, V., Mahood, A.L., Cook, M.C., Amaral, C., DeCastro, A., Leyk, S., McIntosh, T.L., Nagy, R.C., St. Denis, L., Tuff, T., Verleye, E., Williams, A.P., Kolden, C.A., 2024. The fastest-growing and most destructive fires in the US (2001 to 2020). Science 386, 425–431. https://doi.org/10.1126/science.adk5737

Balch, J.K., Williams, A.P., 2024. Extreme wildfire seasons loom — science can help us adapt. Nature 634, 1041–1044. https://doi.org/10.1038/d41586-024-03433-y

Becht, E., McInnes, L., Healy, J., Dutertre, C.-A., Kwok, I.W.H., Ng, L.G., Ginhoux, F., Newell, E.W., 2019. Dimensionality reduction for visualizing single-cell data using UMAP. Nat Biotechnol 37, 38–44. https://doi.org/10.1038/nbt.4314

Belkina, A.C., Ciccolella, C.O., Anno, R., Halpert, R., Spidlen, J., Snyder-Cappione, J.E., 2019. Automated optimized parameters for T-distributed stochastic neighbor embedding improve visualization and analysis of large datasets. Nat Commun 10, 5415. https://doi.org/10.1038/s41467-019-13055-y

Bessho, K., Date, K., Hayashi, M., Ikeda, A., Imai, T., Inoue, H., Kumagai, Y., Miyakawa, T., Murata, H., Ohno, T., Okuyama, A., Oyama, R., Sasaki, Y., Shimazu, Y., Shimoji, K., Sumida, Y., Suzuki, M., Taniguchi, H., Tsuchiyama, H., Uesawa, D., Yokota, H., Yoshida, R., 2016. An introduction to Himawari-8/9 — Japan's new-generation geostationary meteorological satellites. Journal of the Meteorological Society of Japan 94, 151–183. https://doi.org/10.2151/jmsj.2016-009

Bonney, M.T., He, Y., Myint, S.W., 2020. Contextualizing the 2019–20 kangaroo island bushfires: Quantifying landscape-level influences on past severity and recovery with landsat and google earth engine. Remote Sensing 12, 1–32. https://doi.org/10.3390/rs12233942

Bui, H.X., Li, Y.-X., Dommenget, D., 2024. Controlling factors of wildfires in Australia and their changes under global warming. Environ. Res. Lett. 19, 094030. https://doi.org/10.1088/1748-9326/ad69a9

Calheiros, T., Pereira, M.G., Nunes, J.P., 2021. Assessing impacts of future climate change on extreme fire weather and pyro-regions in Iberian Peninsula. Science of the Total Environment 754, 142233. https://doi.org/10.1016/j.scitotenv.2020.142233

Cardil, A., Rodrigues, M., Tapia, M., Barbero, R., Ramírez, J., Stoof, C.R., Silva, C.A., Mohan, M., de-Miguel, S., 2023. Climate teleconnections modulate global burned area. Nat Commun 14, 427. https://doi.org/10.1038/s41467-023-36052-8

Chatzopoulos-Vouzoglanis, K., Reinke, K.J., Soto-Berelov, M., Engel, C., Jones, S.D., 2022. Comparing geostationary and polar-orbiting satellite sensor estimates of Fire Radiative Power (FRP) during the Black Summer Fires (2019–2020) in south-eastern Australia. International Journal of Wildland Fire 31, 572–585. https://doi.org/10.1071/WF21144

Chatzopoulos-Vouzoglanis, K., Reinke, K.J., Soto-Berelov, M., Jones, S.D., 2024. Are fire intensity and burn severity associated? Advancing our understanding of FRP and NBR metrics from Himawari-8/9 and Sentinel-2. International Journal of Applied Earth Observation and Geoinformation 127, 103673. https://doi.org/10.1016/j.jag.2024.103673

Chatzopoulos-Vouzoglanis, K., Reinke, K.J., Soto-Berelov, M., Jones, S.D., 2023. One year of near-continuous fire monitoring on a continental scale: Comparing fire radiative power from polar-orbiting and geostationary observations. International Journal of Applied Earth Observation and Geoinformation 117, 103214. https://doi.org/10.1016/j.jag.2023.103214

Chen, J., Li, R., Tao, M., Wang, Lili, Lin, C., Wang, J., Wang, Lunche, Wang, Y., Chen, L., 2022. Overview of the performance of satellite fire products in China: Uncertainties and challenges. Atmospheric Environment 268, 118838. https://doi.org/10.1016/j.atmosenv.2021.118838

Chuvieco, E., Mouillot, F., Van Der Werf, G.R., San Miguel, J., Tanase, M., Koutsias, N., García, M., Yebra, M., Padilla, M., Gitas, I., Heil, A., Hawbaker, T.J., Giglio, L., 2019. Historical background and current developments for mapping burned area from satellite Earth observation. Remote Sensing of Environment 225, 45–64. https://doi.org/10.1016/j.rse.2019.02.013

Collins, L., Bradstock, R.A., Clarke, H., Clarke, M.F., Nolan, R.H., Penman, T.D., 2021. The 2019/2020 mega-fires exposed Australian ecosystems to an unprecedented extent of high-severity fire. Environ. Res. Lett. 16, 044029. https://doi.org/10.1088/1748-9326/abeb9e

Collins, L., Griffioen, P., Newell, G., Mellor, A., 2018. The utility of Random Forests for wildfire severity mapping. Remote Sensing of Environment 216, 374–384. https://doi.org/10.1016/j.rse.2018.07.005

Collins, L., McCarthy, G., Mellor, A., Newell, G., Smith, L., 2020. Training data requirements for fire severity mapping using Landsat imagery and random forest. Remote Sensing of Environment 245, 111839. https://doi.org/10.1016/j.rse.2020.111839

Cunningham, C.X., Williamson, G.J., Nolan, R.H., Teckentrup, L., Boer, M.M., Bowman, D.M.J.S., 2024. Pyrogeography in flux: Reorganization of Australian fire regimes in a hotter world. Global Change Biology 30, e17130. https://doi.org/10.1111/gcb.17130

DAWE, 2000. Revision of the Interim Biogeographic Regionalisation for Australia (IBRA) and Development of Version 5.1 - Summary report. Department of Agriculture, Water and the Environment, Australian Government, Canberra, Australia.

De Santis, A., Chuvieco, E., 2009. GeoCBI: A modified version of the Composite Burn Index for the initial assessment of the short-term burn severity from remotely sensed data. Remote Sensing of Environment 113, 554–562. https://doi.org/10.1016/j.rse.2008.10.011

Dixon, D.J., Duncan, J.M.A., Callow, J.N., Setterfield, S.A., Pauli, N., 2023. Fire reduces eucalypt forest flowering phenology at the landscape-scale. Science of The Total Environment 894, 164828. https://doi.org/10.1016/j.scitotenv.2023.164828

Dong, Z., Zheng, C., Zhao, F., Wang, G., Tian, Y., Li, H., 2024. A Deep Learning Framework: Predicting Fire Radiative Power From the Combination of Polar-Orbiting and Geostationary Satellite Data During Wildfire Spread. IEEE J. Sel. Top. Appl. Earth Observations Remote Sensing 17, 10827–10841. https://doi.org/10.1109/JSTARS.2024.3403146

Dozier, J., 1980. Satellite identification of surface radiant temperature fields of subpixel resolution (Planck function). 229.

Dubayah, R.O., Blair, J.B., Goetz, S.J., Fatoyinbo, L., Hansen, M.C., Healey, S.P., Hofton, M., Hurtt, G., Kellner, J.R., Luthcke, S., Armston, J., Tang, H., Duncanson, L., Hancock, S., Jantz, P., Marselis,

S., Patterson, P., Qi, W., Silva, C., 2020. GLOBAL Ecosystem Dynamics Investigation (GEDI) Level 02 User Guide. NASA EOSDIS Land Processes DAAC.
Earth Fire Alliance, 2025. FireSat [WWW Document]. URL https://www.earthfirealliance.org/ (accessed 4.22.25).
Engel, C.B., Jones, S.D., Reinke, K.J., 2022. Fire Radiative Power (FRP) Values for Biogeographical Region and Individual Geostationary HHMMSS Threshold (BRIGHT) Hotspots Derived from the Advanced Himawari Imager (AHI). Remote Sensing 14, 2540. https://doi.org/10.3390/rs14112540
Engel, C.B., Jones, S.D., Reinke, K.J., 2021a. Real-time detection of daytime and night-time fire hotspots from geostationary satellites. Remote Sensing 13. https://doi.org/10.3390/rs13091627
Engel, C.B., Jones, S.D., Reinke, K.J., 2021b. A Seasonal-Window Ensemble-Based Thresholding Technique Used to Detect Active Fires in Geostationary Remotely Sensed Data. IEEE Transactions on Geoscience and Remote Sensing 1–10. https://doi.org/10.1109/TGRS.2020.3018455
ESA, 2015. Sentinel-2 User Handbook. European Space Agency.
Fairman, T.A., Nitschke, C.R., Bennett, L.T., 2022a. Carbon stocks and stability are diminished by short-interval wildfires in fire-tolerant eucalypt forests. Forest Ecology and Management 505, 119919. https://doi.org/10.1016/j.foreco.2021.119919
Fairman, T.A., Nitschke, C.R., Bennett, L.T., 2022b. Carbon stocks and stability are diminished by short-interval wildfires in fire-tolerant eucalypt forests. Forest Ecology and Management 505, 119919. https://doi.org/10.1016/j.foreco.2021.119919
Fairman, T.A., Nitschke, C.R., Bennett, L.T., 2016. Too much, too soon? A review of the effects of increasing wildfire frequency on tree mortality and regeneration in temperate eucalypt forests. International Journal of Wildland Fire 25, 831–848. https://doi.org/10.1071/WF15010
FEER, 2021. MODFIRE Dataset [WWW Document]. Fire Energetics and Emissions Research, NASA. URL https://feer.gsfc.nasa.gov/data/frp/ (accessed 6.28.21).
Fensholt, R., Anyamba, A., Huber, S., Proud, S.R., Tucker, C.J., Small, J., Pak, E., Rasmussen, M.O., Sandholt, I., Shisanya, C., 2011. Analysing the advantages of high temporal resolution geostationary msg seviri data compared to polar operational environmental satellite data for land surface monitoring in Africa. International Journal of Applied Earth Observation and Geoinformation 13, 721–729. https://doi.org/10.1016/j.jag.2011.05.009
Fernández-García, V., Santamarta, M., Fernández-Manso, A., Quintano, C., Marcos, E., Calvo, L., 2018. Burn severity metrics in fire-prone pine ecosystems along a climatic gradient using Landsat imagery. Remote Sensing of Environment 206, 205–217. https://doi.org/10.1016/j.rse.2017.12.029
Fernández-Guisuraga, J.M., Fernandes, P.M., Marcos, E., Beltrán-Marcos, D., Sarricolea, P., Farris, M., Calvo, L., 2023a. Caution is needed across Mediterranean ecosystems when interpreting wall-to-wall fire severity estimates based on spectral indices. Forest Ecology and Management 546, 121383. https://doi.org/10.1016/j.foreco.2023.121383
Fernández-Guisuraga, J.M., Martins, S., Fernandes, P.M., 2023b. Characterization of biophysical contexts leading to severe wildfires in Portugal and their environmental controls. Science of The Total Environment 875, 162575. https://doi.org/10.1016/j.scitotenv.2023.162575
Fernández-Guisuraga, J.M., Suárez-Seoane, S., Fernandes, P.M., Fernández-García, V., Fernández-Manso, A., Quintano, C., Calvo, L., 2022. Pre-fire aboveground biomass, estimated from LiDAR, spectral and field inventory data, as a major driver of burn severity in maritime pine (Pinus pinaster) ecosystems. Forest Ecosystems 9, 100022. https://doi.org/10.1016/j.fecs.2022.100022
Fernández-Guisuraga, J.M., Suárez-Seoane, S., García-Llamas, P., Calvo, L., 2021. Vegetation structure parameters determine high burn severity likelihood in different ecosystem types: A case study in a burned Mediterranean landscape. Journal of Environmental Management 288, 112462. https://doi.org/10.1016/j.jenvman.2021.112462
Filkov, A.I., Ngo, T., Matthews, S., Telfer, S., Penman, T.D., 2020. Impact of Australia's catastrophic 2019/20 bushfire season on communities and environment. Retrospective analysis and current trends. Journal of Safety Science and Resilience 1, 44–56. https://doi.org/10.1016/j.jnlssr.2020.06.009

Finco, M., Quayle, B., Zhang, Y., Lecker, J., Megown, K.A., Kenneth Brewer, C., 2012. Monitoring Trends and Burn Severity (MTBS): Monitoring wildfire activity for the past quarter century using landsat data. Presented at the Moving from Status to Trends: Forest Inventory and Analysis Symposium 2012.

Fred, A.L.N., Jain, A.K., 2005. Combining multiple clusterings using evidence accumulation. IEEE Trans. Pattern Anal. Mach. Intell. 27, 835–850. https://doi.org/10.1109/TPAMI.2005.113

Freeborn, P.H., Jolly, W.M., Cochrane, M.A., Roberts, G., 2022. Large wildfire driven increases in nighttime fire activity observed across CONUS from 2003–2020. Remote Sensing of Environment 268, 112777. https://doi.org/10.1016/j.rse.2021.112777

Freeborn, P.H., Wooster, M.J., Roberts, G., Malamud, B.D., Xu, W., 2009. Development of a virtual active fire product for Africa through a synthesis of geostationary and polar orbiting satellite data. Remote Sensing of Environment 113, 1700–1711. https://doi.org/10.1016/j.rse.2009.03.013

Freeborn, P.H., Wooster, M.J., Roberts, G., Xu, W., 2014a. Evaluating the SEVIRI fire thermal anomaly detection algorithm across the Central African Republic using the MODIS active fire product. Remote Sensing 6, 1890–1917. https://doi.org/10.3390/rs6031890

Freeborn, P.H., Wooster, M.J., Roy, D.P., Cochrane, M.A., 2014b. Quantification of MODIS fire radiative power (FRP) measurement uncertainty for use in satellite-based active fire characterization and biomass burning estimation. Geophysical Research Letters 41, 1988–1994. https://doi.org/10.1002/2013GL059086

French, N.H.F., Kasischke, E.S., Hall, R.J., Murphy, K.A., Verbyla, D.L., Hoy, E.E., Allen, J.L., 2008. Using Landsat data to assess fire and burn severity in the North American boreal forest region: an overview and summary of results. Int. J. Wildland Fire 17, 443. https://doi.org/10.1071/WF08007

Fryirs, K.A., Cowley, K.L., Hejl, N., Chariton, A., Christiansen, N., Dudaniec, R.Y., Farebrother, W., Hardwick, L., Ralph, T., Stow, A., Hose, G., 2021. Extent and effect of the 2019-20 Australian bushfires on upland peat swamps in the Blue Mountains, NSW. International Journal of Wildland Fire 30, 294. https://doi.org/10.1071/WF20081

Fu, Y., Li, R., Wang, X., Bergeron, Y., Valeria, O., Chavardès, R.D., Wang, Y., Hu, J., 2020. Fire detection and fire radiative power in forests and low-biomass lands in northeast Asia: MODIS versus VIIRS fire products. Remote Sensing 12, 1–20. https://doi.org/10.3390/rs12182870

Furniss, T.J., Kane, V.R., Larson, A.J., Lutz, J.A., 2020. Detecting tree mortality with Landsat-derived spectral indices: Improving ecological accuracy by examining uncertainty. Remote Sensing of Environment 237, 111497. https://doi.org/10.1016/j.rse.2019.111497

Gale, M.G., Cary, G.J., 2022. What determines variation in remotely sensed fire severity? Consideration of remote sensing limitations and confounding factors. International Journal of Wildland Fire 31, 291–305. https://doi.org/10.1071/WF21131

Gale, M.G., Cary, G.J., Van Dijk, A.I.J.M., Yebra, M., 2023. Untangling fuel, weather and management effects on fire severity: Insights from large-sample LiDAR remote sensing analysis of conditions preceding the 2019-20 Australian wildfires. Journal of Environmental Management 348, 119474. https://doi.org/10.1016/j.jenvman.2023.119474

Gale, M.G., Cary, G.J., Van Dijk, A.I.J.M., Yebra, M., 2021. Forest fire fuel through the lens of remote sensing: Review of approaches, challenges and future directions in the remote sensing of biotic determinants of fire behaviour. Remote Sensing of Environment 255, 112282. https://doi.org/10.1016/j.rse.2020.112282

Gale, M.G., Cary, G.J., Yebra, M., Leavesley, A.J., Van Dijk, A.I.J.M., 2022. Comparison of contrasting optical and LiDAR fire severity remote sensing methods in a heterogeneous forested landscape in south-eastern Australia. International Journal of Remote Sensing 43, 2559–2580. https://doi.org/10.1080/01431161.2022.2064197

Gerrevink, M.J.V., Veraverbeke, S., 2021. Evaluating the Near and Mid Infrared Bi-Spectral Space for Assessing Fire Severity and Comparison with the Differenced Normalized Burn Ratio. Remote Sensing 13, 695. https://doi.org/10.3390/rs13040695

Gibson, R., Danaher, T., Hehir, W., Collins, L., 2020. A remote sensing approach to mapping fire severity in south-eastern Australia using Sentinel 2 and random forest. Remote Sensing of Environment 240, 111702. https://doi.org/10.1016/j.rse.2020.111702

Giglio, L., Boschetti, L., Roy, D.P., Humber, M.L., Justice, C.O., 2018. The Collection 6 MODIS burned area mapping algorithm and product. Remote Sensing of Environment 217, 72–85. https://doi.org/10.1016/j.rse.2018.08.005

Giglio, L., Schroeder, W., Hall, J.V., Justice, C.O., 2021. MODIS Collection 6 and Collection 6.1 Active Fire Product User's Guide, Nasa.

Giglio, L., Schroeder, W., Justice, C.O., 2016. The collection 6 MODIS active fire detection algorithm and fire products. Remote Sensing of Environment 178, 31–41. https://doi.org/10.1016/j.rse.2016.02.054

Godfree, R.C., Knerr, N., Encinas-Viso, F., Albrecht, D., Bush, D., Christine Cargill, D., Clements, M., Gueidan, C., Guja, L.K., Harwood, T., Joseph, L., Lepschi, B., Nargar, K., Schmidt-Lebuhn, A., Broadhurst, L.M., 2021. Implications of the 2019–2020 megafires for the biogeography and conservation of Australian vegetation. Nature Communications 12, 1–13. https://doi.org/10.1038/s41467-021-21266-5

Gridgeman, N.T., 1970. Lamé Ovals. The Mathematical Gazette 54, 31–37. https://doi.org/10.2307/3613154

Hall, J.V., Zhang, R., Schroeder, W., Huang, C., Giglio, L., 2019. Validation of GOES-16 ABI and MSG SEVIRI active fire products. International Journal of Applied Earth Observation and Geoinformation 83, 101928. https://doi.org/10.1016/j.jag.2019.101928

Hally, B., Wallace, L., Reinke, K., Jones, S., 2023. A New Spatio-Temporal Selection Method for Estimating Upwelling Medium-Wave Radiation. Remote Sensing 15, 3521. https://doi.org/10.3390/rs15143521

Hally, B., Wallace, L., Reinke, K., Jones, S., Skidmore, A., 2019. Advances in active fire detection using a multi-temporal method for next-generation geostationary satellite data. International Journal of Digital Earth 12, 1030–1045. https://doi.org/10.1080/17538947.2018.1497099

Haslem, A., Radford, J.Q., Bennett, A.F., Watson, S.J., Chick, M.P., Huang, J., Berry, L.E., Clarke, M.F., 2024. Measuring the ecological outcomes of fire: metrics to guide fire management. fire ecol 20, 99. https://doi.org/10.1186/s42408-024-00333-4

Henry, M.C., Maingi, J.K., McCarty, J., 2019. Fire on the Water Towers: Mapping Burn Scars on Mount Kenya Using Satellite Data to Reconstruct Recent Fire History. Remote Sensing 11, 104. https://doi.org/10.3390/rs11020104

Heward, H., Smith, A.M.S., Roy, D.P., Tinkham, W.T., Hoffman, C.M., Morgan, P., Lannom, K.O., 2013. Is burn severity related to fire intensity? Observations from landscape scale remote sensing. International Journal of Wildland Fire 22, 910–918. https://doi.org/10.1071/WF12087

Hislop, S., Jones, S., Soto-Berelov, M., Skidmore, A., Haywood, A., Nguyen, T.H., 2018. Using landsat spectral indices in time-series to assess wildfire disturbance and recovery. Remote Sensing 10, 1–17. https://doi.org/10.3390/rs10030460

Holmlund, K., Grandell, J., Schmetz, J., Stuhlmann, R., Bojkov, B., Munro, R., Lekouara, M., Coppens, D., Viticchie, B., August, T., Theodore, B., Watts, P., Dobber, M., Fowler, G., Bojinski, S., Schmid, A., Salonen, K., Tjemkes, S., Aminou, D., Blythe, P., 2021. Meteosat Third Generation (MTG): Continuation and Innovation of Observations from Geostationary Orbit. Bulletin of the American Meteorological Society 102, E990–E1015. https://doi.org/10.1175/BAMS-D-19-0304.1

Huang, H., Wang, Y., Rudin, C., Browne, E.P., 2022. Towards a comprehensive evaluation of dimension reduction methods for transcriptomic data visualization. Commun Biol 5, 719. https://doi.org/10.1038/s42003-022-03628-x

Huettermann, S., Jones, S., Soto-Berelov, M., Hislop, S., 2023. Using Landsat time series and bi-temporal GEDI to compare spectral and structural vegetation responses after fire. International Journal of Applied Earth Observation and Geoinformation 122, 103403. https://doi.org/10.1016/j.jag.2023.103403

Hyer, E.J., Reid, J.S., Prins, E.M., Hoffman, J.P., Schmidt, C.C., Miettinen, J.I., Giglio, L., 2013. Patterns of fire activity over Indonesia and Malaysia from polar and geostationary satellite observations. Atmospheric Research 122, 504–519. https://doi.org/10.1016/j.atmosres.2012.06.011

Ichoku, C., Ellison, L., 2014. Global top-down smoke-aerosol emissions estimation using satellite fire radiative power measurements. Atmospheric Chemistry and Physics 14, 6643–6667. https://doi.org/10.5194/acp-14-6643-2014

Ichoku, C., Kaufman, Y.J., 2005. A method to derive smoke emission rates from MODIS fire radiative energy measurements. IEEE Transactions on Geoscience and Remote Sensing 43, 2636–2649. https://doi.org/10.1109/TGRS.2005.857328

Jain, P., Barber, Q.E., Taylor, S.W., Whitman, E., Castellanos Acuna, D., Boulanger, Y., Chavardès, R.D., Chen, J., Englefield, P., Flannigan, M., Girardin, M.P., Hanes, C.C., Little, J., Morrison, K., Skakun, R.S., Thompson, D.K., Wang, X., Parisien, M.-A., 2024. Drivers and Impacts of the Record-Breaking 2023 Wildfire Season in Canada. Nat Commun 15, 6764. https://doi.org/10.1038/s41467-024-51154-7

Ji, Y., Wang, L., Zhang, W., Marino, A., Wang, M., Ma, J., Shi, J., Jing, Q., Zhang, F., Zhao, H., Huang, G., Yang, F., Wang, G., 2024. Forest above-ground biomass estimation using X, C, L, and P band SAR polarimetric observations and different inversion models. International Journal of Digital Earth 17, 2310730. https://doi.org/10.1080/17538947.2024.2310730

Jia, G., Shevliakova, E., Artaxo, P., Noblet-Ducoudré, N.D., Houghton, R., House, J., Kitajima, K., Lennard, C., Popp, A., Sirin, A., Sukumar, R., Verchot, L., 2019. Land–climate interactions, in: Bernier, P., Espinoza, J.C., Semenov, S. (Eds.), Climate Change and Land: An IPCC Special Report on Climate Change, Desertification, Land Degradation, Sustainable Land Management, Food Security, and Greenhouse Gas Fluxes in Terrestrial Ecosystems. pp. 131–248.

Johnston, J., Johnston, L., Wooster, M., Brookes, A., McFayden, C., Cantin, A., 2018. Satellite Detection Limitations of Sub-Canopy Smouldering Wildfires in the North American Boreal Forest. Fire 1, 28. https://doi.org/10.3390/fire1020028

Jolliffe, I.T., Cadima, J., 2016. Principal component analysis: a review and recent developments. Phil. Trans. R. Soc. A. 374, 20150202. https://doi.org/10.1098/rsta.2015.0202

Jones, M.W., Abatzoglou, J.T., Veraverbeke, S., Andela, N., Lasslop, G., Forkel, M., Smith, A.J.P., Burton, C., Betts, R.A., Van Der Werf, G.R., Sitch, S., Canadell, J.G., Santín, C., Kolden, C., Doerr, S.H., Le Quéré, C., 2022. Global and Regional Trends and Drivers of Fire Under Climate Change. Reviews of Geophysics 60, e2020RG000726. https://doi.org/10.1029/2020RG000726

Jones, M.W., Veraverbeke, S., Andela, N., Doerr, S.H., Kolden, C., Mataveli, G., Pettinari, M.L., Le Quéré, C., Rosan, T.M., Van Der Werf, G.R., Van Wees, D., Abatzoglou, J.T., 2024. Global rise in forest fire emissions linked to climate change in the extratropics. Science 386, eadl5889. https://doi.org/10.1126/science.adl5889

Jucker, T., Gosper, C.R., Wiehl, G., Yeoh, P.B., Raisbeck-Brown, N., Fischer, F.J., Graham, J., Langley, H., Newchurch, W., O'Donnell, A.J., Page, G.F.M., Zdunic, K., Prober, S.M., 2023. Using multi-platform LiDAR to guide the conservation of the world's largest temperate woodland. Remote Sensing of Environment 296, 113745. https://doi.org/10.1016/j.rse.2023.113745

Kaiser, H.F., 1960. The Application of Electronic Computers to Factor Analysis. Educational and Psychological Measurement 20, 141–151. https://doi.org/10.1177/001316446002000116

Kaufman, Y.J., Justice, C., Flynn, L., Kendall, J., Giglio, L., Ward, D.E., Menzel, P., Setzer, A., 1998. Potential Global Fire Monitoring from EOS-MODIS. Journal of Geophysical Research 103, 32215–32238.

Keeley, J.E., 2009. Fire intensity, fire severity and burn severity: A brief review and suggested usage. International Journal of Wildland Fire 18, 116–126. https://doi.org/10.1071/WF07049

Key, C.H., Benson, N.C., 2006. Landscape Assessment: Ground measure of severity, the Composite Burn Index; and Remote sensing of severity, the Normalized Burn Ratio, in: FIREMON: Fire Effects Monitoring and Inventory System. USDA Forest Service, Rocky Mountain Research Station, Ogden, UT., p. LA 1-51.

Kim, D., Gu, M., Oh, T.-H., Kim, E.-K., Yang, H.-J., 2021. Introduction of the Advanced Meteorological Imager of Geo-Kompsat-2a: In-Orbit Tests and Performance Validation. Remote Sensing 13, 1303. https://doi.org/10.3390/rs13071303

Kotu, V., Deshpande, B., 2015. Classification, in: Predictive Analytics and Data Mining. Elsevier, pp. 63–163. https://doi.org/10.1016/B978-0-12-801460-8.00004-5

Krause, C., Dunn, B., Bishop-Taylor, R., Adams, C., Burton, C., Alger, M., Chua, S., Phillips, C., Newey, V., Kouzoubov, K., Leith, A., Ayers, D., Hicks, A., 2021. DEA Notebooks contributors 2021. Digital Earth Australia notebooks and tools repository. https://doi.org/10.26186/145234

Kuhn, H.W., 1955. The Hungarian method for the assignment problem. Naval Research Logistics 2, 83–97. https://doi.org/10.1002/nav.3800020109

Landry, J.S., Matthews, H.D., 2016. Non-deforestation fire vs. fossil fuel combustion: The source of CO2 emissions affects the global carbon cycle and climate responses. Biogeosciences 13, 2137–2149. https://doi.org/10.5194/bg-13-2137-2016

Lang, Y., Moeini-Meybodi, H., 2021. Wildfires – a growing concern for sustainable development (Policy Brief No. 111). United Nations - Department of Economic and Social Afairs, Forum on Forests Secretariat in UN DESA.

Lee, K., Van Leeuwen, W.J.D., Gillan, J.K., Falk, D.A., 2024. Examining the Impacts of Pre-Fire Forest Conditions on Burn Severity Using Multiple Remote Sensing Platforms. Remote Sensing 16, 1803. https://doi.org/10.3390/rs16101803

Lekouara, M., Grandell, J., Burini, A., Viticchie, B., Mueller, J., Avbelj, J., Straif, C., Mousivand, A., Stock, S., Wagner, S., Hadesty, S., Enno, S.-E., Strandgren, J., Meraner, A., Innorta, D., Fowler, G., 2024. Outcomes of the MTG-I1 FCI and LI Cal/Val, and status of MTG-S, in: Https://Doi.Org/10.1117/12.3028533. Presented at the Proc. SPIE 13143, Earth Observing Systems XXIX. https://doi.org/10.1117/12.3028533

Levin, N., Yebra, M., Phinn, S., 2021. Unveiling the Factors Responsible for Australia's Black Summer Fires of 2019/2020. Fire 4, 58. https://doi.org/10.3390/fire4030058

Li, F., Jupp, D.L.B., Reddy, S., Lymburner, L., Mueller, N., Tan, P., Islam, A., 2010. An Evaluation of the Use of Atmospheric and BRDF Correction to Standardize Landsat Data. IEEE J. Sel. Top. Appl. Earth Observations Remote Sensing 3, 257–270. https://doi.org/10.1109/JSTARS.2010.2042281

Li, F., Zhang, X., Kondragunta, S., 2021. Highly anomalous fire emissions from the 2019–2020 australian bushfires. Environmental Research Communications 3. https://doi.org/10.1088/2515-7620/ac2e6f

Li, F., Zhang, X., Kondragunta, S., 2020a. Biomass burning in Africa: An investigation of fire radiative power missed by MODIS using the 375 m VIIRS active fire product. Remote Sensing 12. https://doi.org/10.3390/rs12101561

Li, F., Zhang, X., Kondragunta, S., Csiszar, I., 2018a. Comparison of Fire Radiative Power Estimates From VIIRS and MODIS Observations. Journal of Geophysical Research: Atmospheres 123, 4545–4563. https://doi.org/10.1029/2017JD027823

Li, F., Zhang, X., Kondragunta, S., Lu, X., Csiszar, I., Schmidt, C.C., 2022. Hourly biomass burning emissions product from blended geostationary and polar-orbiting satellites for air quality forecasting applications. Remote Sensing of Environment 281, 113237. https://doi.org/10.1016/j.rse.2022.113237

Li, F., Zhang, X., Kondragunta, S., Roy, D.P., 2018b. Investigation of the Fire Radiative Energy Biomass Combustion Coefficient: A Comparison of Polar and Geostationary Satellite Retrievals Over the Conterminous United States. Journal of Geophysical Research: Biogeosciences 123, 722–739. https://doi.org/10.1002/2017JG004279

Li, F., Zhang, X., Kondragunta, S., Schmidt, C.C., Holmes, C.D., 2020b. A preliminary evaluation of GOES-16 active fire product using Landsat-8 and VIIRS active fire data, and ground-based prescribed fire records. Remote Sensing of Environment 237, 111600. https://doi.org/10.1016/j.rse.2019.111600

Li, F., Zhang, X., Roy, D.P., Kondragunta, S., 2019a. Estimation of biomass-burning emissions by fusing the fire radiative power retrievals from polar-orbiting and geostationary satellites across the conterminous United States. Atmospheric Environment 211, 274–287. https://doi.org/10.1016/j.atmosenv.2019.05.017

Li, F., Zhang, X., Roy, D.P., Kondragunta, S., 2019b. Estimation of biomass-burning emissions by fusing the fire radiative power retrievals from polar-orbiting and geostationary satellites across the conterminous United States. Atmospheric Environment 211, 274–287. https://doi.org/10.1016/j.atmosenv.2019.05.017

Lin, S., Li, L., Liu, S., Gao, G., Zhao, X., Chen, L., Qi, J., Shen, Q., Huang, H., 2024. Stratified burn severity assessment by integrating spaceborne spectral and waveform attributes in Great Xing'an Mountain. Remote Sensing of Environment 307, 114152. https://doi.org/10.1016/j.rse.2024.114152

Lindsey, D.T., Heidinger, A.K., Sullivan, P.C., McCorkel, J., Schmit, T.J., Tomlinson, M., Vandermeulen, R., Frost, G.J., Kondragunta, S., Rudlosky, S., 2024. GeoXO: NOAA's Future Geostationary Satellite System. Bulletin of the American Meteorological Society 105, E660–E679. https://doi.org/10.1175/BAMS-D-23-0048.1

Liu, Z., Ballantyne, A.P., Cooper, L.A., 2019. Biophysical feedback of global forest fires on surface temperature. Nat Commun 10, 214. https://doi.org/10.1038/s41467-018-08237-z

Lizundia-Loiola, J., Franquesa, M., Khairoun, A., Chuvieco, E., 2022. Global burned area mapping from Sentinel-3 Synergy and VIIRS active fires. Remote Sensing of Environment 282, 113298. https://doi.org/10.1016/j.rse.2022.113298

Lizundia-Loiola, J., Otón, G., Ramo, R., Chuvieco, E., 2020. A spatio-temporal active-fire clustering approach for global burned area mapping at 250 m from MODIS data. Remote Sensing of Environment 236, 111493. https://doi.org/10.1016/j.rse.2019.111493

López-García, M.J., Caselles, V., 1991. Mapping burns and natural reforestation using thematic Mapper data. Geocarto International 6, 31–37. https://doi.org/10.1080/10106049109354290

Lu, S., Jones, E., Zhao, L., Sun, Y., Qin, K., Liu, J., Li, J., Abeysekara, P., Mueller, N., Oliver, S., O'Hehir, J., Peters, S., 2024. Onboard AI for Fire Smoke Detection Using Hyperspectral Imagery: An Emulation for the Upcoming Kanyini Hyperscout-2 Mission. IEEE J. Sel. Top. Appl. Earth Observations Remote Sensing 17, 9629–9640. https://doi.org/10.1109/JSTARS.2024.3394574

Lymburner, L., Tan, P., McIntyre, A., Thankappan, M., Sixsmith, J., 2015. Dynamic Land Cover Dataset Version 2.1.

Maier, S.W., Russell-Smith, J., 2012. Measuring and monitoring of contemporary fire regimes in Australia using satellite remote sensing, in: Flammable Australia : Fire Regimes, Biodiversity and Ecosystems in a Changing World. CSIRO Publishing, p. 399.

Mallick, K., Chakraborty, S., Mallik, S., Bandyopadhyay, S., 2023. A scalable unsupervised learning of scRNAseq data detects rare cells through integration of structure-preserving embedding, clustering and outlier detection. Briefings in Bioinformatics 24, bbad125. https://doi.org/10.1093/bib/bbad125

Marcos, B., Gonçalves, J., Alcaraz-Segura, D., Cunha, M., Honrado, J.P., 2021. A Framework for Multi-Dimensional Assessment of Wildfire Disturbance Severity from Remotely Sensed Ecosystem Functioning Attributes. Remote Sensing 13, 780. https://doi.org/10.3390/rs13040780

Mariani, M., Holz, A., Veblen, T.T., Williamson, G., Fletcher, M., Bowman, D.M.J.S., 2018. Climate Change Amplifications of Climate-Fire Teleconnections in the Southern Hemisphere. Geophysical Research Letters 45, 5071–5081. https://doi.org/10.1029/2018GL078294

Martínez, B., Camacho, F., Verger, A., García-Haro, F.J., Gilabert, M.A., 2013. Intercomparison and quality assessment of MERIS, MODIS and SEVIRI FAPAR products over the Iberian Peninsula. International Journal of Applied Earth Observation and Geoinformation 21, 463–476. https://doi.org/10.1016/j.jag.2012.06.010

McCarley, T.R., Hudak, A.T., Sparks, A.M., Vaillant, N.M., Meddens, A.J.H., Trader, L., Mauro, F., Kreitler, J., Boschetti, L., 2020. Estimating wildfire fuel consumption with multitemporal airborne laser scanning data and demonstrating linkage with MODIS-derived fire radiative energy. Remote Sensing of Environment 251, 112114. https://doi.org/10.1016/j.rse.2020.112114

McCarthy, G., Moon, K., Smith, L., 2017. Mapping fire severity and fire extent in forest in Victoria for ecological and fuel outcomes. Eco Management Restoration 18, 54–65. https://doi.org/10.1111/emr.12242
McInnes, L., Healy, J., Melville, J., 2020. UMAP: Uniform Manifold Approximation and Projection for Dimension Reduction.
McInnes, L., Healy, J., Saul, N., Großberger, L., 2018. UMAP: Uniform Manifold Approximation and Projection. JOSS 3, 861. https://doi.org/10.21105/joss.00861
Meng, R., Wu, J., Schwager, K.L., Zhao, F., Dennison, P.E., Cook, B.D., Brewster, K., Green, T.M., Serbin, S.P., 2017. Using high spatial resolution satellite imagery to map forest burn severity across spatial scales in a Pine Barrens ecosystem. Remote Sensing of Environment 191, 95–109. https://doi.org/10.1016/j.rse.2017.01.016
Messerli, P., Murniningtyas, E., Eloundou-Enyegue, P., Foli, E.G., Furman, E., Glassman, A., Hernández Licona, G., Kim, E.M., Lutz, W., Moatti, J.-P., Richardson, K., Saidam, M., Smith, D., Kazimieras Staniškis, J., van Ypersele, J.-P., 2019. The Future is Now – Science for Achieving Sustainable Development, UNDESA. UN, New York.
Miller, C.W., Harvey, B.J., Kane, V.R., Moskal, L.M., Alvarado, E., 2023. Different approaches make comparing studies of burn severity challenging: a review of methods used to link remotely sensed data with the Composite Burn Index. International Journal of Wildland Fire 450–476. https://doi.org/10.1071/wf22050
Miller, J.D., Thode, A.E., 2007. Quantifying burn severity in a heterogeneous landscape with a relative version of the delta Normalized Burn Ratio (dNBR). Remote Sensing of Environment 109, 66–80. https://doi.org/10.1016/j.rse.2006.12.006
Morgan, P., Keane, R.E., Dillon, G.K., Jain, T.B., Hudak, A.T., Karau, E.C., Sikkink, P.G., Holden, Z.A., Strand, E.K., 2014. Challenges of assessing fire and burn severity using field measures, remote sensing and modelling. International Journal of Wildland Fire 23, 1045–1060. https://doi.org/10.1071/WF13058
Mota, B., Wooster, M.J., 2018. A new top-down approach for directly estimating biomass burning emissions and fuel consumption rates and totals from geostationary satellite fire radiative power (FRP). Remote Sensing of Environment 206, 45–62. https://doi.org/10.1016/j.rse.2017.12.016
Nguyen, H.M., He, J., Wooster, M.J., 2023. Biomass burning CO, PM and fuel consumption per unit burned area estimates derived across Africa using geostationary SEVIRI fire radiative power and Sentinel-5P CO data. Atmos. Chem. Phys. 23, 2089–2118. https://doi.org/10.5194/acp-23-2089-2023
Nguyen, H.M., Wooster, M.J., 2020. Advances in the estimation of high Spatio-temporal resolution pan-African top-down biomass burning emissions made using geostationary fire radiative power (FRP) and MAIAC aerosol optical depth (AOD) data. Remote Sensing of Environment 248, 111971. https://doi.org/10.1016/j.rse.2020.111971
NISAR, 2018. NASA-ISRO SAR (NISAR) Mission Science Users' Handbook. NASA Jet Propulsion Laboratory.
NSW DCCEEW, 2020. State Government of NSW and NSW Department of Climate Change, Energy, the Environment and Water 2020, Fire Extent and Severity Mapping (FESM).
Oliveira, S.L.J., Maier, S.W., Pereira, J.M.C., Russell-Smith, J., 2015. Seasonal differences in fire activity and intensity in tropical savannas of northern Australia using satellite measurements of fire radiative power. International Journal of Wildland Fire 24, 249–260. https://doi.org/10.1071/WF13201
Parker, B.M., Lewis, T., Srivastava, S.K., 2015. Estimation and evaluation of multi-decadal fire severity patterns using Landsat sensors. Remote Sensing of Environment 170, 340–349. https://doi.org/10.1016/j.rse.2015.09.014
Parks, S., Dillon, G., Miller, C., 2014. A New Metric for Quantifying Burn Severity: The Relativized Burn Ratio. Remote Sensing 6, 1827–1844. https://doi.org/10.3390/rs6031827

Pedregosa, F., Varoquaux, G., Gramfort, A., Michel, V., Thirion, B., Grisel, O., Blondel, M., Prettenhofer, P., Weiss, R., Dubourg, V., Vanderplas, J., Passos, A., Cournapeau, D., 2011. Scikit-learn: Machine Learning in Python. MACHINE LEARNING IN PYTHON.

Pettinari, M.L., Chuvieco, E., 2020. Fire Danger Observed from Space. Surveys in Geophysics 23. https://doi.org/10.1007/s10712-020-09610-8

Ponomarev, E.I., Zabrodin, A.N., Shvetsov, E.G., Ponomareva, T.V., 2023. Wildfire Intensity and Fire Emissions in Siberia. Fire 6, 246. https://doi.org/10.3390/fire6070246

Qi, W., Saarela, S., Armston, J., Ståhl, G., Dubayah, R., 2019. Forest biomass estimation over three distinct forest types using TanDEM-X InSAR data and simulated GEDI lidar data. Remote Sensing of Environment 232, 111283. https://doi.org/10.1016/j.rse.2019.111283

Quegan, S., Le Toan, T., Chave, J., Dall, J., Exbrayat, J.F., Minh, D.H.T., Lomas, M., D'Alessandro, M.M., Paillou, P., Papathanassiou, K., Rocca, F., Saatchi, S., Scipal, K., Shugart, H., Smallman, T.L., Soja, M.J., Tebaldini, S., Ulander, L., Villard, L., Williams, M., 2019. The European Space Agency BIOMASS mission: Measuring forest above-ground biomass from space. Remote Sensing of Environment 227, 44–60. https://doi.org/10.1016/j.rse.2019.03.032

Ramsey, S., Reinke, K., Trihantoro, N., Jones, S., Engel, C., 2021. Kangaroo island Black Summer 2019-2020 fire reconstruction. Bushfire and Natural Hazards CRC, Melbourne.

Rao, K., Williams, A.P., Flefil, J.F., Konings, A.G., 2020. SAR-enhanced mapping of live fuel moisture content. Remote Sensing of Environment 245, 111797. https://doi.org/10.1016/j.rse.2020.111797

Richardson, D., Black, A.S., Irving, D., Matear, R.J., Monselesan, D.P., Risbey, J.S., Squire, D.T., Tozer, C.R., 2022. Global increase in wildfire potential from compound fire weather and drought. npj Clim Atmos Sci 5, 23. https://doi.org/10.1038/s41612-022-00248-4

Roberts, G., Wooster, M.J., 2014. Development of a multi-temporal Kalman filter approach to geostationary active fire detection & fire radiative power (FRP) estimation. Remote Sensing of Environment 152, 392–412. https://doi.org/10.1016/j.rse.2014.06.020

Roberts, G., Wooster, M.J., Lauret, N., Gastellu-Etchegorry, J.-P., Lynham, T., McRae, D., 2018. Investigating the impact of overlying vegetation canopy structures on fire radiative power (FRP) retrieval through simulation and measurement. Remote Sensing of Environment 217, 158–171. https://doi.org/10.1016/j.rse.2018.08.015

Roberts, G., Wooster, M.J., Perry, G.L.W., Drake, N., Rebelo, L.M., Dipotso, F., 2005. Retrieval of biomass combustion rates and totals from fire radiative power observations: Application to southern Africa using geostationary SEVIRI imagery. Journal of Geophysical Research Atmospheres 110, 1–19. https://doi.org/10.1029/2005JD006018

Roberts, G., Wooster, M.J., Xu, W., Freeborn, P.H., Morcrette, J.J., Jones, L., Benedetti, A., Jiangping, H., Fisher, D., Kaiser, J.W., 2015. LSA SAF Meteosat FRP products-Part 2: Evaluation and demonstration for use in the Copernicus Atmosphere Monitoring Service (CAMS). Atmospheric Chemistry and Physics 15, 13241–13267. https://doi.org/10.5194/acp-15-13241-2015

Roberts, G.J., Wooster, M.J., 2008. Fire detection and fire characterization over Africa using meteosat SEVIRI. IEEE Transactions on Geoscience and Remote Sensing 46, 1200–1218. https://doi.org/10.1109/TGRS.2008.915751

Roy, D.P., 1999. Multi-temporal active-fire based burn scar detection algorithm. International Journal of Remote Sensing 20, 1031–1038. https://doi.org/10.1080/014311699213073

Roy, D.P., Boschetti, L., Maier, S.W., Smith, A.M.S., 2010. Field estimation of ash and char colour-lightness using a standard grey scale. Int. J. Wildland Fire 19, 698. https://doi.org/10.1071/WF09133

Roy, D.P., Boschetti, L., Trigg, S.N., 2006. Remote Sensing of Fire Severity: Assessing the Performance of the Normalized Burn Ratio. IEEE Geosci. Remote Sensing Lett. 3, 112–116. https://doi.org/10.1109/LGRS.2005.858485

Roy, D.P., De Lemos, H., Huang, H., Giglio, L., Houborg, R., Miura, T., 2024. Multi-resolution monitoring of the 2023 maui wildfires, implications and needs for satellite-based wildfire disaster monitoring. Science of Remote Sensing 10, 100142. https://doi.org/10.1016/j.srs.2024.100142

Roy, D.P., Huang, H., Boschetti, L., Giglio, L., Yan, L., Zhang, H.H., Li, Z., 2019. Landsat-8 and Sentinel-2 burned area mapping - A combined sensor multi-temporal change detection approach. Remote Sensing of Environment 231, 111254. https://doi.org/10.1016/j.rse.2019.111254

Roy, D.P., Landmann, T., 2005. Characterizing the surface heterogeneity of fire effects using multi-temporal reflective wavelength data. International Journal of Remote Sensing 26, 4197–4218. https://doi.org/10.1080/01431160500112783

Roy, D.P., Li, Z., Giglio, L., Boschetti, L., Huang, H., 2021. Spectral and diurnal temporal suitability of GOES Advanced Baseline Imager (ABI) reflectance for burned area mapping. International Journal of Applied Earth Observation and Geoinformation 96. https://doi.org/10.1016/j.jag.2020.102271

Rumpff, L., Legge, S., Van Leeuwen, S., Wintle, B., Woinarski, J. (Eds.), 2023. Australia's Megafires: Biodiversity Impacts and Lessons from 2019-2020. CSIRO Publishing. https://doi.org/10.1071/9781486316656

Saberi, S.J., Harvey, B.J., 2023. What is the color when black is burned? Quantifying (re)burn severity using field and satellite remote sensing indices. fire ecol 19, 24. https://doi.org/10.1186/s42408-023-00178-3

Santoro, M., Cartus, O., Wegmüller, U., Besnard, S., Carvalhais, N., Araza, A., Herold, M., Liang, J., Cavlovic, J., Engdahl, M.E., 2022. Global estimation of above-ground biomass from spaceborne C-band scatterometer observations aided by LiDAR metrics of vegetation structure. Remote Sensing of Environment 279, 113114. https://doi.org/10.1016/j.rse.2022.113114

Schmidt, C.C., Hoffman, J., Prins, E., Lindstrom, S., 2020. GOES-R Advanced Baseline Imager (ABI) Algorithm Theoretical Basis Document For Fire / Hot Spot Characterization (No. 2.7). NOAA NESDIS STAR.

Schmit, T.J., Gunshor, M.M., Menzel, W.P., Gurka, J.J., Li, J., Bachmeier, A.S., 2005. INTRODUCING THE NEXT-GENERATION ADVANCED BASELINE IMAGER ON GOES-R. Bull. Amer. Meteor. Soc. 86, 1079–1096. https://doi.org/10.1175/BAMS-86-8-1079

Schöttl, F., Spichtinger, A., Franquinet, J., Langer, M., 2024. Real-Time On-Orbit Fire Detection on FOREST-2, in: IGARSS 2024 - 2024 IEEE International Geoscience and Remote Sensing Symposium. Presented at the IGARSS 2024 - 2024 IEEE International Geoscience and Remote Sensing Symposium, IEEE, Athens, Greece, pp. 2360–2364. https://doi.org/10.1109/IGARSS53475.2024.10641618

Schroeder, W., Giglio, L., 2018. NASA VIIRS Land Science Investigator Processing System (SIPS) Visible Infrared Imaging Radiometer Suite (VIIRS) 375 m & 750 m Active Fire Products: Product User's Guide Version 1.4, Nasa.

Schroeder, W., Oliva, P., Giglio, L., Csiszar, I.A., 2014. The New VIIRS 375m active fire detection data product: Algorithm description and initial assessment. Remote Sensing of Environment 143, 85–96. https://doi.org/10.1016/j.rse.2013.12.008

Shen, Y., Jiang, C., Chan, K.L., Hu, C., Yao, L., 2021. Estimation of Field-Level NO x Emissions from Crop Residue Burning Using Remote Sensing Data : A Case Study in Hubei, China. Remote Sensing 13, 404. https://doi.org/10.3390/rs13030404

Silva, C.A., Duncanson, L., Hancock, S., Neuenschwander, A., Thomas, N., Hofton, M., Fatoyinbo, L., Simard, M., Marshak, C.Z., Armston, J., Lutchke, S., Dubayah, R., 2021. Fusing simulated GEDI, ICESat-2 and NISAR data for regional aboveground biomass mapping. Remote Sensing of Environment 253, 112234. https://doi.org/10.1016/j.rse.2020.112234

Sloan, S., Locatelli, B., Andela, N., Cattau, M.E., Gaveau, D., Tacconi, L., 2022. Declining severe fire activity on managed lands in Equatorial Asia. Communications Earth and Environment 3. https://doi.org/10.1038/s43247-022-00522-6

Smith, A.M.S., Sparks, A.M., Kolden, C.A., Abatzoglou, J.T., Talhelm, A.F., Johnson, D.M., Boschetti, L., Lutz, J.A., Apostol, K.G., Yedinak, K.M., Tinkham, W.T., Kremens, R.J., 2016. Towards a new paradigm in fire severity research using dose-response experiments. International Journal of Wildland Fire 25, 158–166. https://doi.org/10.1071/WF15130

Smith, A.M.S., Talhelm, A.F., Johnson, D.M., Sparks, A.M., Kolden, C.A., Yedinak, K.M., Apostol, K.G., Tinkham, W.T., Abatzoglou, J.T., Lutz, J.A., Davis, A.S., Pregitzer, K.S., Adams, H.D., Kremens, R.L., 2017. Effects of fire radiative energy density dose on Pinus contorta and Larix occidentalis seedling physiology and mortality. International Journal of Wildland Fire 26, 82–94. https://doi.org/10.1071/WF16077

Smith, A.M.S., Wooster, M.J., Drake, N.A., Dipotso, F.M., Falkowski, M.J., Hudak, A.T., 2005. Testing the potential of multi-spectral remote sensing for retrospectively estimating fire severity in African Savannahs. Remote Sensing of Environment 97, 92–115. https://doi.org/10.1016/j.rse.2005.04.014

SOFR, 2018. Australia's State of the Forests Report 2018 – Executive summary. Department of Agriculture and Water Resources, Australian Government.

Sparks, A.M., Boschetti, L., Smith, A.M.S., Tinkham, W.T., Lannom, K.O., Newingham, B.A., 2015. An accuracy assessment of the MTBS burned area product for shrub-steppe fires in the northern Great Basin, United States. International Journal of Wildland Fire 24, 70–78. https://doi.org/10.1071/WF14131

Sparks, A.M., Kolden, C.A., Smith, A.M.S., Boschetti, L., Johnson, D.M., Cochrane, M.A., 2018. Fire intensity impacts on post-fire temperate coniferous forest net primary productivity. Biogeosciences 15, 1173–1183. https://doi.org/10.5194/bg-15-1173-2018

Sparks, A.M., Kolden, C.A., Talhelm, A.F., Smith, A.M.S., Apostol, K.G., Johnson, D.M., Boschetti, L., 2016. Spectral indices accurately quantify changes in seedling physiology following fire: Towards mechanistic assessments of post-fire carbon cycling. Remote Sensing 8. https://doi.org/10.3390/rs8070572

Sparks, A.M., Smith, A.M.S., Hudak, A.T., Corrao, M.V., Kremens, R.L., Keefe, R.F., 2023a. Integrating active fire behavior observations and multitemporal airborne laser scanning data to quantify fire impacts on tree growth: A pilot study in mature Pinus ponderosa stands. Forest Ecology and Management 545, 121246. https://doi.org/10.1016/j.foreco.2023.121246

Sparks, A.M., Smith, A.M.S., Hudak, A.T., Corrao, M.V., Kremens, R.L., Keefe, R.F., 2023b. Integrating active fire behavior observations and multitemporal airborne laser scanning data to quantify fire impacts on tree growth: A pilot study in mature Pinus ponderosa stands. Forest Ecology and Management 545, 121246. https://doi.org/10.1016/j.foreco.2023.121246

Sparks, A.M., Smith, A.M.S., Talhelm, A.F., Kolden, C.A., Yedinak, K.M., Johnson, D.M., 2017. Impacts of fire radiative flux on mature Pinus ponderosa growth and vulnerability to secondary mortality agents. International Journal of Wildland Fire 26, 95–106. https://doi.org/10.1071/WF16139

Subasinghe Achchige, Y.M., Volkova, L., Filkov, A.I., Weston, C.J., 2022. Effect of bark properties on the cambium cell viability of Eucalyptus species under low radiative heat exposure. Forest Ecology and Management 521, 120443. https://doi.org/10.1016/j.foreco.2022.120443

Szpakowski, D.M., Jensen, J.L.R., 2019. A review of the applications of remote sensing in fire ecology. Remote Sensing 11. https://doi.org/10.3390/rs11222638

Thapa, L.H., Saide, P.E., Bortnik, J., Berman, M.T., Da Silva, A., Peterson, D.A., Li, F., Kondragunta, S., Ahmadov, R., James, E., Romero-Alvarez, J., Ye, X., Soja, A., Wiggins, E., Gargulinski, E., 2024. Forecasting Daily Fire Radiative Energy Using Data Driven Methods and Machine Learning Techniques. JGR Atmospheres 129, e2023JD040514. https://doi.org/10.1029/2023JD040514

Tortorelli, C.M., Latimer, A.M., Young, D.J.N., 2024. Moderating effects of past wildfire on reburn severity depend on climate and initial severity in Western U S forests. Ecological Applications 34, e3023. https://doi.org/10.1002/eap.3023

UN General Assembly, 2015. Transforming our world: The 2030 agenda for sustainable development.

Valenzuela, A., Reinke, K., Jones, S., 2024. Assessing the spatial resolution distance of satellite images: SuperDove versus Landsat 8. International Journal of Remote Sensing 45, 4120–4159. https://doi.org/10.1080/01431161.2024.2357839

van der Maaten, L., Hinton, G., 2008. Visualizing Data using t-SNE. JMLR 9, 2579–2605.

Van Der Maaten, L., Hinton, G., 2012. Visualizing non-metric similarities in multiple maps. Mach Learn 87, 33–55. https://doi.org/10.1007/s10994-011-5273-4

VIC DEECA, 2020. Fire severity map of the major fires in Gippsland and north east Victoria in 2019/20 (version 1.0).
Viedma, O., Almeida, D.R.A., Moreno, J.M., 2020a. Postfire tree structure from high-resolution LiDAR and RBR sentinel 2A fire severity metrics in a pinus halepensis-dominated burned stand. Remote Sensing 12, 1–21. https://doi.org/10.3390/rs12213554
Viedma, O., Chico, F., Fernández, J.J., Madrigal, C., Safford, H.D., Moreno, J.M., 2020b. Disentangling the role of prefire vegetation vs. burning conditions on fire severity in a large forest fire in SE Spain. Remote Sensing of Environment 247. https://doi.org/10.1016/j.rse.2020.111891
Volkova, L., Paul, K.I., Roxburgh, S.H., Weston, C.J., 2022. Tree mortality and carbon emission as a function of wildfire severity in south-eastern Australian temperate forests. Science of the Total Environment 853, 158705. https://doi.org/10.1016/j.scitotenv.2022.158705
Wang, G., Cai, W., 2020. Two-year consecutive concurrences of positive Indian Ocean Dipole and Central Pacific El Niño preconditioned the 2019/2020 Australian “black summer” bushfires. Geosci. Lett. 7, 19. https://doi.org/10.1186/s40562-020-00168-2
Wang, Y., Huang, H., Rudin, C., Shaposhnik, Y., 2021. Understanding How Dimension Reduction Tools Work: An Empirical Approach to Deciphering t-SNE, UMAP, TriMap, and PaCMAP for Data Visualization. Journal of Machine Learning Research 22, 1–73.
Ward, J.H., 1963. Hierarchical Grouping to Optimize an Objective Function. Journal of the American Statistical Association 58, 236–244.
Wickramasinghe, C., Wallace, L., Reinke, K., Jones, S., 2020. Intercomparison of Himawari-8 AHI-FSA with MODIS and VIIRS active fire products. International Journal of Digital Earth 13, 457–473. https://doi.org/10.1080/17538947.2018.1527402
Wickramasinghe, C.H., Jones, S., Reinke, K., Wallace, L., 2016. Development of a multi-spatial resolution approach to the surveillance of active fire lines using Himawari-8. Remote Sensing 8, 1–13. https://doi.org/10.3390/rs8110932
Williamson, G.J., Ellis, T.M., Bowman, D.M.J.S., 2022. Double-Differenced dNBR: Combining MODIS and Landsat Imagery to Map Fine-Grained Fire MOSAICS in Lowland Eucalyptus Savanna in Kakadu National Park, Northern Australia. Fire 5, 160. https://doi.org/10.3390/fire5050160
Wintle, B.A., Legge, S., Woinarski, J.C.Z., 2020. After the Megafires: What Next for Australian Wildlife? Trends in Ecology and Evolution 35, 753–757. https://doi.org/10.1016/j.tree.2020.06.009
Wooster, M.J., 2002. Small-scale experimental testing of fire radiative energy for quantifying mass combusted in natural vegetation fires. Geophysical Research Letters 29, 21–24. https://doi.org/10.1029/2002GL015487
Wooster, M.J., Roberts, G., Freeborn, P.H., Xu, W., Govaerts, Y., Beeby, R., He, J., Lattanzio, A., Fisher, D., Mullen, R., 2015. LSA SAF Meteosat FRP products-Part 1: Algorithms, product contents, and analysis. Atmospheric Chemistry and Physics 15, 13217–13239. https://doi.org/10.5194/acp-15-13217-2015
Wooster, M.J., Roberts, G., Perry, G.L.W., Kaufman, Y.J., 2005. Retrieval of biomass combustion rates and totals from fire radiative power observations: FRP derivation and calibration relationships between biomass consumption and fire radiative energy release. Journal of Geophysical Research Atmospheres 110, 1–24. https://doi.org/10.1029/2005JD006318
Wooster, M.J., Roberts, G.J., Giglio, L., Roy, D., Freeborn, P., Boschetti, L., Justice, C., Ichoku, C., Schroeder, W., Davies, D., Smith, A., Setzer, A., Csiszar, I., Strydom, T., Frost, P., Zhang, T., Xu, W., de Jong, M., Johnston, J., Ellison, L., Vadrevu, K., McCarty, J., Tanpipat, V., Schmidt, C., San-Miguel, J., 2021. Satellite remote sensing of active fires: History and current status, applications and future requirements. Remote Sensing of Environment 267, 112694. https://doi.org/10.1016/j.rse.2021.112694
Wooster, M.J., Zhukov, B., Oertel, D., 2003. Fire radiative energy for quantitative study of biomass burning: Derivation from the BIRD experimental satellite and comparison to MODIS fire products. Remote Sensing of Environment 86, 83–107. https://doi.org/10.1016/S0034-4257(03)00070-1

Xu, W., Wooster, M.J., He, J., Zhang, T., 2021. Improvements in high-temporal resolution active fire detection and FRP retrieval over the Americas using GOES-16 ABI with the geostationary Fire Thermal Anomaly (FTA) algorithm. Science of Remote Sensing 3, 100016. https://doi.org/10.1016/j.srs.2021.100016

Xu, W., Wooster, M.J., He, J., Zhang, T., 2020. First study of Sentinel-3 SLSTR active fire detection and FRP retrieval: Night-time algorithm enhancements and global intercomparison to MODIS and VIIRS AF products. Remote Sensing of Environment 248, 111947. https://doi.org/10.1016/j.rse.2020.111947

Xu, W., Wooster, M.J., Kaneko, T., He, J., Zhang, T., Fisher, D., 2017. Major advances in geostationary fire radiative power (FRP) retrieval over Asia and Australia stemming from use of Himarawi-8 AHI. Remote Sensing of Environment 193, 138–149. https://doi.org/10.1016/j.rse.2017.02.024

Xu, W., Wooster, M.J., Roberts, G., Freeborn, P., 2010. New GOES imager algorithms for cloud and active fire detection and fire radiative power assessment across North, South and Central America. Remote Sensing of Environment 114, 1876–1895. https://doi.org/10.1016/j.rse.2010.03.012

Yang, J., Zhang, Z., Wei, C., Lu, F., Guo, Q., 2017. Introducing the New Generation of Chinese Geostationary Weather Satellites, Fengyun-4. Bulletin of the American Meteorological Society 98, 1637–1658. https://doi.org/10.1175/BAMS-D-16-0065.1

Yin, C., He, B., Yebra, M., Quan, X., Edwards, A.C., Liu, X., Liao, Z., 2020. Improving burn severity retrieval by integrating tree canopy cover into radiative transfer model simulation. Remote Sensing of Environment 236, 111454. https://doi.org/10.1016/j.rse.2019.111454

Zhang, T., De Jong, M.C., Wooster, M.J., Xu, W., Wang, L., 2020. Trends in eastern China agricultural fire emissions derived from a combination of geostationary (Himawari) and polar (VIIRS) orbiter fire radiative power products. Atmospheric Chemistry and Physics 20, 10687–10705. https://doi.org/10.5194/acp-20-10687-2020

Zhao, J., Yue, C., Wang, J., Hantson, S., Wang, X., He, B., Li, G., Wang, L., Zhao, H., Luyssaert, S., 2024. Forest fire size amplifies postfire land surface warming. Nature 633, 828–834. https://doi.org/10.1038/s41586-024-07918-8

Zheng, Y., Liu, J., Jian, H., Fan, X., Yan, F., 2021. Fire Diurnal Cycle Derived from a Combination of the Himawari-8 and VIIRS Satellites to Improve Fire Emission Assessments in Southeast Australia. Remote Sensing 13, 2852. https://doi.org/10.3390/rs13152852

Zubkova, M., Boschetti, L., Abatzoglou, J.T., Giglio, L., 2022. Fire Regions as Environmental Niches: A New Paradigm to Define Potential Fire Regimes in Africa and Australia. JGR Biogeosciences 127, e2021JG006694. https://doi.org/10.1029/2021JG006694